SOLUTION-MEDIATED STRATEGIES FOR SYNTHESIZING METAL OXIDES, BORATES AND PHOSPHIDES USING NANOCRYSTALS AS REACTIVE PRECURSORS

A Dissertation

by

AMANDA ERIN HENKES

Submitted to the Office of Graduate Studies of
Texas A&M University
in partial fulfillment of the requirements for the degree of

DOCTOR OF PHILOSOPHY

May 2008

Major Subject: Chemistry

SOLUTION-MEDIATED STRATEGIES FOR SYNTHESIZING METAL OXIDES, BORATES AND PHOSPHIDES USING NANOCRYSTALS AS REACTIVE PRECURSORS

A Dissertation

by

AMANDA ERIN HENKES

Submitted to the Office of Graduate Studies of
Texas A&M University
in partial fulfillment of the requirements for the degree of

DOCTOR OF PHILOSOPHY

Approved by:

Co-Chairs of Committee,	Raymond E. Schaak
	François P. Gabbaï
Committee Members,	Marcetta Y. Darensbourg
	Daniel F. Shantz
Head of Department,	David H. Russell

May 2008

Major Subject: Chemistry

ABSTRACT

Solution-Mediated Strategies for Synthesizing Metal Oxides, Borates and Phosphides Using Nanocrystals as Reactive Precursors. (May 2008)

Amanda Erin Henkes, B.S.; B.A., Southern Methodist University

Co-Chairs of Advisory Committee: Dr. Raymond E. Schaak
Dr. François P. Gabbaï

Because of their high surface area (and hence, increased reactivity) nanocrystals can be used as reactive precursors in the low-temperature synthesis of solid state materials. When nanocrystals are used as reactants, the temperatures needed for diffusion between them can be significantly lower than for bulk-scale reactions—often at temperatures attainable using solution-based techniques. In the following work, two synthetic strategies are defined and developed for accessing metal oxides, borates and phosphides using nanocrystalline precursors and solution-mediated techniques. Broadly, the strategies involve either 1) the formation of a nano-sized precursor in solution which is post-annealed after isolation to form a target metal oxide or borate or 2) the solution-mediated diffusion of phosphorus into a nanocrystalline metal to form target metal phosphides.

To form multi-metal oxides using the first strategy, metal oxide nanoparticle precursors are mixed in stoichiometric ratios in solution to form a nanocomposite. After isolation, the nanocomposite is annealed in air at 700-800 °C to form target ternary metal oxides, including $Y_2Ti_2O_7$, $Eu_2Ti_2O_7$, $NiTiO_3$, Zn_2SnO_4 and $CuInO_2$. As a variation of

this method, rare earth borate nanoparticle precursors can be formed in solution by the reaction of RE^{3+} with $NaBH_4$. After isolation, annealing in air at 700-800 °C crystallizes a range of $REBO_3$ and $Al_3RE(BO_3)_4$ powders.

Using solution-based techniques, metal phosphides can be formed by the reaction of pre-formed metal nanocrystals with trioctylphosphine (TOP), which acts as a mild phosphorus-source, at 300-370 °C. A range of transition metal phosphide nanocrystals are accessible using this strategy, including the polyphosphides PdP_2, AgP_2 and Au_2P_3. Furthermore, shape and size of the metal phosphide product can be influenced by the shape and size of the metal precursor, allowing for the templated-design of nanostructured metal phosphides. The utility of this technique is not limited to the nano-regime. Bulk-scale metal powders, wires, foils, thin films and nanostructured metals can be converted to metal phosphides using analogous reactions with hot TOP.

The two-fold purpose of this work is to extend these solution-mediated nanocrystal-based synthetic strategies to new classes of materials, and to compliment the existing library of low-temperature methods for making solid state materials.

ACKNOWLEDGEMENTS

I would like to thank my committee co-chair and graduate advisor Prof. Raymond E. Schaak, my committee co-chair Prof. François P. Gabbaï, and my committee members Prof. Marcetta Y. Darensbourg and Prof. Daniel F. Shantz, for their guidance and support throughout the coursework and research. Thanks also to my friends and colleagues and the department faculty and staff for making my time at Texas A&M University a great experience.

I also want to extend my gratitude to the National Science Foundation for the opportunity to conduct my research as a National Science Foundation Graduate Research Fellow. In addition, I thank the scientists who work at the Department of Chemistry's X-ray Crystallography Laboratory, the Texas A&M Microscopy and Imaging Center, and the Texas A&M Materials Characterization Facility for their guidance and assistance in collecting and analyzing my data.

Finally, I thank my parents, family, and especially my fiancé for their patience and support throughout my graduate school experiences.

NOMENCLATURE

TOP	tri-*n*-octylphosphine
PVP	poly(vinylpyrrolidone)
XRD	X-ray diffraction
TEM	transmission electron microscopy
EDS	energy dispersive spectroscopy
SAED	selected area electron diffraction
DSC	differential scanning calorimetry
TGA	thermal gravimetric analysis
SEM	scanning electron microscopy
T_c	critical temperature
RE	rare earth
TOPO	tri-*n*-octylphosphine oxide
TPP	triphenylphosphine
TOAB	tetra-*n*-octylammonium bromide
HDA	hexadecylamine
CCD	charge-coupled device
Oct_2O	octyl ether
fcc	face centered cubic
EG	ethylene glycol

TABLE OF CONTENTS

CHAPTER Page

CHAPTER Page

LIST OF FIGURES

Page

Page

Page

Page

Page

Page

Page

LIST OF TABLES

CHAPTER I

INTRODUCTION: NANOCRYSTALS AS BUILDING-BLOCKS FOR COMPLEX MATERIALS

While solid state techniques for making functional materials have been used successfully for centuries, it is important to explore and develop low temperature routes for making them due to the synthetic drawbacks of traditional high temperature techniques. Because high temperatures are necessary for breaking bonds in the extended structures of the reactants and for inducing diffusion between them,[1] the critical limitation of traditional solid state methods is that the extent of reaction is limited by the slow rate of diffusion between the solid reactants. Although rigorous re-grinding and re-heating treatments are used to improve the reaction rate between solids, the necessity of high temperatures limits the reaction products to the most thermodynamically stable phases.[1] Thus, accessing new and metastable phases and understanding reaction kinetics is virtually impossible using traditional methods.[1]

A simple solution to the problem of slow diffusion between solids is to decrease the size of the reactants so as to increase the number of surface contacts. For example, finely divided powders are commonly used in ceramic synthesis. The advantage is that the small (often nano-sized) powders have higher surface area than their bulk counterparts, which can provide more interfaces between reactants at which diffusion can occur and over shorter distances. Thus with nano-sized reactants, solid state

---

This dissertation follows the style of the *Journal of the American Chemical Society*.

reactions can occur more quickly and often at lower temperatures than when bulk-scale reactants are used.

In analogy to work done with ceramics, nanoscale reactants have been used for the synthesis of nanocrystalline and nanostructured materials because they can afford insight to reaction pathways and control over phase formation due to their enhanced reactivity at lower temperatures. For example, Buhro and co-workers synthesized NiAl and Ni_3Al intermetallics by mixing nanoscale Al and Ni in solution, followed by rigorous drying, pressing, and heat treatment at 400 °C under vacuum (lower than the typical 640 °C reaction temperature needed for the Ni-Al system).[2] Similarly, nanoscale ZnSb and Zn_4Sb_3—intermetallics with thermoelectric properties—can be synthesized below 300 °C from finely divided Zn and Sb powders.[3] This is significant because both are metastable phases and Zn_4Sb_3 is reported to decompose near 490 °C.[3] Extensive research has been done by our group investigating various low-temperature solution-based routes that use nanoparticles as reactants for forming complex materials.[4-10] Most notable is the work done with intermetallics, although many of the concepts can be adapted to other classes of materials.

There are two general solution-based approaches used in our group by which nanocrystalline reagents can be transformed into more complex materials. The first approach is called the "nanocomposite" route (Figure 1) and is distinguished by the formation of nano-mixed aggregates of two or more types of nanoparticles in solution, followed by their isolation and post-annealing as a dry powder to transform them into a target material. The second approach involves the transformation of nanocrystals to

target materials in solution upon addition of a metal reagent and annealing in solution, which will be called the "solution transformation" route (Figure 2). Several variations of the "solution transformation" route can be employed depending on the type of metal precursors used.

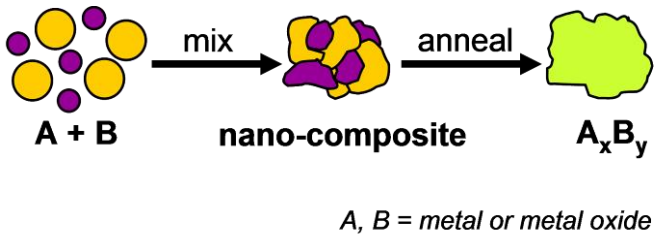

Figure 1. Reaction scheme for the "nanocomposite" route by which a binary mixture of nanoparticles forms a composite that is annealed to form a target material.

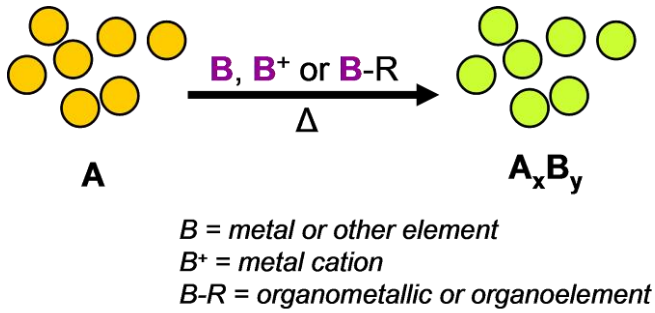

Figure 2. Reaction scheme for the "solution transformation" strategy by which nanocrystals are converted to a target material via reaction in solution with metal or element precursors (i.e., zero-valent metals, elements, ions, organometallic or organoelement reagents).

The nanocomposite route applied to alloys and intermetallics was pioneered with work done by Sra and Schaak using Au and Cu nanoparticles as precursors to form AuCu and $AuCu_3$.[4] In analogy to the work done by Buhro and Schlecht, pre-formed Au

and Cu nanoparticles were mixed in solution to form aggregates, isolated, and then annealed at 200-300 °C in a furnace under flowing argon to form target alloys and intermetallics. A key observation was that because of the shortened diffusion distances and the increased number of interfaces between the Au and Cu reactants in the aggregates, AuCu and $AuCu_3$ could form after a few hours of heating at 200-300 °C.[4] In contrast, temperatures greater than 850 °C are required to melt bulk-scale reactants in order induce diffusion, followed by annealing at 200-300 °C for several days or weeks to form the intermetallics.[4] To prove the generality and versatility of the nanocomposite route, it was extended to other alloy and intermetallic systems to form Ag_3Pt, Au_3Cu, Au_3Pd, $AuPd_2$, $AuPd_4$, CoPt, Cu_3Pt, CuPt, FePt, $FePt_3$, NiPt and Ag_2Pd_3S using nanoparticle reactants.[5] Notably, superconducting properties seen in bulk Ag_2Pd_3S were also observed using this synthetic approach.[5] Furthermore, the nanocomposite approach is a portable strategy because it utilizes simple bench-top, solution-based techniques.

Solution transformation involves the addition of one of three types of elemental precursors to a solution of metal nanocrystals: ionic reactants under reducing conditions, zero-valent elemental reactants, or organometallic/organoelement reactants. Our group has studied the transformation of metal nanocrystals to intermetallics from the addition of metal cations under reducing conditions extensively. Typically, a polyol or modified polyol process[11] is used to form metal nanocrystals in solution. Metal cations added to the solution are reduced by the polyol solvent to their zero-valent state when heated, and diffuse into the parent nanocrystals to form a target material. For example, Bauer and Schaak used this method to form a library of binary intermetallics using the polyol

process to convert Pt nanocrystals to PtSn, PtPb, PtBi and $FePt_3$ by reaction in tetraethylene glycol with metal salts at 190-308 °C ($FePt_3$ required pos-annealing at 550 °C).[6] Additionally, PtSn, PtPb, PtSb, Pt_3Sn and Cu_3Pt can be formed from Pt nanocrystals supported on Al_2O_3, CeO_2 on carbon in the same temperature range (Cu_3Pt required post-annealing at 500 °C).[6] Similarly, β-Sn nanocrystals can be transformed in solution to $FeSn_2$, PdSn, $CoSn_3$ and $NiSn_3$ by adding the appropriate metal cations (along with sodium borohydride to serve as a reducing agent) and heating at 150-205 °C.[7] Furthermore, it was shown that PtSn nanocrystals could be transformed to Pt_3Sn by addition of Pt^{4+}, and then back to PtSn by addition of Sn^{2+} under reducing conditions.[8] Additionally, ternary intermetallics can be generated by the transformation of Au nanocrystals first to AuCu and then to $AuCuSn_2$ by subsequent addition of metal cations (which are reduced with sodium borohydride) to a polyol reaction.[9]

The second type of solution transformation of metal nanocrystals to binary compounds is via the addition of zero-valent elemental reactants in solution. This strategy has been used by many groups to make metal chalcogenides. For example, the Alivisatos group has made Co_3S_4 and Co_9S_8 by reacting sulfur with a solution of Co nanocrystals.[12-13.] Likewise, they formed CoSe by reacting Co nanocrystals with selenium.[12] Similarly, Gates et al. formed Ag_2Se by reacting Ag nanocrystals with Se.[14] Oxygen is also used as an elemental reactant in nanocrystal transformation, and has been used by many groups[12,15-17] to convert metal nanocrystals into oxides in solution. For example, the Hyeon[16] and O'Brien[17] groups have both formed Cu_2O from Cu nanocrystals by exposing them to ambient oxygen.

As a third variation of solution transformation, metal nanocrystals can be reacted in solution with organometallics or other organoelement compounds to form target materials. For example, Cable et al. reacted diethyl zinc with Au, Cu and Pd nanocrystals to form AuZn, Au_3Zn, Cu_5Zn_8, and PdZn at 220-250 °C.[10] Additionally, Khanna and co-workers have formed InP by reacting colloidal indium with trioctylphosphine (TOP), which serves as a phosphorus source.[18-19] Likewise, Chiang and Chiang have made Ni_2P using a similar strategy.[20]

As is evident by the diversity materials which have already been synthesized using the nanocomposite and solution transformation approaches, there is potential to apply them broadly to other classes of materials. The following chapters detail advancements that serve to expand the scope of applicability of the nanocomposite and the solution transformation routes to classes of materials for which more complex systems are developed or for which little work has been previously reported using these solution-based nanocrystal-directed synthetic strategies.

Chapter II focuses on expanding the nanocomposite route to metal oxides.[21] In this chapter, a library of metal oxide nanoparticles is synthesized using simple, aqueous techniques which then serve as reactive precursors to form ternary metal oxides. Binary metal oxide nanoparticles are mixed in solution to form aggregates that are mixed on the nanoscale, which are isolated, washed, dried, and then annealed at temperatures between 500 and 800 °C to form target ternary metal oxides. This low temperature approach to making solid state materials utilizes mild synthetic techniques and annealing temperatures that are 400-700 °C lower than traditional solid state methods. The lower

reaction temperatures can allow investigation of nucleation events during the formation of these ternary oxides—something impossible to do when following traditional synthetic protocol because of high temperatures. Furthermore, in some cases metastable ternary oxides can be made using this method.

Chapter III highlights the synthesis of a series of rare earth orthoborates using an approach that is similar to the nanocomposite strategy. Amorphous powders precipitated during an aqueous reaction between RE^{3+} and $NaBH_4$ can be annealed in air to form $REBO_3$ at 700 °C. Rare earth borates can have nonlinear optical properties and applications in plasma display panels.[22] This strategy is generalized for many rare earth borates, and evidence suggests that it can be adapted to make multi-metal borates, such as huntite-type $Al_3RE(BO_3)_4$.[23]

Chapter IV explores the reaction by which trioctylphosphine can transform metal nanocrystals into metal phosphides.[24-25] This solution transformation strategy for forming metal phosphides is generalized for many late transition metal phosphides. Changing the reaction temperature can allow access to multiple phases in several metal-phosphorus systems. In some systems, large aggregated metal phosphide products are formed from small nanocrystalline precursors, while in others metal nanocrystal precursor size can be retained in the product. Furthermore, size can have an effect on the morphology of the metal phosphide product, which can be hollow for some systems. These observations suggest a relationship between the size and shape of the precursor and the product.

Chapter V expands the reactivity of trioctylphosphine with metals to include bulk and nanostructured precursors.[25] For example, bulk scale powders, wires and foils can be converted to metal phosphides under similar reaction conditions as those used for nanocrystals in the previous chapter. In some cases, complete reactivity of the bulk-scale precursors is presumed to be inhibited by the larger size of the precursor. Additionally, nanostructured metals such as thin films and patterned substrates can be transformed into their corresponding phosphides. Furthermore, this strategy is applicable towards the conversion of supported metal nanocrystals into metal phosphides. Supported metal phosphides are used as hydrotreating catalysts, and this transformation strategy could provide an alternative, mild method for synthesizing them. Expanding the phosphide conversion method to various types of precursors demonstrates the versatility of the strategy and its potential to be used in materials processing.

Chapter VI rigorously details a proof-of-concept that size and shape can be retained for nanocrystal precursors in metal phosphide conversion reactions.[26] Rh_2P serves as an ideal target for these studies because there are literature reports of Rh nanocrystals with various shapes. Rh cube derivatives, triangle derivatives, and multipods are converted to Rh_2P while retaining the shape of the precursors via reaction with trioctylphosphine in a trioctylphosphine oxide solution at 330-360 °C. Key reaction parameters such as temperature, stabilizing ligands, and co-solvents can be varied to achieve optimal shape retention and product purity. This investigation provides important insights into shape conservation in nanocrystal conversion reactions which could be broadly applied to other classes of materials.

CHAPTER II

LOW-TEMPERATURE NANOPARTICLE-DIRECTED SOLID-STATE SYNTHESIS OF TERNARY TRANSITION METAL OXIDES*

Introduction

Ternary and quaternary transition metal oxides offer a wide variety of important physical properties, including magnetism,[27] superconductivity,[28] ferroelectricity,[29] nonlinear optical behavior,[30] ionic conductivity,[31] and catalytic activity.[32] Like all solid-state materials, the synthetic protocol used to make multi-metal oxides is critical for ensuring optimal performance. These oxides are traditionally synthesized using high-temperature reactions that often require several days of heating because solid-solid diffusion is the rate-limiting step in their formation. As a result, the phases that form are generally thermodynamically stable, and there is little control over the morphology or the kinetics of phase formation. Alternative methods exist for synthesizing metal oxides at low temperatures, including coprecipitation,[33] hydrothermal synthesis,[34] topochemical reactions,[35] and the sol-gel process,[36] and they are generally successful at yielding simple oxides with some control over structure, morphology, and processability. Each of these alternative low-temperature synthetic methods has a particular strength, and often the synthesis of new functional materials is driven by their use.

---

* Reprinted in part with permission from *Chem. Mater., 18*. Henkes, A. E.; Bauer, J. C.; Sra, A. K.; Johnson, R. D.; Cable, R. E.; Schaak, R. E. "Low-Temperature, Nanoparticle-Directed Solid-State Synthesis of Ternary and Quaternary Transition Metal Oxides" 567, Copyright 2006 by the American Chemical Society.

Here we present several strategies for synthesizing a library of binary metal oxide nanoparticles in aqueous solution. This library of metal oxide nanoparticles serves as a robust toolkit of reactants which can be used as precursors for synthesizing bulk-scale ternary metal oxides. This strategy is based on the idea that readily available binary oxide nanoparticles can be combined in known ratios to form nanocomposites and then thermally transformed rapidly and at low temperatures into a predesigned product phase. Since solid-solid diffusion is the rate-limiting step in traditional solid-state reactions, this alternative approach succeeds because it effectively reduces diffusion distances to the nanometer scale and allows reactions to occur much more quickly at relatively low temperatures. This synthetic strategy employs much milder conditions than are required for traditional approaches, and includes water-based mixing of the solid-state precursors and heating temperatures that are often 400-700 °C lower than necessary for conventional high-temperature routes. This approach was originally developed for the low-temperature solution-based synthesis of alloys and intermetallic compounds[4-5] and has yielded insights into reaction pathways and has the potential to generate new structures that are not stable in bulk systems synthesized through traditional methods. Extending this approach to oxides is important because it opens the door to studying low-temperature phase formation and kinetically controlling reaction pathways for these materials. Furthermore, because of the availability of many metal oxide nanoparticles that can serve as precursors,[37] this approach has the potential to be general for a wide range of complex systems.

Experimental Section

Chemicals

Copper(II) acetate monohydrate ($Cu(ac)_2 \cdot H_2O$, 99.9 %), nickel(II) acetate hydrate ($Ni(ac)_2 \cdot xH_2O$, 99+ %), tin(II) chloride ($SnCl_2$, anhydrous, 98 %), titanium(IV) isopropoxide ($Ti(iPrO)_4$, 97+ %), yttrium(III) acetate tetrahydrate ($Y(ac)_3 \cdot 4H_2O$, 99.9 %), europium(III) nitrate hexahydrate ($Eu(NO_3)_3 \cdot 6H_2O$, 99.9 %), cerium(III) nitrate hexahydrate, ($Ce(NO_3)_3 \cdot 6H_2O$, 99.5 %), zinc(II) acetate dihydrate ($Zn(ac)_2 \cdot 2H_2O$, 98+ %), indium(III) nitrate hydrate ($In(NO_3)_3 \cdot xH_2O$, 99.999 %), lanthanum(III) nitrate hexahydrate ($La(NO_3)_3 \cdot 6H_2O$, 99.9 %), aluminum(III) nitrate nonahydrate ($Al(NO_3)_3 \cdot 9H_2O$, 98 %), sodium borohydride ($NaBH_4$, 98 %), and poly(vinylpyrrolidone) (PVP, 40k MW) were used as purchased from Alfa Aesar. Sodium hydroxide (NaOH, pellets) was from EM Science. NANOpure water was obtained by reverse osmosis (18.2 MΩ purity).

Characterization

Powder X-ray diffraction (XRD) data were collected using a Bruker GADDS three-circle X-ray diffractometer (Cu Kα radiation, 40 mV, 40 mA) using microdiffraction powder techniques.[38] The large background at low angles is due to air scattering because the beam size is larger than the sample for the microdiffraction experiments.[38] Transmission electron microscopy (TEM) images, energy-dispersive X-ray spectroscopy (EDS), and selected area diffraction (SAED) patterns were collected on

a JEOL 2010 TEM operating at 200 kV. Samples were prepared by re-suspending the isolated and cleaned nanoparticles in ethanol and dropping the solution on a carbon-coated Cu or Ni grid (chosen to avoid EDS interference with constituent elements in the samples). Differential scanning calorimetry (DSC) and thermal gravimetric analysis (TGA) data were collected on a TA Instruments Q600 SDT under flowing air at a heating rate of 10 °C/min. Elemental analysis for C, H, and N (CHN analysis) was performed by Atlantic Microlabs (Norcross, GA).

Synthesis of Metal Oxide Nanoparticles via Sodium Borohydride Reduction

Cu_2O nanoparticles. Cu_2O was made by dissolving 22.0 g $Cu(ac)_2 \cdot H_2O$ and 100 mg PVP in 15 mL NANOpure water. 10 mg $NaBH_4$ in 10 mL NANOpure water was added dropwise with stirring, which initially formed reduced metal nanoparticles (black), and stirring was allowed to continue for 90 min in air to oxidize the particles (dark green). They were isolated by centrifugation, washed with water and ethanol, and dried at 50 °C in air. Annealing the particles at 500 °C for 1.5 h transformed them from Cu_2O to CuO.

NiO nanoparticles. NiO was prepared in a similar manner, except 21.5 mg $Ni(ac)_2 \cdot xH_2O$ were used and the reaction was only stirred for 15 min. The as-prepared particles (black) were $Ni(OH)_2 \cdot 0.75H_2O$, which transformed to NiO after annealing at 500 °C for 1.5 h.

SnO nanoparticles. SnO was made in a similar manner, except 38.2 mg $SnCl_2$ and 15.7 mg $NaBH_4$ were used. Also, the reaction was boiled for 40 min after addition of $NaBH_4$, which caused the color to change from black to brown.

Synthesis of Metal Oxide Nanoparticles via Hydrolysis of Metal Alkoxides

TiO_2 nanoparticles. TiO_2 was prepared by a hydrolysis reaction. 2.0 mL of 0.0351 M Ti(*i*PrO)$_4$ in 2-propanol were added dropwise to 20 mL of NANOpure water and 100 mg of PVP, immediately causing white particles to precipitate. After stirring for 30 min, the particles were isolated by centrifugation, washed with water and ethanol, and dried in a 50 °C oven. Annealing at 500 °C for 1.5 h in air transformed the as-prepared amorphous particles to crystalline TiO_2. Generally, the TiO_2 particles were used in solution without isolation in subsequent reactions.

Synthesis of Metal Oxide Nanoparticles via Sodium Borohydride-Mediated Precipitation

Y_2O_3 nanoparticles. Y_2O_3 was prepared by dissolving 24.0 mg $Y(ac)_3{\cdot}4H_2O$ and 100 mg PVP in 15 mL NANOpure water. 10 mg $NaBH_4$ in 10 mL NANOpure water was added dropwise with stirring, which immediately precipitated translucent white particles. The solution was stirred for 30 min after addition of $NaBH_4$, and then the particles were isolated by centrifugation, washed with water and ethanol, and dried in air at 50 °C. Annealing at 500 °C for 1.5 h in air crystallized the particles into white Y_2O_3.

Eu_2O_3 nanoparticles. Eu_2O_3 nanoparticles were prepared in the same manner, except 34.0 mg of $Eu(NO_3)_3 \cdot 6H_2O$ was used. The as-prepared particles were also translucent white and turned opaque white when dried and annealed.

CeO_2 nanoparticles. CeO_2 was prepared in the same manner, except 36.0 mg $Ce(NO_3)_3 \cdot 6H_2O$ were used and the as-prepared particles (yellow) did not require annealing to form CeO_2; however, annealing at 700 °C for 1 h in air further crystallized the product.

ZnO nanoparticles. ZnO was prepared in the same manner, except 47.6 mg $Zn(ac)_2 \cdot 2H_2O$ were used and the as-prepared particles (white) did not require annealing to crystallize ZnO.

Synthesis of Metal Hydroxide Nanoparticles via Sodium Hydroxide-Mediated Precipitation and Transformation into Metal Oxides

In_2O_3 nanoparticles. $In(OH)_3$ was prepared by dissolving 31.5 mg $In(NO_3)_3 \cdot xH_2O$ and 100 mg PVP in 40 mL NANOpure water. A 5 mL volume of 0.08 M NaOH (aq.) was added and the solution was boiled for 30 min, which precipitated white particles. After cooling, they were isolated by centrifugation, washed with water and ethanol, and dried in air at 50 °C. Annealing at 700 °C for 90 min in air transformed the as-prepared $In(OH)_3$ to In_2O_3.

La_2O_3 nanoparticles. $La(OH)_3$ was prepared in the same manner, except 48.6 mg $La(NO_3)_3 \cdot 6H_2O$ was used and the solution was boiled for 45 min. Annealing at 700 °C for 1 h in air transformed the as-prepared $La(OH)_3$ to La_2O_3.

Al_2O_3 nanoparticles. $Al(OH)_3$ was formed in the same manner, except 44.8 mg $Al(NO_3)_3 \cdot 9H_2O$ was used. Although it was not annealed, it is presumed based on protocol and other data (not shown) that annealing in air would form Al_2O_3.

Formation of Nanocomposites and Subsequent Conversion into Ternary Oxides

$Y_2Ti_2O_7$. Two procedures were used to form $Y_2Ti_2O_7$. First, approximately 5.6 mg of Y_2O_3 and approximately 8.0 mg of TiO_2 nanoparticle powders (as-synthesized) were re-dispersed in 40 mL of NANOpure water and stirred for 30 min, and the precipitate (Y_2O_3:TiO_2 nanocomposite, 1:2 ratio) was isolated by centrifugation. In a slight modification of this procedure, Y_2O_3:TiO_2 nanocomposites could also be made by adding $Ti(i\text{OPr})_4$ (2.0 mL, 0.0351 M in 2-propanol) to the as-synthesized Y_2O_3 nanoparticle solution, essentially forming TiO_2 nanoparticles in situ in the presence of Y_2O_3 nanoparticles. (TEM analysis confirmed the presence of a Y_2O_3:TiO_2 nanoparticle composite identical to the one formed by physically mixing Y_2O_3 and TiO_2 nanoparticles.) In both cases, pyrochlore-type $Y_2Ti_2O_7$ could be accessed by annealing at 700 °C for 2 h in air.

$Eu_2Ti_2O_7$. Eu_2O_3:TiO_2 nanocomposites were formed in situ from the hydrolysis reaction of Ti(*i*OPr)$_4$ in a solution of as-prepared Eu_2O_3 nanoparticles. Annealing at 800 °C for 2 h in air to formed $Eu_2Ti_2O_7$.

$NiTiO_3$. NiO:TiO_2 nanocomposites were formed in situ from the hydrolysis reaction of Ti(*i*OPr)$_4$ in a solution of as-prepared NiO nanoparticles (1:1 ratio). Annealing at 700 °C for 1 h in air to formed $NiTiO_3$.

Zn_2SnO_4. A 2:1 ratio of ZnO:SnO nanoparticles were suspended in 40 mL ethanol and stirred for 15 min, forming a composite (tan). The composite was isolated by centrifugation and dried at 50 °C in air. The dried ZnO:SnO composite was annealed at 700 °C for 3 h in air, forming Zn_2SnO_4 with slight SnO_2 and ZnO impurities.

$CuInO_2$. Cu_2O nanoparticles dispersed in 2 mL ethanol were added dropwise to a stirring solution of In(OH)$_3$ nanoparticles dispersed in 20 mL ethanol, forming a Cu_2O:In(OH)$_3$ nanocomposite (1:2 ratio). The solution was stirred for 30 min before the nanocomposite was isolated by centrifugation and allowed to dry in ambient conditions. The dried Cu_2O:In(OH)$_3$ composite was annealed at 800 °C for 2 h in an argon atmosphere, forming $CuInO_2$ with slight In_2O_3 and Cu_2O impurities.

Results and Discussion

Synthesis of Metal Oxide Nanoparticles and Precursors

While there are many methods reported in the literature for synthesizing metal oxide nanoparticles,[39] we chose to design a library of metal oxide nanoparticles that were simple to access using mild, aqueous bench-top techniques. To utilize the metal oxide nanoparticles as precursors in the synthesis of multimetal oxides, rigorous size- and shape-control is not necessary. In this case, four distinct methods were used; however, many others could be employed to access oxide nanoparticles from other areas of the periodic table and with precise control over size and morphology.[39] The first method involved oxidation of metal nanoparticles in solution in ambient condition following similar protocol reported by others for making Cu_2O by slowly oxidizing Cu nanocrystals.[16,40] In this case, zero-valent metal nanoparticles were synthesized by reducing metal salts in aqueous solution using sodium borohydride in the presence of PVP (a stabilizing agent) followed by oxidation by air in solution to form metal oxide nanoparticles (Cu_2O, NiO and SnO) as shown by powder XRD in Figure 3a-c. For the case of NiO, the as-prepared particles are $Ni(OH)_2 \cdot 0.75H_2O$ with residual unoxidized Ni (Figure 3b, top) and can be transformed to NiO upon annealing at 500 °C for 1 h (Figure 3b, bottom). The second method involved the formation of TiO_2 nanoparticles via hydrolysis of titanium isopropoxide in water in the presence of PVP based on sol-gel methods.[41] The as-prepared TiO_2 particles are amorphous (as evidenced by the broad

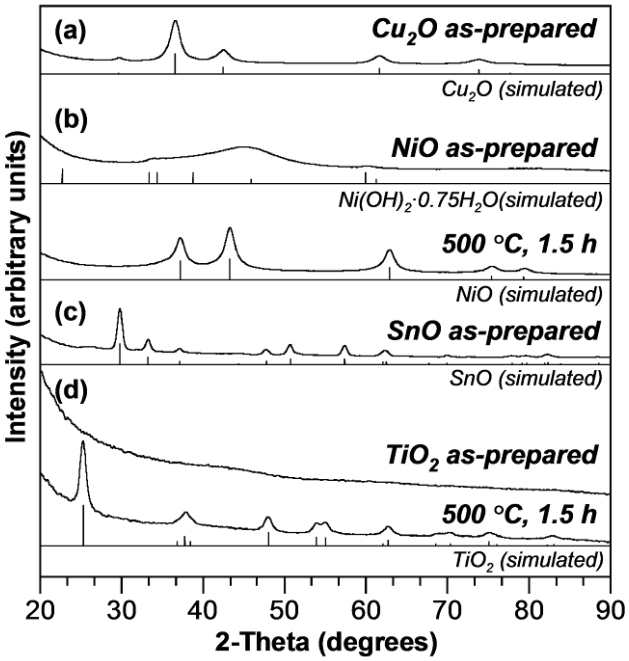

Figure 3. Powder XRD patterns for (a) Cu_2O, (b) NiO (intense peak at ~ 45 degrees for as-prepared NiO is due to un-oxidized Ni) and (c) SnO nanoparticles formed by oxidation of zero-valent metals in aqueous solution by air and (d) TiO_2 nanoparticles formed by hydrolysis of Ti(*i*OPr)$_4$ in water.

features in the XRD pattern in Figure 3d, top), but annealing at 500 °C crystallizes anatase TiO_2 (Figure 3d, bottom). A third method involved the precipitation of metal oxide nanoparticles mediated by aqueous sodium borohydride (XRD, Figure 4). Enhanced crystallinity was seen for Y_2O_3 and Eu_2O_3 by powder XRD after annealing the as-prepared particles at 500 °C in air (Figure 4a-b). The final method involved the formation of metal hydroxide nanoparticles ($In(OH)_3$, $La(OH)_3$, $Al(OH)_3$ powder XRD patterns shown in Figure 5) in aqueous solution in the presence of NaOH, which could be thermally transformed to metal oxide nanoparticles (powder XRD patterns shown for $In(OH)_3$ and $La(OH)_3$ in Figure 5a-b). Stoichiometric combinations of these metal oxide

nanoparticles and metal oxide precursors could be mixed in solution to form nano-mixed composites, and then thermally transformed to ternary oxides by annealing in air at temperatures between 700 and 800 °C for 1-3 h.

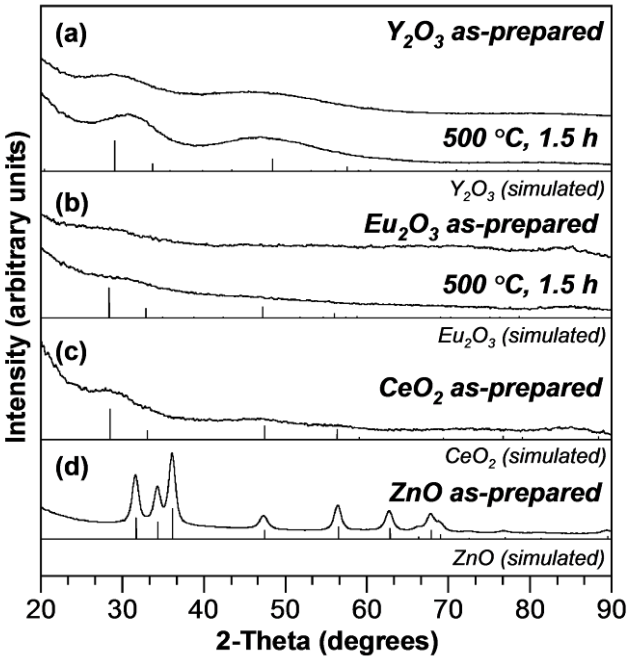

Figure 4. Powder XRD patterns for (a) Y_2O_3, (b) Eu_2O_3, (c) CeO_2 and (d) ZnO nanoparticles formed by $NaBH_4$-mediated precipitation from aqueous solution.

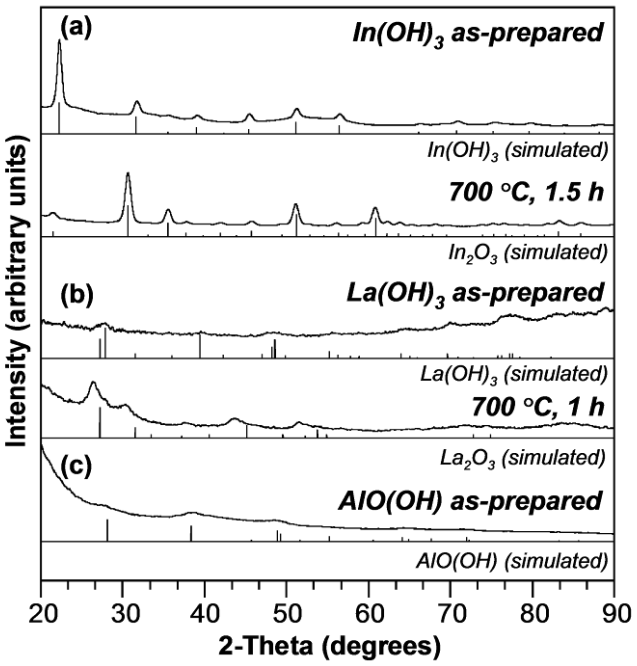

Figure 5. Powder XRD patterns for (a) $In(OH)_3$, (b) $La(OH)_3$, and (c) $Al(OH)_3$ nanoparticles formed by NaOH-mediated precipitation from aqueous solution, which could be thermally transformed to their respective metal oxides.

Synthesis of Metal Oxide Nanocomposites and Transformation to Multi-Metal Oxides

As an initial demonstration of the applicability of the nanoparticle precursor route to multi-metal oxides, we focused on pyrochlore-type $Y_2Ti_2O_7$. Titanate pyrochlores are important oxides with properties that include geometric magnetic frustration[42] and high-T_c ferroelectricity,[29] and $Y_2Ti_2O_7$ in particular shows ionic conductivity when appropriately doped.[43] $Y_2Ti_2O_7$ is traditionally synthesized by heating mechanically mixed powders of Y_2O_3 and TiO_2 to temperatures above 1200 °C for 1-3 days.[44] Alternative methods for synthesizing $Y_2Ti_2O_7$[45-47] have yielded products that either contain significant amounts of organic residue, are limited to thin films, or

require long reaction times to yield a phase-pure product. With use of our nanoparticle-directed strategy, bulk-scale $Y_2Ti_2O_7$ can be formed within 2 h of heating at 700 °C.

Figure 6a shows powder XRD data for Y_2O_3 and TiO_2 nanoparticles stabilized by PVP that were synthesized using techniques discussed previously. The Y_2O_3 and TiO_2 nanoparticles appear to be amorphous as synthesized at room temperature, but upon annealing them to 500 °C, they crystallize to form phase-pure cubic Y_2O_3 (Figure 4a) and anatase TiO_2 (Figure 3d), as expected. When redispersed in water in a 1:2 molar ratio of Y_2O_3:TiO_2, a nanocomposite forms and precipitates out of solution. The initial mass is not all recovered, indicating that the nanocomposite formation is not quantitative, although, in most cases, the nominal ratio of nanoparticles mixed together agrees well with the actual composition of the precipitated nanocomposite. In most cases, the individual nanoparticles will precipitate out of solution over time, regardless of whether they have been mixed with other types of nanoparticles. We speculate that the solution mixing, combined with known interactions of polymers in solution, homogenizes the nanoparticles, effectively mixing them at the 10-100 nm scale and allowing them to coprecipitate in a reasonably homogeneous fashion. The precipitated nanocomposite was found by EDS analysis to have an average Y:Ti stoichiometry of 1.1:1.0, which is close to that of the relative ratios of the Y_2O_3 and TiO_2 nanoparticles in solution. In addition, TGA analysis in air indicates that the nanocomposite contains 25-30 wt % PVP. The XRD pattern (Figure 6a) for the Y_2O_3:TiO_2 nanocomposite has broad peaks that generally match those expected for a mixture of amorphous Y_2O_3 and TiO_2.

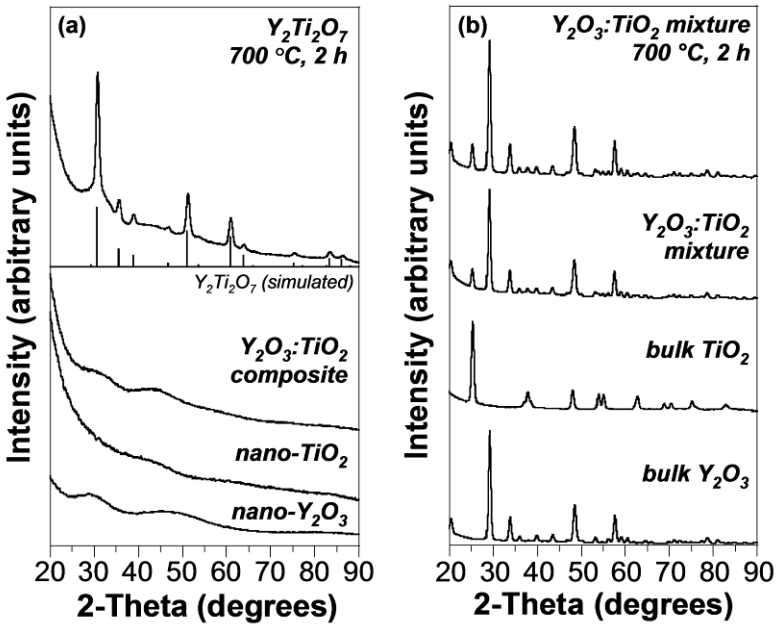

Figure 6. (a) Powder XRD patterns for Y_2O_3 and TiO_2 nanoparticles, a 1:2 Y_2O_3:TiO_2 nanocomposite, and the nanocomposite heated to 700 °C for 2 h to form pyrochlore-type $Y_2Ti_2O_7$ (top XRD pattern). The simulated XRD pattern for $Y_2Ti_2O_7$, based on PDF card no. 42-0413, is shown for comparison. (b) For comparison, analogous XRD data for bulk-scale (micrometer-size) samples of Y_2O_3, TiO_2, a mechanically mixed Y_2O_3-TiO_2 sample, and the 1:2 Y_2O_3:TiO_2 mixture heated to 700 °C for 4 h. No appreciable reaction is observed under similar heating conditions to those used in (a).

Figure 7 shows transmission electron microscopy (TEM) images of the nanoparticles and nanocomposite. The Y_2O_3 system (Figure 7a) appears as a network of irregularly shaped nanoparticles with diameters that range from 5 to 15 nm. The selected-area electron diffraction (SAED) pattern (Figure 7a, inset) is very diffuse, which is consistent with the broad XRD pattern and indicates an amorphous structure. The TiO_2 nanoparticles, shown in Figure 7b, generally form larger 20-50 nm blocks which, upon closer inspection, are comprised of 1-3 nm particles. The SAED pattern is

almost featureless, also indicating an amorphous structure. The Y_2O_3:TiO_2 nanocomposite (Figure 7c) formed in solution from the aggregation of the PVP-stabilized Y_2O_3 and TiO_2 nanoparticles shows a mixture of the interconnected Y_2O_3 nanoparticles and the aggregated TiO_2 nanoparticles (enlarged view of the TiO_2 region is shown in Figure 7d). EDS confirms the presence of both Ti and Y in a 1.0:1.1 ratio, and the SAED pattern (Figure 7e) shows primarily the diffraction pattern expected for Y_2O_3, with extra diffuse intensity like that observed for TiO_2.

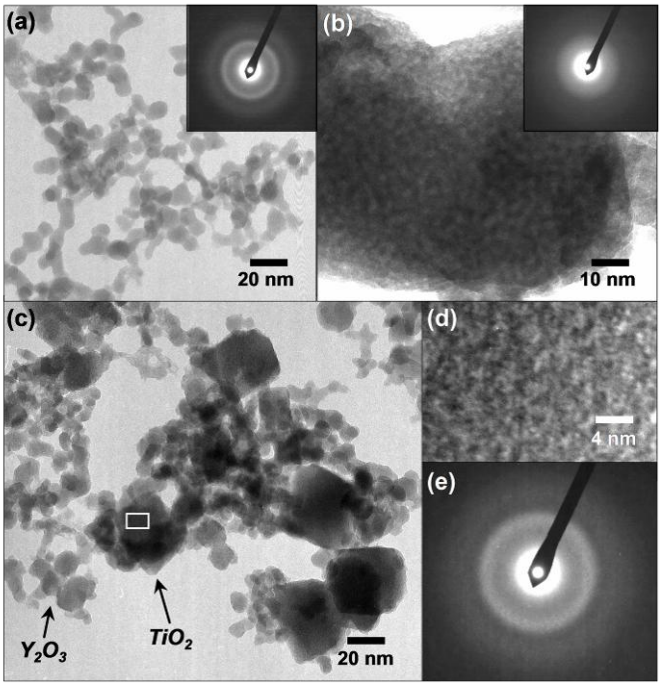

Figure 7. TEM micrographs of (a) Y_2O_3 nanoparticles, (b) TiO_2 nanoparticles, and (c) the Y_2O_3:TiO_2 nanocomposite showing components consistent with both Y_2O_3 and TiO_2. An enlargement of the region marked by a box in (c) is shown in (d), and it matches the aggregated structure observed for TiO_2 nanoparticles. SAED patterns for the Y_2O_3 and TiO_2 nanoparticles are shown as insets in (a) and (b), and the SAED pattern for the nanocomposite is shown in (e).

When the nanocomposite is heated to 700 °C for 2 h in air, the resulting XRD pattern (Figure 6a) matches that expected for pyrochlore-type $Y_2Ti_2O_7$ (PDF card no. 42-0413). The resulting powder (Figure 8) is nanocrystalline, with 50-100 nm grains. Importantly, elemental analysis for carbon, hydrogen, and nitrogen indicates that 100 % of the polymer residue is removed (via oxidation) during the heating process, leaving a product that is free of organic impurities.

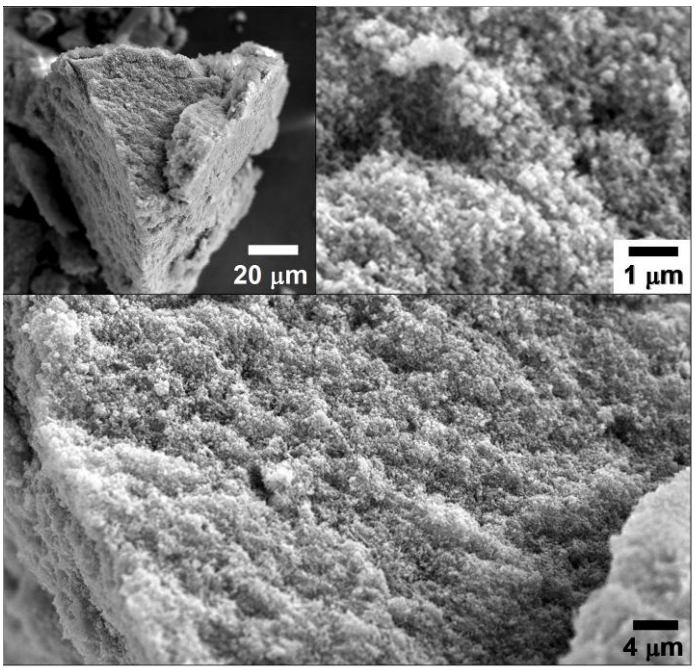

Figure 8. SEM micrographs (three magnifications of the same sample) for nanocrystalline pyrochlore-type $Y_2Ti_2O_7$ powder prepared by heating a 1:2 Y_2O_3:TiO_2 nanocomposite to 700 °C for 2 h.

In contrast to the nanoparticle-directed synthesis of $Y_2Ti_2O_7$, which yields a crystalline pyrochlore phase at temperatures as low as 700 °C, the traditional high-temperature ceramic method is virtually unreactive at these temperatures. Figure 6b

shows powder XRD data for micrometer-scale Y_2O_3 and TiO_2 powders, as well as the 1:2 physical mixture of Y_2O_3 and TiO_2. When the mixture of micrometer-scale Y_2O_3 and TiO_2 powders are heated to 700 °C for several hours, no reaction is detected (Figure 6b). This clearly shows the enhanced reactivity afforded by the nanoparticle precursors, which decrease diffusion distances by several orders of magnitude and virtually eliminate solid-solid diffusion as the rate-limiting step.

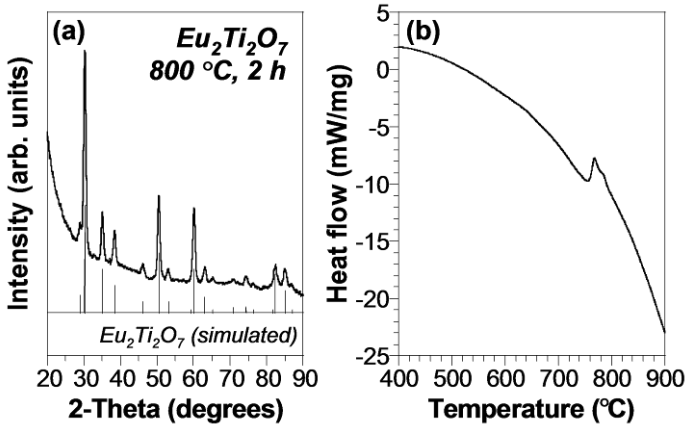

Figure 9. (a) XRD pattern for the pyrochlore-type $Eu_2Ti_2O_7$ product formed by heating a Eu_2O_3:TiO_2 nanocomposite to 800 °C for 1 h. The simulated XRD pattern is shown for comparison. (b) DSC trace (in air) for a 1:2 Eu_2O_3:TiO_2 nanocomposite, showing an exotherm near 765 °C that corresponds to the crystallization of pyrochlore-type $Eu_2Ti_2O_7$.

Similarly, phase-pure pyrochlore-type $Eu_2Ti_2O_7$ can be prepared by heating a composite of Eu_2O_3 and TiO_2 nanoparticles (1.0:1.1 average Eu:Ti stiochiometry according to EDS analysis) to 800 °C for 2 h (Figure 9a). Interestingly, the differential scanning calorimetry (DSC) trace for the Eu_2O_3:TiO_2 nanocomposite (Figure 9b) shows an exotherm at 765 °C. (The Y_2O_3:TiO_2 nanocomposite shows similar features.)

Previous calorimetry studies of ball-milled $RE_2Ti_2O_7$ (*RE* = rare earth) attribute this exotherm to atomic ordering that forms the pyrochlore lattice.[45] For traditional bulk powders, this feature is not observed because diffusion is not complete on the time scale of the calorimetry experiment. However, RE_2O_3:TiO_2 powders that are broken into smaller pieces and homogenized by extensive mechanical milling show similar exotherms.[43] Thus, observation of this exotherm in our samples is further evidence of solution-mediated nanocomposite formation and its role in supporting rapid thermal interdiffusion of the reagents to nucleate $Eu_2Ti_2O_7$ and $Y_2Ti_2O_7$.

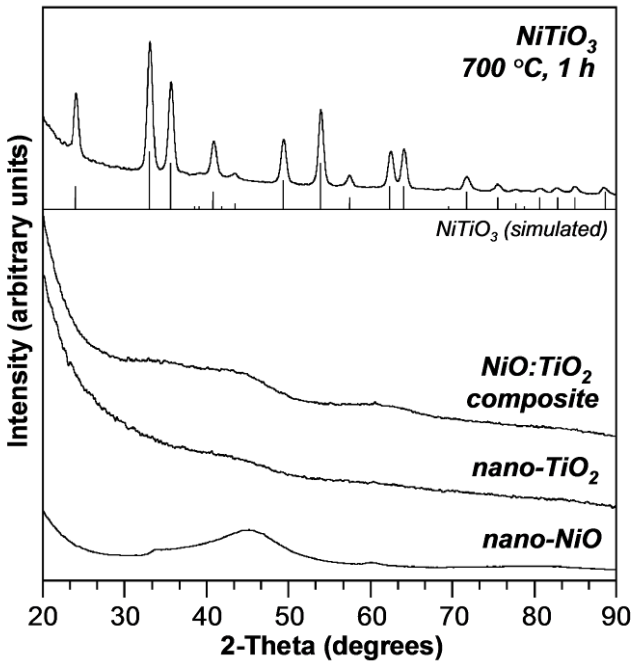

Figure 10. Powder XRD patterns for nano-NiO and nano-TiO_2 (bottom), the NiO:TiO_2 composite formed from them (middle), and $NiTiO_3$ formed from annealing the nanocomposite at 700 °C in air for 1 h (top). Simulated XRD pattern for $NiTiO_3$ is shown below experimental data.

In addition to $Y_2Ti_2O_7$ and $Eu_2Ti_2O_7$, other ternary oxides can be accessed using this method. For example, Figure 10 shows the XRD pattern for ilmenite-type $NiTiO_3$ that was synthesized from a composite containing nanoparticles of NiO and TiO_2. $NiTiO_3$ is typically synthesized at 1000-1400 °C,[48] and while a few lower temperature methods have been reported,[49] they generally contain significant amounts of impurities. Here, we accessed phase-pure $NiTiO_3$ by heating a NiO:TiO_2 nanocomposite to 700 °C for 1 h. Additionally, Zn_2SnO_4 can be accessed by heating a composite of ZnO and SnO nanoparticles at 700 °C in air for 3 h, although precursor impurities remain (Figure 11a). Other efforts using this strategy have resulted in the formation of Bi_2CuO_4 from a Bi_2O_3:Cu_2O nanocomposite and ilmenite-type $CoTiO_3$ from a CoO:TiO_2 nanocomposite. Furthermore, the strategy can be used to form quaternary metal oxides, such as aurivillius-type $Bi_5FeTi_3O_{15}$[50] from a Bi_2O_3:Fe_2O_3:TiO_2 nanocomposite. This suggests that a variety of compositionally and structurally complex oxides could be formed as nanocrystalline powders at low temperatures using this strategy. Accessible complex metal oxide phases and their required thermal transformation conditions are shown in Table 1.

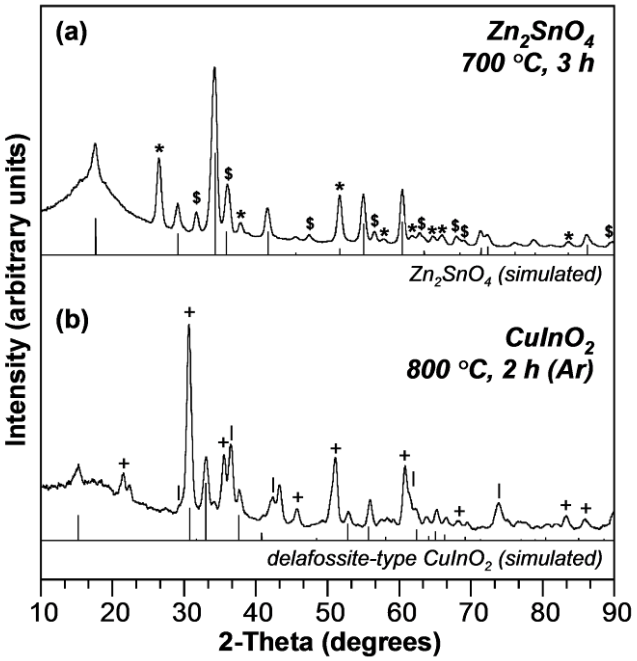

Figure 11. Powder XRD patterns for (a) Zn_2SnO_4 with ZnO and SnO_2 impurities (indicated by $ and *, respectively) formed from a ZnO:SnO nanocomposite annealed at 700 °C in air for 3 h, and (b) delafossite-type $CuInO_2$ with Cu_2O and In_2O_3 impurities (indicated by | and +, respectively) formed from a Cu_2O:$In(OH)_3$ nanocomposite annealed at 800 °C in argon for 2 h.

Moreover, it is of significant utility that Cu_2O forms when Cu nanoparticles are oxidized in solution in ambient conditions. Cuprite Cu_2O, which is a high-symmetry cubic phase, forms preferentially over tenorite CuO (monoclinic) when face centered cubic Cu nanocrystals are oxidized because oxygen atoms easily diffuse into the Cu lattice without disrupting the cubic symmetry.[40] Hence, the air-stable Cu_2O nanoparticles can be used as a precursor for the formation of delafossite-type $CuInO_2$, in which Cu is in the 1+ oxidation state. $CuInO_2$, a transparent conducting oxide, can be challenging to synthesize by traditional solid state techniques due to its low decomposition temperature.[51] Careful heat treatment of a Cu_2O:$In(OH)_3$ nanocomposite

in an argon atmosphere at 800 °C for 2 h forms $CuInO_2$ (Figure 11b). Although both Cu_2O and In_2O_3 impurities are present (either due to incomplete reaction or product decomposition), the formation of $CuInO_2$ is an important observation supporting the versatility and breadth of synthetic utility of this nanocomposite conversion strategy.

Table 1. Multimetal oxides formed using the nanocomposite strategy.

Complex metal oxide	Nanocomposite components	Formation conditions
$Y_2Ti_2O_7$	Y_2O_3:TiO_2	700 °C, 2 h, air
$Eu_2Ti_2O_7$	Eu_2O_3:TiO_2	800 °C, 2 h, air
$NiTiO_3$	NiO:TiO_2	700 °C, 1 h, air
$CoTiO_3$	CoO:TiO_2	700 °C, 2 h, air
Bi_2CuO_4	Bi_2O_3:Cu_2O	500 °C, 2 h, air
$Bi_5FeTi_3O_{15}$	Bi_2O_3:Fe_2O_3:TiO_2	700 °C, 2 h, air
Zn_2SnO_4	ZnO:SnO	700 °C, 3 h, air
$CuInO_2$	Cu_2O:$In(OH)_3$	800 °C, 2 h, argon

Conclusions

In summary, we have developed a library of metal oxide nanoparticles easily synthesized in aqueous solution, which can be used as reactive precursors to form multimetallic oxides. Mixing various metal oxides nanoparticles in solution in known ratios can form nano-mixed precursors that rapidly transform, at low temperatures and under mild conditions, into complex ternary oxides. This presents a new low-temperature approach for synthesizing nanocrystalline oxides that is distinct from other

methods. In all cases, this approach can nucleate complex crystalline oxides at temperatures that are equal to or lower than the crystallization temperatures observed using other methods. Of importance, creating nano-mixed precursors potentially affords kinetic control of the product so that metastable phases such as $CuInO_2$[27] can be accessed. While most of our target compounds can be prepared by other methods such as coprecipitation, the use of nanoparticles as precursors opens up new possibilities for solution-based materials processing applications, control of nanocrystalline morphology, and careful studies of diffusion and nucleation events in nanoscale oxide materials. Accordingly, in analogy to our previous work with alloys and intermetallic compounds,[4-5] it may prove possible to study reaction pathways, separate diffusion and nucleation events, template nanostructured materials using solution infiltration routes, and synthesize new and metastable phases in bulk-scale oxide systems using this approach. Modifications to this approach may also provide insight into the size dependence of crystallization temperatures for complex oxides, carefully tuning the composite homogeneity from nearly atomic-level mixing (e.g., coprecipitation) to the micrometer-scale mixing of traditional ceramic samples since many metal oxide nanoparticle precursors can be made as size-controlled nanocrystals with dimensions that span several orders of magnitude.[39] Finally, this work demonstrates that the same synthetic concept can be applied to both oxides and reduced multi-metallic compounds and suggests that this strategy may be general for many other classes of solid-state materials.

CHAPTER III

A SOLUTION-MEDIATED STRATEGY FOR SYNTHESIZING *RE*BO_3 (*RE* = Y, Nd, Sm, Eu, Gd, Ho) USING SODIUM BOROHYDRIDE AS A BORON SOURCE

Introduction

Due to their crystallographic noncentrosymmetry, metal borates can exhibit nonlinear optical properties.[52] While bulk-scale single crystals of nonlinear optical materials are most commonly used in optics, polycrystalline nonlinear optical materials are gaining increased attention as candidates for use in nonlinear optical application due to an increased efficiency for optical frequency conversion caused by constructive interference.[53] A technological limitation of polycrystalline materials is the ability to maintain the narrow range of wavelengths emitted, which can be influenced by crystal defects and crystal field symmetry.[22,54-55] Nano- and microcrystalline rare earth borates have been made by a variety of synthetic methods, including solvothermal reactions,[22,56-59] spray pyrolosis,[60] single-source precursor decomposition,[54,61] and sol-gel synthesis.[62] By decreasing their size to the nano-regime, rare earth borates could have applications as biological fluorescence labels and could provide higher resolution as phosphor components in plasma display panels.[59] However, as a consequence of their nanocrystalline size, low crystallinity and surface defects can decrease the luminescence intensity. Therefore, an ideal size-range exists where rare earth borate nanocrystals can retain optimal luminescence properties, which varies depending on reaction conditions.

In this chapter we describe an alternative method for forming *RE*BO_3 (*RE* = Y, Nd, Sm, Eu, Gd, Ho) where an amorphous gel-like precipitate forms in an aqueous solution of RE^{3+} following the addition of aqueous $NaBH_4$ in the presence of a stabilizing polymer. The dried precipitate is annealed at 700 °C to form *RE*BO_3. Using this method we are able to form a nanostructured YBO_3:Eu powder (a technologically relevant red phosphor[22,54,59,62]) that has comparable emission properties to high quality nanocrystals prepared by solvothermal methods. Furthermore, preliminary results suggest that it is possible to extend this strategy to form multi-metal borates, such as huntite-type $Al_3Gd(BO_3)_4$. This simple and general method could be used for forming application-directed nanostructured materials, such as thin films and patterned surfaces.

Experimental Details

Chemicals

All chemicals were used as purchased. Poly(vinylpyrrolidone) (40k MW, PVP) was from Aldrich. Sodium borohydride ($NaBH_4$, 98 %), yttrium(III) acetate tetrahydrate ($Y(ac)_3{\cdot}4H_2O$, 99.9 %), europium(III) nitrate hexahydrate ($Eu(NO_3)_3{\cdot}6H_2O$, 99.9 %), yttrium(III) chloride hydrate ($YCl_3{\cdot}xH_2O$, 99.9 %), gadolinium(III) acetate hydrate ($Gd(ac)_3{\cdot}xH_2O$, 99.9 %) and aluminum(III) nitrate nonahydrate ($Al(NO_3)_3{\cdot}9H_2O$, 98 %) were from Alfa Aesar. Neodymium(III) nitrate hexahydrate ($Nd(NO_3)_3{\cdot}6H_2O$, 99.9 %), samarium(III) nitrate hexahydrate ($Sm(NO_3)_3{\cdot}6H_2O$, 99.9 %), and holmium(III) nitrate

pentahydrate ($Ho(NO_3)_3 \cdot 5H_2O$, 99.9 %) were from K & K Labs. NANOpure water was obtained by reverse osmosis (18.2 MΩ purity).

Characterization

Powder X-ray diffraction (XRD) data were collected using a Bruker GADDS three-circle X-ray diffractometer (Cu Kα radiation, 40 mV, 40 mA) using microdiffraction powder techniques.[38] Transmission electron microscopy (TEM) images, energy-dispersive X-ray spectroscopy (EDS), and selected area diffraction (SAED) patterns were collected on a JEOL 2010 TEM operating at 200 kV. Samples were prepared by re-suspending the isolated nanoparticles in ethanol and dropping the solution on a carbon-coated Ni grid. Scanning electron microscopy (SEM) was performed using an Electroscan ESEM-E3 scanning electron microscope operating at 15 kV. Metal borate powders were prepared for SEM by coating with AuPd using a metal sputter coater. Differential scanning calorimetry (DSC) and thermal gravimetric analysis (TGA) data were collected on a TA Instruments Q600 SDT under flowing air at a heating rate of 10 °C/min. UV absorbance and emission spectra were collected using a Photon Technology International (PTI) fluorimeter with a xenon lamp with a scan rate of 1 nm/s. ATR-IR spectroscopy was performed using a Bruker TENSOR 27 ATR from 600-4000 cm^{-1}.

Synthesis of Amorphous Rare Earth Oxide-Boron Powders and Transformation to Crystalline *RE*BO_3

Typically, 25-30 mg of each rare earth salt was dissolved in 30 mL NANOpure water with 100 mg PVP in an Erlenmeyer flask. After stirring vigorously in air for 15 min, a chilled 10 mL solution of 0.03-0.09 M $NaBH_4$ (aq) was added dropwise, causing bubbling and often the immediate precipitation of translucent particles. After stirring for 30-60 min, a translucent gel-like precipitate was isolated via centrifugation at 13k rpm. The precipitate was not washed so that residual BH_4^- would remain incorporated into the recovered precipitate. It was dried in a 50 °C oven. Dried powders were opaque, dense and white except in the case of Ho (pink) and Nd (purple). The as-prepared dried powders were annealed in air at 700 °C for 90-120 min to form *RE*BO_3. Specific details for each metal borate system are listed below in Table 2.

Table 2. Synthetic details for the formation of amorphous *RE*-B powders and transformation to *RE*BO_3.

RE^{3+} precursor(s)	$NaBH_4$ in 10 mL H_2O	Heat treatment	Product
25.5 mg $Y(ac)_3 \cdot 4H_2O$	10.5 mg	700 °C, 90 min	orthoborate YBO_3
22.8 mg $Eu(NO_3)_3 \cdot 6H_2O$	13.9 mg	700 °C, 90 min	orthoborate $EuBO_3$
35.2 mg $Nd(NO_3)_3 \cdot 6H_2O$	32.0 mg	700 °C, 2 h	hexagonal $NdBO_3$
35.4 mg $Sm(NO_3)_3 \cdot 6H_2O$	21.4 mg	700 °C, 2 h	orthoborate $SmBO_3$
26.2 mg $Gd(ac)_3 \cdot xH_2O$	32.6 mg	700 °C, 90 min	orthoborate $GdBO_3$
35.3 mg $Ho(NO_3)_3 \cdot 5H_2O$	30.9 mg	700 °C, 90 min	orthoborate $HoBO_3$
2.2 mg $Eu(NO_3)_3 \cdot 6H_2O$ + 15.8 mg $Y(ac)_3 \cdot 4H_2O$ (or 11.7 mg $YCl_3 \cdot xH_2O$)	14.0 mg	700 °C, 2 h	orthoborate YBO_3:Eu

Synthesis of Amorphous Rare Earth Oxide-Aluminum Oxide-Boron Powders and Transformation to Huntite-Type $Al_3RE(BO_3)_4$

To synthesize huntite-type borate powders, 22.5 mg $Gd(ac)_3 \cdot xH_2O$ or 24.2 mg $Sm(NO_3)_3 \cdot 6H_2O$ was mixed with 62.2 mg $Al(NO_3)_3 \cdot 9H_2O$ and 250 mg PVP in 30 mL NANOpure water. After stirring for 15 min, 51.0 mg $NaBH_4$ in 10 mL NANOpure water was added dropwise, causing the solution to bubble and translucent, gel-like particles to precipitate. After stirring for 1 h, the precipitate was isolated via centrifugation, then dried in a 50 °C oven. The dried powders were annealed at 800 °C in air for 2 h to form $Al_3Gd(BO_3)_4$ and $Al_3Sm(BO_3)_4$ with oxide impurities.

Results and Discussion

When aqueous sodium borohydride is added to a solution of Eu^{3+} and PVP in water, the solution changes from clear and colorless to murky, and a translucent gel-like precipitate forms. Under dry reaction conditions, spectroscopic evidence suggests the formation of tetrahydroborate polymeric solid state structures for some lanthanides in which BH_4^- bridges two metal atoms.[63] The stability of these networks is influenced by how easily the metal cation can be reduced by BH_4^-.[63] In the case of the rare earths, which have a more negative reduction potential than BH_4^-,[63] the tetrahydroborate complexes are stable and unreactive. Based on the byproducts from the reaction of BH_4^- with water[64] and the known interactions of RE^{3+} ions with BH_4^-,[63] we hypothesize that a polymeric network is forming in solution. It is our hypothesis that BH_4^- and other

byproducts from the reaction of BH_4^- with water bridge RE^{3+} cations to form polymeric networks that precipitate out of aqueous solution as a gel-like solid. ATR-FTIR spectroscopy was used to confirm the presence of B-O and B-H groups in the as-prepared samples. Stretches in the region of 1200-1500 cm^{-1} can correspond to both B-O and bridging B-H moieties in the as-prepared powder (Figure 12, top).[63,65] When annealed to form $EuBO_3$, the stretches in this region decrease in intensity and a new group of signals appears in the 800-1000 cm^{-1} region corresponding to B-O stretches in vaterite-type $EuBO_3$ (Figure 12, bottom).[66]

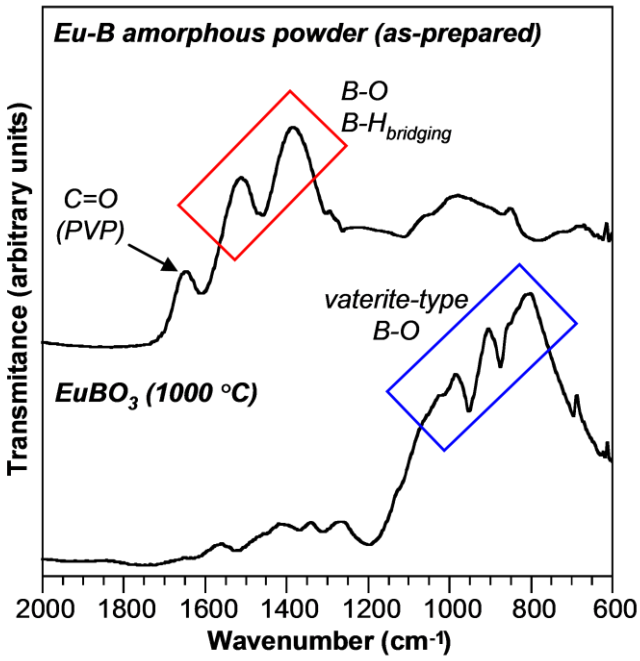

Figure 12. ATR-IR spectra for as-prepared powder from $Eu(NO_3)_3$ and $NaBH_4$ (top) and $EuBO_3$ (bottom) after annealing the as-prepared powder at 1000 °C (ensuring burn-off of PVP). Red and blue boxes indicate regions where B-O and $B\text{-}H_{bridging}$ stretches and vaterite-type B-O stretches are observed, respectively.

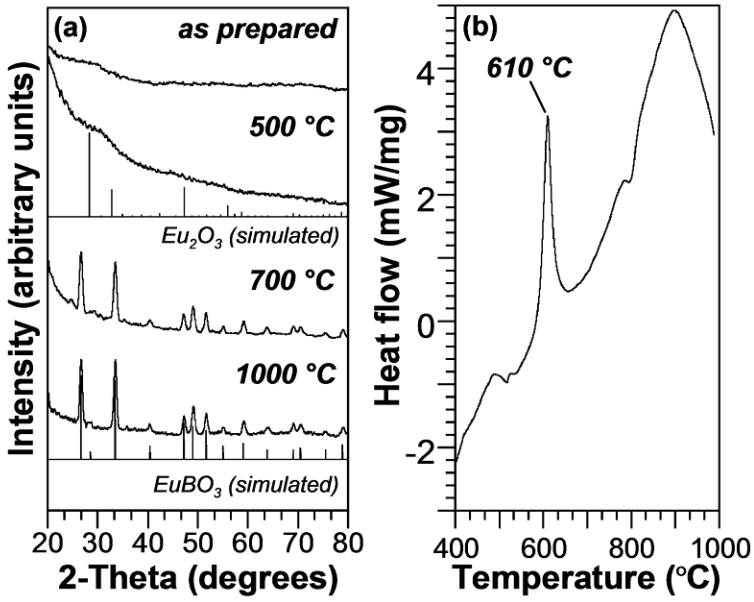

Figure 13. (a) Powder XRD patterns for the synthesis of $EuBO_3$ from an amorphous Eu-B powder. The as-prepared powder (top) was annealed at 500 °C, 700 °C and 1000 °C in air. $EuBO_3$ was formed at 700 °C. (b) DSC trace for the as-prepared powder collected under flowing air showing an exotherm at 610 °C, correlating to the crystallization of orthoborate $EuBO_3$.

After isolation of the gel via centrifugation and dehydrating at 50 °C, the as-prepared powder can be transformed into $EuBO_3$ by thermal treatment in air. As seen in Figure 13a, the as-prepared powder (top) is amorphous by powder XRD. Heating it to 500 °C begins to crystallize Eu_2O_3, which is further transformed to vaterite-type $EuBO_3$ when heated at 700 °C for 90 min. Typically, using solid state methods, vaterite-type $EuBO_3$ is reported only at temperatures above 750 °C.[66] DSC measurements in air show an exotherm at 610 °C (Figure 13b), corresponding to the crystallization of $EuBO_3$. This transition at 610 °C is at a lower temperature than the exotherm reported for the crystallization of vaterite-type $EuBO_3$ using solid-state synthetic techniques, which

occurs near 650 °C.[66] Figure 14a shows a TEM image of the as-prepared amorphous Eu-B powder, which is made up of a web-like network of smaller particles. An SEM image (Figure 14b) of the $EuBO_3$ annealed at 700 °C shows that the product roughly retains the network-like morphology of its precursor.

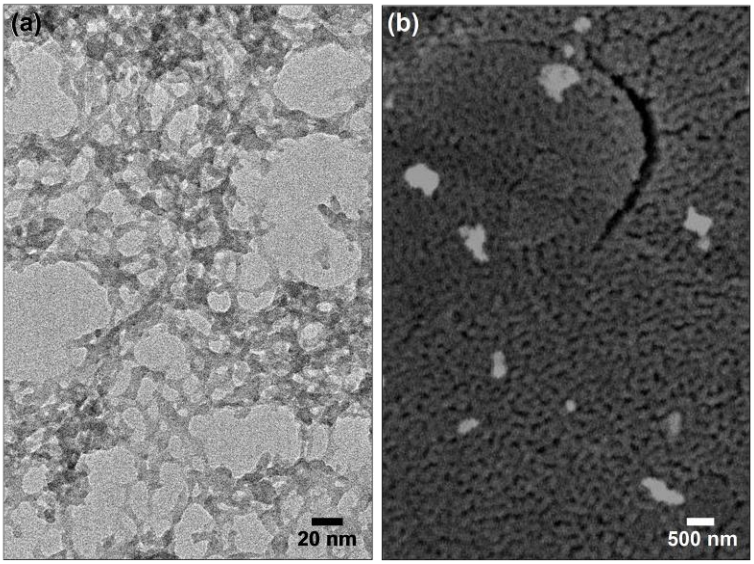

Figure 14. (a) TEM image of as-prepared Eu-B powder. (b) SEM image of porous $EuBO_3$ prepared by annealing the powder from (a) at 700 °C in air for 90 min.

In addition to $EuBO_3$, other rare earth borates can be formed using this method. YBO_3, $GdBO_3$, $HoBO_3$, $SmBO_3$ and $NdBO_3$ can be made by annealing their respective amorphous powder precursors at 700 °C (Figure 15). All are the orthoborate phase, except $NdBO_3$, which preferentially forms a hexagonal phase that does not have nonlinear optical properties. Of interest, the as-prepared powders of Ho-B and Nd-B retain the color of their $Ho(NO_3)_3$ and $Nd(NO_3)_3$ precursors, respectively. This is

credited to 4f transitions in the Ho^{3+} and Nd^{3+} ions.[64] However, the color disappears when the amorphous powders are annealed to form $HoBO_3$ and $NdBO_3$, which are both dense white solids.

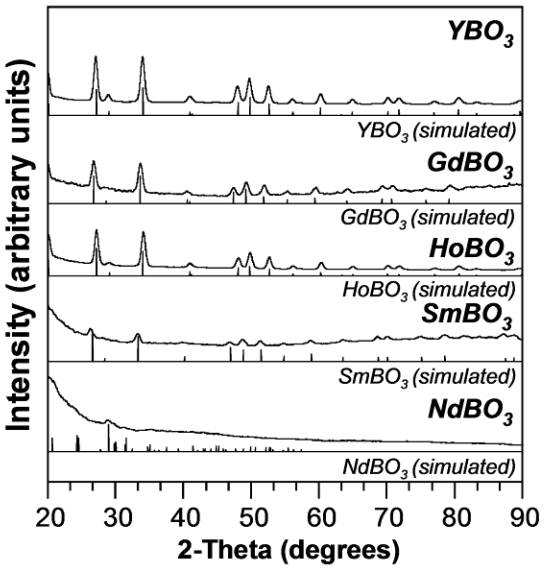

Figure 15. Powder XRD patterns for the range of *RE*BO_3 accessible from amorphous precursor powders annealed at 700 °C in air for 90-120 min. Simulated XRD patterns are below experimental data.

The orthoborate structure of *RE*BO_3 has a noncentrosymmetric structure, which can result in nonlinear optical properties.[52] Of particular technological interest are orthoborates doped with rare earth cations because they can be used as phosphors. When irradiated with UV light, YBO_3:Eu emits in the red-orange region of the visible spectrum.[22,54,59,62] A promising red phosphor for use in plasma display panels, YBO_3:Eu has a strong luminescent intensity, a high optical damage threshold, vacuum-UV transparency, and chemical stability.[59] The quality of emission from YBO_3:Eu is related

to its crystallinity and the symmetry around the Eu^{3+} cations.[22,54] The strongest UV emission bands in the visible range observed for YBO_3:Eu are at 592, 612 and 624 nm. The orange emission at 592 nm corresponds to a magnetic dipole transition, whereas the red emission at 612 nm corresponds to an electric dipole transition.[22] Local crystal field symmetry around the Eu^{3+} cations can have a significant effect on electric dipole transitions.[22] For example, bulk-scale single crystals have high local symmetry around the Eu^{3+} cations, which diminishes the intensity of the red emission. However, when the crystal size is decreased to the nano regime, surface defects decrease the local symmetry around the Eu^{3+} cations, increasing the intensity of the red emission.[22,59] For use in plasma displays, it is important that the YBO_3:Eu have a strong red emission component.[54]

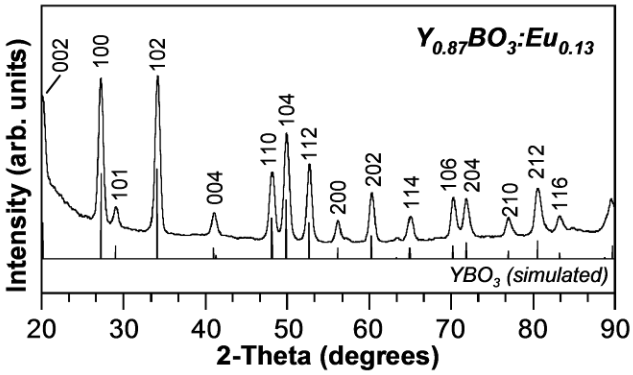

Figure 16. Powder XRD pattern for Eu-doped YBO_3 after annealing at 700 °C for 2 h in air (with simulated YBO_3 pattern, PDF card no. 16-277).

Using our synthetic protocol, we were able to synthesize YBO_3 doped with Eu^{3+} by annealing the as-prepared powder at 700 °C in air for 2 h (Figure 16). Doping with

Eu^{3+} is evidenced by the lattice expansion seen in powder XRD.[67] Our method results in the precipitation of networks of small particles (~ 10-20 nm in diameter), as seen in Figure 17a. The homogeneous incorporation of Y and Eu is confirmed by EDS mapping, showing an 87:13 Y:Eu ratio (Figure 17 b-d). When annealed, the resulting powder retains the periodic voids of the nanoparticle networks and is composed of constituent particles that are ~ 500 nm in diameter (Figure 18). A UV-emission spectrum (Figure 19) obtained by irradiating YBO_3:Eu particles dispersed in isopropanol with 254-nm light shows emission bands at 593, 612 and 627 nm, which correlate well with literature.[59] The dominant red emission at 612 nm is in accordance with recent reports of emission spectra for 8 nm YBO_3:Eu nanocrystals prepared by solvothermal methods.[59]

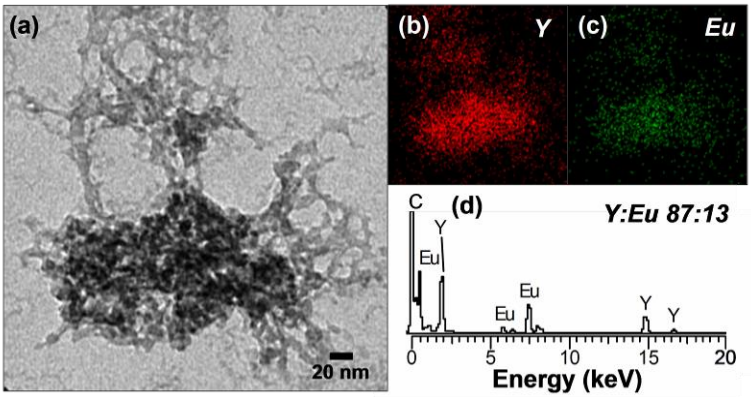

Figure 17. (a) TEM image of as-prepared Y-Eu-B powder with EDS maps showing the presence of both (b) Y and (c) Eu; (d) Y:Eu ratio was shown to be 87:13 via EDS.

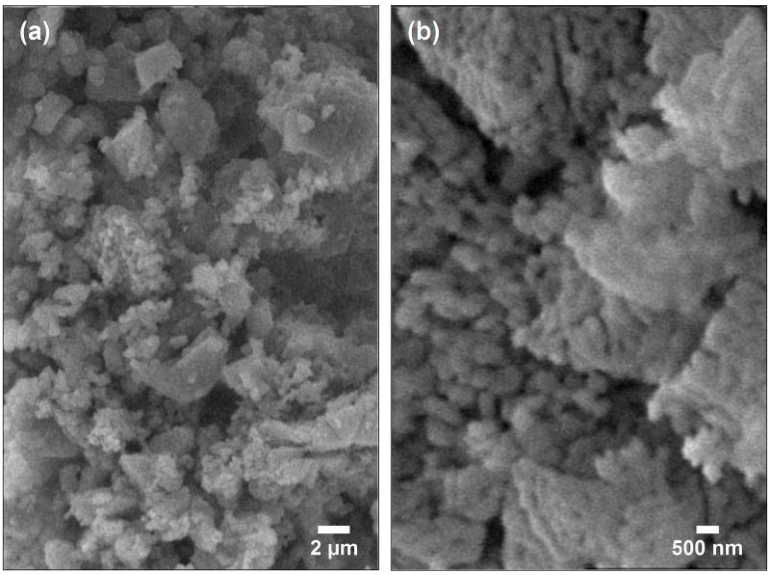

Figure 18. SEM images of YBO_3:Eu taken at (a) 2.8k and (b) 9k magnification.

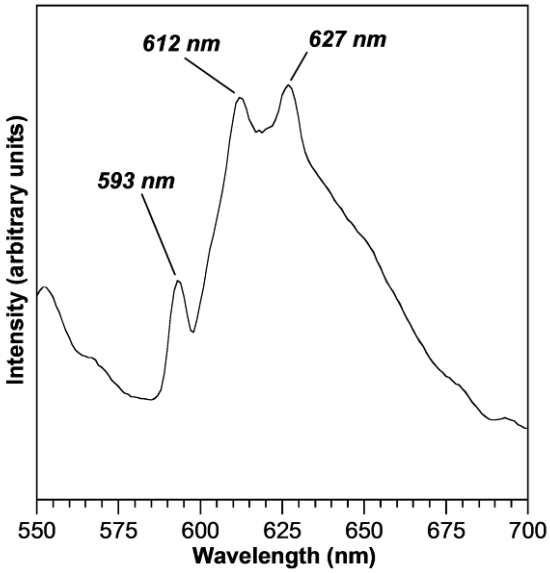

Figure 19. Emission spectrum for YBO_3:Eu (dispersed in isopropanol) collected under 254-nm UV irradiation. Peaks at 593 and 612 nm correlate to orange and red emissions, respectively.

Furthermore, evidence suggests that this strategy for making rare earth borates can be expanded to include multi-metal borates. For example, when $Al(NO_3)_3$ was added to the reaction which precipitates the Gd-B powder, a multi-metal precursor is formed. When annealed at 800 °C in air for 2 h, huntite-type $Al_3Gd(BO_3)_4$ forms along with $Gd_3Al_5O_{12}$ (Figure 20a). Huntite-type borates can have frequency self-doubling properties and laser applications.[52,23] Similarly, $Al_3Sm(BO_3)_4$ can be made with a $SmBO_3$ impurity (Figure 20b). Although impurities are present, these powder XRD data suggest that additional metals can be added to *RE*-B powders to form precursors to multi-metal borates.

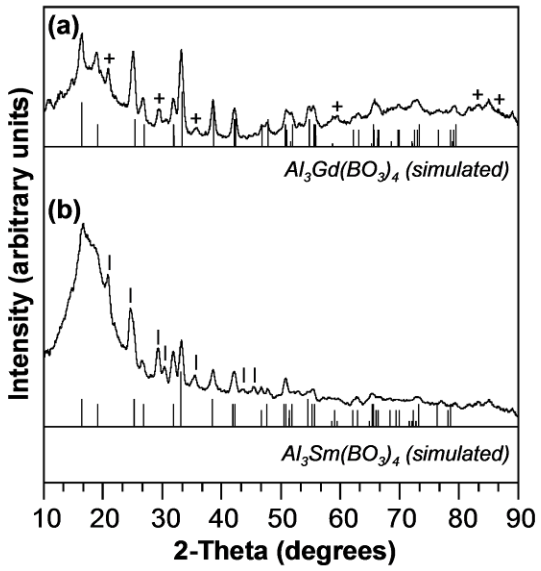

Figure 20. Powder XRD patterns for (a) $Al_3Gd(BO_3)_4$ and (b) $Al_3Sm(BO_3)_4$ made by annealing a *RE*-Al-B powder at 800 °C in air for 2 h. $Gd_3Al_5O_{12}$ and $SmBO_3$ impurities are represented by | and +, respectively.

Conclusions

In this chapter, a simple aqueous strategy was developed for synthesizing amorphous rare earth borate precursor powders. The amorphous precursors can be annealed to form *RE*BO_3 powders, which retain the network-like structure of their precursors. It is hypothesized that the amorphous precursor is made up of a polymeric network of RE^{3+} and BH_4^- and other borohydride species. Due to their nonlinear optical properties, rare earth orthoborates can be used as red phosphors in plasma displays. Of particular importance is the formation of YBO_3:Eu using this strategy, which has a red-orange emission comparable to literature reports.[59] Furthermore, other metals can be introduced into the amorphous *RE*-B powder, resulting in a multi-metal precursor that can be used to form huntite-type $Al_3RE(BO_3)_4$. The simplicity of this strategy for synthesizing *RE*BO_3 could make it useful for forming thin films and patterned substrates.

CHAPTER IV

CONVERTING METALS INTO PHOSPHIDES: A GENERAL STRATEGY FOR THE SYNTHESIS OF METAL PHOSPHIDE NANOCRYSTALS*

Introduction

Nanocrystalline transition metal phosphides are attractive candidates for advanced catalytic, electronic, and magnetic applications.[69] Furthermore, recent studies of their size-dependent physical properties have uncovered notable differences between bulk and nanoscale materials.[69-71] Thus, it is important to develop general synthetic approaches that yield nanocrystalline transition metal phosphides with careful control over both the composition and the morphology. A variety of methods have emerged for the synthesis of these materials, including solvothermal reactions,[72] decomposition of single-source precursors,[73] high temperature annealing of organometallic and solid-state precursors,[74] and the co-reaction of organometallic reagents with phosphines.[70-71,75-79] In particular, Brock,[70-71,75] Hyeon,[78-79] and Yang and Liu[80] have shown that high-quality 3d transition metal phosphide nanocrystals and nanowires can be obtained by thermal decomposition of metal-phosphine complexes that form in-situ from the reaction of metal salts and trioctylphosphine (TOP), a common stabilizing agent.

Here we describe a new strategy for synthesizing nanostructures of transition metal phosphides. Unlike the previous methods that involve either direct combination of precursors or thermal decomposition of single-source precursors, our approach involves a different mechanism: the conversion of pre-formed metal nanoparticles into metal phosphides by solution-mediated reaction with TOP. By starting with metal nanoparticles as precursors, a large number of metal phosphide systems are accessible, including those with 4d and 5d transition metals that have not previously been reported as unsupported nanocrystals. In some cases, the size and dispersity of the metal nanocrystal precursors is retained in the phosphide product, which provides a proof-of-concept for a method to design metal phosphide nanocrystals with precise sizes. Furthermore, nanostructures such as hollow spheres and rods, which are not typically accessible using thermal decomposition reactions, can be easily made using a Kirkendall-type mechanism, which utilizes metal nanoparticles as reactive templates.

Experimental Section

Chemicals

Palladium(II) 2,4-pentanedionate ($Pd(acac)_2$), copper(II) 2,4-pentanedionate (98 %, $Cu(acac)_2$), nickel(II) 2,4-pentanedionate (95 %, $Ni(acac)_2$), rhodium(III) chloride hydrate ($RhCl_3 \cdot xH_2O$), platinum(II) 2,4-pentanedionate ($Pt(acac)_2$), cobalt(II) 2,4-pentanedionate ($Co(acac)_2$), silver nitrate (99 %, $AgNO_3$), hydrogen tetrachloroaurate(III) trihydrate (99 %, $HAuCl_4 \cdot 3H_2O$), and iron(III) 2,4-pentanedionate

($Fe(acac)_3$) were used as purchased from Alfa Aesar. Trioctylphosphine (tech. 90%, TOP), trioctylphosphine oxide (98 %, TOPO), triphenylphosphine (99 %, TPP), tetra-n-octylammonium bromide (98 %, TOAB), sodium borohydride (98 %, $NaBH_4$), oleic acid, hexadecylamine (90 %, HDA) and toluene were from Alfa Aesar. Octyl ether (99 %), oleylamine (70 %), hexanes and 1,2-hexadecanediol (90 %) were from Sigma Aldrich. All reactions were carried out under argon using standard air-free techniques.

Characterization

Powder x-ray diffraction (XRD) was performed on a Bruker-AXS GADDS diffractometer using microdiffraction techniques as previously described.[38] Transmission electron microscopy (TEM) was performed using a JEOL JEM-2010 transmission electron microscope operating at 200 kV. TEM samples were prepared by sonicating a few milligrams of nanoparticles in either hexanes or ethanol (depending on solubility) and then drop casting onto Ni or Cu grids, which were allowed to slowly dry under ambient conditions (or in an argon atmosphere for more easily oxidized samples, such as Cu).

Direct Synthesis of Metal Phosphide Nanocrystals

Synthesis of PdP_2 nanocrystals. The synthesis of PdP_2 nanocrystals was adapted from Hyeon's work.[78-79] $Pd(acac)_2$ (20.5 mg) was dissolved in 2.0 mL TOP with sonication (orange-colored when dissolved) in an argon atmosphere. The Pd-TOP solution was rapidly injected into 2.2 g TOPO at 360 °C and heated at 360 °C for 2 h.

Aliquots were taken at 30 s, 5 min, and 30 min and quenched in ethanol. After 2 h, the reaction was cooled and saturated with ethanol. The particles were isolated by centrifugation, washed with ethanol, and dried under Ar.

Synthesis of Ni_2P nanocrystals. The synthesis of Ni_2P nanocrystals was also adapted from Hyeon's work.[78-79] Typically, 0.05-0.2 mmol $Ni(acac)_2$ dispersed in 0.5-2.0 mL TOP and rapidly injected into 2 mL of octyl ether at 290 °C. After injection, the reaction was aged 2 h at 300 °C, then cooled to room temperature. Ethanol was added to precipitate particles, which were isolated via centrifugation, washed with ethanol and hexanes, and dried under a stream of Ar. Alternatively, 2 g TOPO or HDA was used in place of octyl ether. When HDA was used, a 3:1 mix of ethanol:hexanes was added to precipitate particles.

Synthesis of Metal Nanocrystal Precursors

Pd Nanocrystals. Pd nanocrystals were synthesized using a modification of Hyeon's procedures.[81] 23.2 mg $Pd(acac)_2$ were heated in 2.0 mL TOP at 220 °C for 30 min, precipitated with ethanol, isolated by centrifugation, washed with ethanol, and dried under argon.

Cu Nanocrystals. This synthesis of copper nanocrystals is a modification of methods reported by Hyeon and co-workers for the synthesis of Ni nanocrystals.[82] A solution was prepared under Ar using 26.2 mg of $Cu(acac)_2$ in 1.000 mL of oleylamine,

which was heated in a 100 °C water bath and then rapidly injected into 2.000 mL of oleylamine at 260 °C. The reaction was heated at 260 °C for 30 min and then slowly cooled. Cu particles could be isolated by saturating the solution with ethanol, followed by centrifugation and washing with ethanol and hexanes. For conversion to Cu_3P, the Cu was used as prepared in oleylamine to avoid oxidation.

Ni Nanocrystals. Two methods were used to prepare Ni nanoparticles of varying size and dispersity. The first method is modified from Sra et al.[83] and involves sonicating 85.3 mg $Ni(acac)_2$, 166.5 mg 1,2-hexadecanediol, 200 μL oleylamine, and 200 μL oleic acid in 4.0 mL octyl ether. The solution was then heated at 230 °C for 1 h, then cooled and saturated with ethanol. The particles were isolated by centrifugation, washed with ethanol, and dried under Ar. The second method is a modification of Hyeon's method[12] in which 210.0 mg $Ni(acac)_2$ and 2.80 mL oleylamine were heated to 100 °C and injected into 2.5 g TPP at 215 °C. The solution was heated at 200 °C for 30 min, then cooled. The particles were precipitated with ethanol, isolated via centrifugation, washed with ethanol and dried under argon.

Rh Nanocrystals. Rh nanoparticles were prepared by modifying Hyeon's method.[82] 28.4 mg $RhCl_3 \cdot xH_2O$ were sonicated in 1.000 mL oleylamine and injecting the solution into 2.0 g HDA at 260 °C. The solution was then heated 1 h at 260 °C, then cooled and saturated with 3:1 ethanol:hexanes. The particles were isolated by centrifugation, washed with 3:1 ethanol:hexanes, and dried under Ar.

Pt Nanocrystals. Pt nanocrystals were prepared by modifying Sra's method for FePt[83] using 47.8 mg $Pt(acac)_2$, 42.9 mg 1,2-hexadecanediol, 100 μL oleylamine and 100 μL oleic acid in 2.0 mL octyl ether. The solution was then heated at 230 °C for 1 h. The solution was cooled and saturated with ethanol. The particles were isolated by centrifugation, washed with ethanol and dried under Ar.

Ag Nanocrystals. This synthesis is a modification of methods previously used by Sra et al. to prepare FePt nanocrystals.[83] A solution of 70.2 g of $AgNO_3$, 70.9 mg of 1,2-hexadecanediol, 100 μL of oleylamine, 100 μL of oleic acid, and 2.00 mL of octyl ether was heated at 100 °C for 1 h and then slowly cooled and saturated with ethanol, which caused an orange-brown precipitate to form. The precipitate was washed with hexanes several times. The hexane wash was reserved, to which an equal volume of ethanol was added. Ag nanocrystals were isolated by centrifugation from the hexane/ethanol solution, washed with ethanol, and dried under Ar.

Au Nanocrystals. Au nanocrystals were prepared according to Grebinski's methods.[84] 13.1 mg $HAuCl_4 \cdot 3H_2O$ were dissolved in 0.625 mL NANOpure water. Separately, 21.0 mg TOAB was stirred in 0.825 mL toluene under argon. The aqueous Au^{3+} solution was added to the toluene solution. Then, 0.01 mL TOP dissolved in 0.200 mL toluene was added dropwise until the solution changed from clear dark red to milky white. 6.1 mg $NaBH_4$ in 0.500 mL NANOpure water was added dropwise. The reaction

was stirred 30 min, then the toluene layer extracted and saturated with ethanol. The particles were isolated via centrifugation, washed with ethanol, and dried under argon.

Fe Nanocrystals. Synthesis of Fe nanocrystals is also a modification of a previous literature report.[82] A solution was prepared under Ar using 35.3 mg of $Fe(acac)_3$ in 1.0 mL of oleylamine, which was heated in a 100 °C water bath and then rapidly injected into 1.0 mL of oleylamine at 260 °C. The reaction was heated 1 h at 260 °C and then cooled to room temperature. This solution could be saturated with ethanol and centrifuged to isolate nanoparticles, although oxidation readily occurs.

Synthesis of Metal Nanocrystals and in situ Conversion to Metal Phosphides

Pd Nanocrystals and in Situ Conversion to Pd_5P_2. 19.5 mg $Pd(acac)_2$ was dissolved in 2.0 mL TOP with stirring in an argon atmosphere. The reaction solution was heated slowly to 300 °C and held at this temperature for 30 min (Pd nanorcrystals initially formed at 220 °C before conversion to Pd_5P_2). The solution was cooled and saturated with ethanol. The particles were isolated by centrifugation, washed with ethanol, and dried under Ar.

Co Nanocrystals and in Situ Conversion to CoP. Synthesis of cobalt nanocrystals is also a modification of Hyeon's methods.[82] A solution was prepared under Ar using 30.9 mg of $Co(acac)_2$ in 1.0 mL of olyelamine, which was heated in a 100 °C water bath and then rapidly injected into 2.0 g of HDA at 320 °C. The reaction

was heated 1 h at 320 °C; then the temperature was raised to 330 °C. At 330 °C, 1.0 mL of TOP was rapidly injected and the temperature was then raised to 370 °C. The reaction was held at 370 °C for 1 h and then slowly cooled and saturated with ethanol and hexanes. CoP particles were isolated by centrifugation, washed thoroughly with ethanol and hexanes, and dried under Ar. The Co nanocrystal intermediate could be isolated by saturating the solution with ethanol and hexanes prior to injection of TOP and centrifuging, although oxidation readily occurs.

Conversion of Metal Nanocrystals into Metal Phosphides

PdP_2 Nanocrystals. Pd nanocrystals (10-20 mg) were dispersed in 1-2 mL TOP and injected into 2.0 g TOPO at 360 °C. The reaction was heated for 1-2 h, then cooled and saturated with ethanol. The particles were isolated by centrifugation, washed with ethanol, and dried under Ar.

Cu_3P Nanocrystals. A portion of the Cu nanocrystal solution in oleylamine (1.0 mL), prepared as described above, was mixed with 1.0 mL of TOP under Ar and then rapidly injected into 2.0 g of TOPO at 320 °C. The reaction was heated at 320 °C for 1 h and then slowly cooled and saturated with ethanol. Cu_3P nanocrystals were isolated by centrifugation, washed with ethanol, and dried under Ar.

Ni_2P Nanocrystals. Ni nanocrystals (22.2 mg) were dispersed in 1 mL TOP and injected into 2.0 mL octyl ether at 290 °C. The reaction was heated for 2 h at 300 °C,

then cooled and saturated with ethanol. The particles were isolated by centrifugation, washed with ethanol, and dried under Ar.

Rh_2P Nanocrystals. Rh nanocrystals (8.7 mg) were dispersed in 2 mL TOP and injected into 2.0 g TOPO at 360 °C. The reaction was heated for 1 h at 360 °C, then cooled and saturated with ethanol. The particles were isolated by centrifugation, washed with ethanol, and dried under Ar.

PtP_2 Nanocrystals. Pt nanocrystals (18.0 mg) were dispersed in 1 mL TOP and injected into 2.0 mL TOP at 370 °C. The reaction was heated for 2 h at 370 °C, then cooled and saturated with ethanol. The particles were isolated by centrifugation, washed with ethanol, and dried under Ar.

AgP_2 Nanocrystals. TOP (1.0 mL) was added to 9.5 mg of Ag nanocrystals, and mixed by sonication, and then rapidly injected into 2.0 mL of TOP at 370 °C. The reaction was heated at 370 °C for 2 h and then slowly cooled and saturated with ethanol. A mixture of Ag and AgP_2 nanocrystals was isolated by centrifugation, washed with ethanol, and dried under Ar.

Au_2P_3 Nanocrystals. Au nanoparticles (3.1 mg) were dispersed in 2.0 mL TOP and rapidly injected into 2.0 g TOPO at 360 °C. The reaction was heated at 360 °C for 6

hours, then cooled and saturated with ethanol. The particles were isolated by centrifugation, washed with ethanol, and dried under Ar.

FeP Nanocrystals. TOP (1.0 mL) was added to 1.0 mL of the Fe-oleylamine solution prepared as described above under Ar. This solution was stirred and then transferred either rapidly or via syringe pump into 2.0 g of HDA at 320 °C. During or immediately after injection, the reaction temperature was rapidly increased to 330-350 °C. The reaction was heated at 330-350 °C for 1-2 h and then slowly cooled and saturated with ethanol and hexanes. FeP particles were isolated by centrifugation, washed thoroughly with ethanol and hexanes, and dried under Ar.

Results and Discussion

In a typical reaction, a metal acac dissolved in TOP is injected into a hot solvent (TOP, trioctylphosphine oxide, or octyl ether) at 300-360 °C. By collecting aliquots over time, we discovered that unlike the previously reported pathways that involve the direct thermal decomposition of complexes formed between the metal acac and TOP, the formation of metal phosphide nanoparticles instead goes through a metal nanoparticle intermediate. As an example, at early stages of the reaction between $Pd(acac)_2$ and TOP to form PdP_2, a Pd nanoparticle intermediate can be isolated. This is confirmed by XRD (Figure 21a, top), TEM and SAED (Figure 21b). EDS shows a Pd:P ratio of 50:50, as expected for small (~ 2 nm), TOP-stabilized Pd nanoparticles (which increases the

amount of phosphorus detected). As the reaction progresses, mixed-phase Pd_5P_2/PdP_2 begin to form after 5 minutes (Figure 21a, middle), which converts to phase-pure PdP_2 after 2 h (Figure 20a, bottom and 21c) where EDS shows a Pd:P ratio of 35:65.

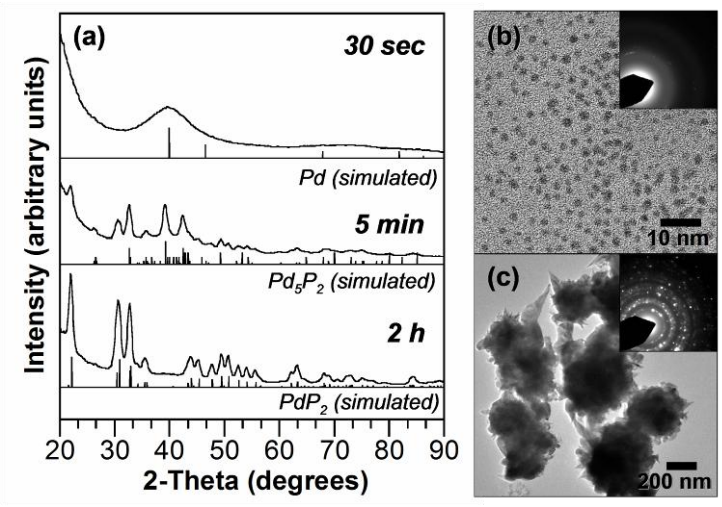

Figure 21. Formation of PdP_2 from $Pd(acac)_2$ and TOP. (a) Powder XRD patterns of PdP_2 formation showing a Pd intermediate after 30 s, followed by the formation of mixed-phase PdP_2/Pd_5P_2 within 5 min, and phase-pure PdP_2 after 2 h; TEM images showing (b) Pd intermediate at 30 s and (c) PdP_2 aggregates formed after 2 h.

Building on the important observation of a metal nanoparticle intermediate, Pd nanoparticles can be made separately according to literature methods,[81] then isolated, washed, and re-dispersed in TOP, then injected into hot TOPO to form PdP_2 nanoparticles via a conversion mechanism. Four distinct morphologies of PdP_2 nanostructures can be reproducibly accessed by controlling subtle, and sometimes unexpected, reaction conditions involved in the Pd to PdP_2 conversion reaction. The nanostructures shown in Figures 22f-i were all generated using 2 mL TOP and 2 g

TOPO at 360 °C. Discrete nanocrystal and nanorod structures (Figure 22b) are generated when a glass stirbar is used in the reaction, regardless of the Pd concentration. In contrast, spherical aggregates (Figure 22c-f) are generated when a Teflon stirbar is used. We speculate that high temperatures begin to melt the Teflon, and its presence as a liquid in the reaction solution could cause it to act as an additional stabilizing agent, influencing the shape of the nanocrystals and promoting aggregation. (Distortion of Teflon stirbars after reactions greater than 30 min at 360 °C support this hypothesis.)

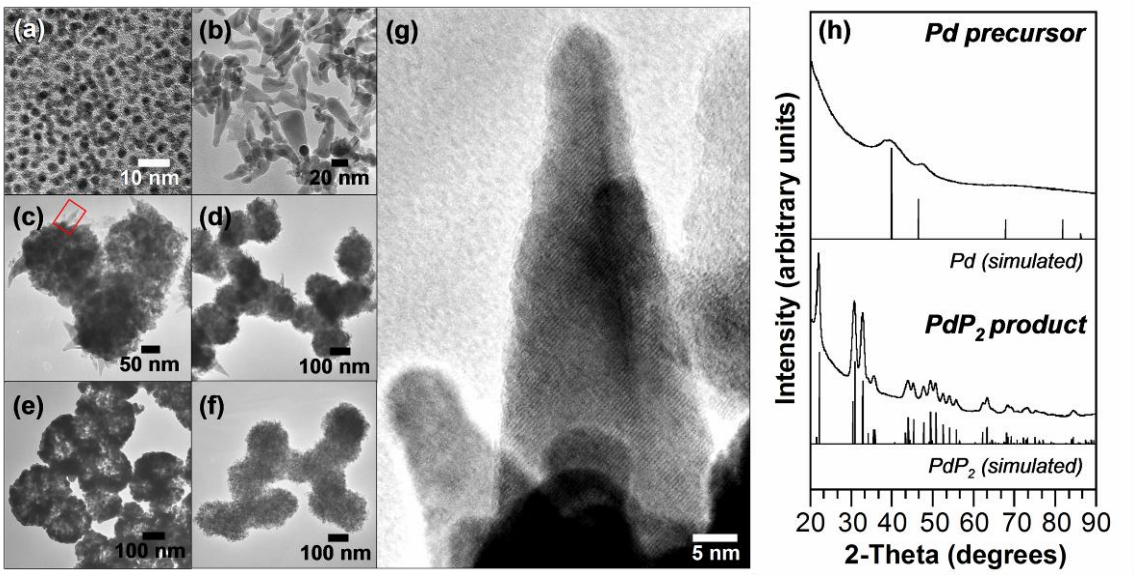

Figure 22. Formation of PdP_2 from Pd nanocrystals. TEM images of (a) Pd nanocrystals and (b-g) PdP_2 formed from (a) by reaction with TOP at 360 °C: using (b) a glass stirbar with 20 mg Pd and 2 mL TOP aged 2 h, (c) a Teflon stirbar with 20 mg Pd and 2 mL TOP aged 1 h, (d) Teflon stirbar with 10 mg Pd and 1 mL TOP aged 1 h, (e) particles from (c) aged 2 h, (f) Teflon stirbar with 10 mg Pd and 2 mL TOP aged 2 h, and (g) enlarged area contained by the red box in (c) showing single crystalline cone-like protrusions; (h) powder XRD patterns of Pd precursors in (a) and PdP_2 from (b).

Using relatively large amounts of Pd relative to TOP (e.g. 20 mg Pd, 2 mL TOP), dense spherical aggregates form within 1 h of heating to 360 °C (Figure 22c). These structures adopt nano-tumbleweed morphologies that are assembled from discrete nanocrystals and nanorods and contain single-crystal cone-shaped PdP_2 protrusions (Figure 22c,g) that are similar in morphology to those shown in Figure 22b. Similar structures form using 10 mg Pd and 1 mL TOP (Figure 22d). When the dense spherical aggregates in Figure 22c are heated for an additional hour at 360 °C, they begin to transform into hollow aggregates that are no longer densely packed nor composed of cone-like particles (Figure 22e). When the Pd:TOP ratio is decreased, dense spherical aggregates are formed that consist of much smaller spherical nanocrystals (Figure 22f). Taken together, this suggests that the Pd:TOP ratio is an important variable for controlling the nanostructure morphology, particularly for controlling the size and morphology of the constituent nanocrystals.

Because Pd is a noble metal (and generally presumed nonreactive) and TOP is typically considered an innocent coordinating ligand in nanocrystal synthesis, the facile conversion of palladium nanocrystals into PdP_2 when reacted with hot TOP is surprising and serves as a proof-of-concept for developing a generalized strategy for converting metal nanocrystals into metal phosphides. It has been proposed that colloidal metals can induce cleavage of the P-C bond in alklyphosphines[85] and this is suspected to be the driving force behind the conversion of Pd nanocrystals into PdP_2. Figure 23 presents a hypothetical reaction pathway by which metal nanocrystals are converted into metal phosphides. Indeed, the conversion strategy can be extended to other metal phosphide

systems, and is general for many 3d, 4d and 5d transition metals. Table 3 lists the various metal phosphides accessible via this strategy and the reaction conditions required for each. It was found that Ir, Sn, and Ru nanoparticles did not form phosphides under the conditions used for the other systems, perhaps due to reactivity (Ir) or oxidation (Sn, Ru). The Pd-P system is particularly noteworthy, since it demonstrates that multiple phases can be accessed in the same system (Pd_5P_2 and PdP_2) simply by changing the reaction temperature, and thus the amount of phosphorus incorporation. In addition, the formation of PdP_2, as well as PtP_2, AgP_2 and Au_2P_3, is particularly interesting, since these phases belong to a class of compounds called "polyphosphides," which are phosphorus-rich phases that have short P-P bonds. Polyphosphides can be difficult to synthesize as bulk-scale solids,[86] and they also have not been observed as products of low-temperature solution reactions. Thus, this nanocrystal conversion strategy provides a unified method for synthesizing a variety of 3d, 4d, and 5d transition metal phosphide nanocrystals, many of which have not been previously accessed by direct reaction of organometallic precursors with TOP.

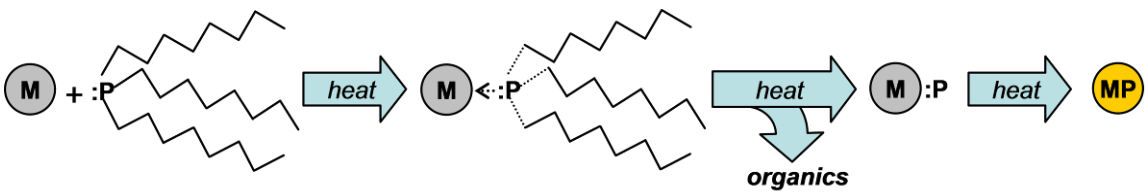

Figure 23. Hypothetical reaction pathway for converting metal nanocrystals (M) into metal phosphides (MP) using TOP as a phosphorus source.

Table 3. Transition-metal phosphides accessible by reacting metal nanocrystal precursors with TOP.

Nanocrystal precursor	Reaction conditions[a]	Product (via powder XRD)
Fe	330-350 °C HDA/TOP, 1-2 h	FeP
Co	350 °C HDA/TOP, 2 h	CoP
Ni	300 °C TOP/Oct_2O, 2 h	Ni_2P
Cu	320 °C TOP/TOPO, 1 h	Cu_3P
Rh	360 °C TOP/TOPO, 1-2 h	Rh_2P
Ag	370 °C TOP, 2 h	AgP_2, Ag
Pd	300 °C TOP, 0.5 h	Pd_5P_2
	360 °C TOP/TOPO, 1-2 h	PdP_2
Pt	370 °C TOP/TOPO, 2 h	PtP_2
Au	360 °C TOP/TOPO, 6 h	Au_2P_3, Au

[a] HDA = *n*-hexadecylamine, TOP = tri-*n*-octylphosphine, TOPO = tri-*n*-octylphosphine oxide, Oct_2O = octyl ether.

It is worth highlighting that we (and others) generally observe that only one or two phases form preferentially in a particular binary system that contains multiple line phases. For metal phosphides, the phases that form as nanocrystals tend to be those that are stable to the highest temperatures (regardless of whether they are metal-rich or phosphorus-rich), but this is not always the case. Thus, it is difficult to predict in which systems multiple phases will be accessible. In systems where multiple metal phosphide phases can be formed, higher temperatures tend to favor the phosphorus rich phases because of either higher phosphorus availability via TOP decomposition or faster phosphorus diffusion into the metal nanoparticles. Exploiting other solution-chemistry

conversion strategies could possibly expand the number of accessible phases in a given binary system.[8]

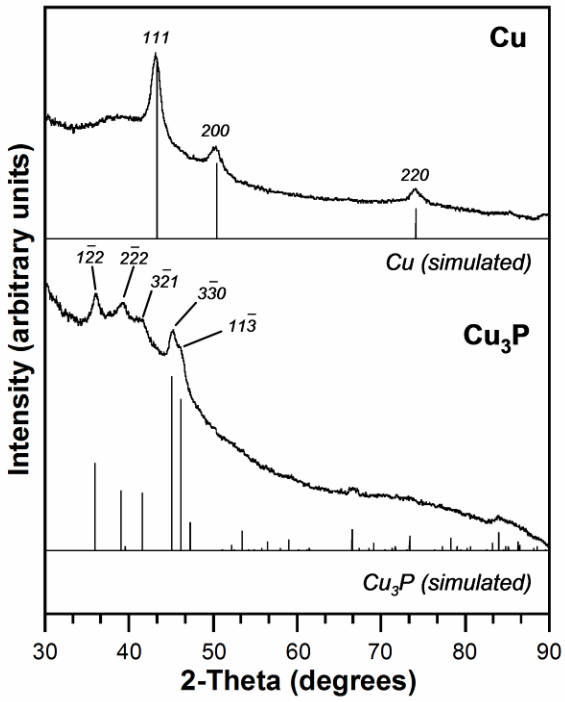

Figure 24. Powder XRD patterns of Cu nanocrystals and Cu_3P formed from their reaction with TOP at 320 °C. Major reflections are indexed and simulated patterns are shown below the experimental data.

A key aspect of our phosphide conversion strategy is that in many cases the size of the metal nanocrystal precursor can be retained by the metal phosphide product. For example, Figure 24 shows X-ray diffraction evidence that Cu_3P nanocrystals can be generated by reacting Cu nanoparticles with TOP in TOPO at 320 °C. While there are several reports describing the synthesis of nanocrystalline or bulk-scale Cu_3P using solvothermal strategies,[72,87-88] no examples describe high-quality single-domain Cu_3P

nanocrystals with minimal polydispersity. In our case, the Cu nanoparticles are generally spherical with an average size of 13.1 ± 2.6 nm (Figures 25a and 26a). The SAED pattern confirms the fcc structure of Cu metal (Figure 25a). After reaction with TOP to form Cu_3P, the nanoparticles grow to 15.6 ± 2.6 nm (consistent with diffusion of P into Cu) while retaining the general morphology and size dispersity of the Cu nanoparticle precursors (Figures 25b and 26b). The SAED pattern (Figure 25b) confirms that the nanoparticles are Cu_3P, and EDS analysis shows a Cu:P ratio of 55:45 (Figure 25b). This is consistent with the ratio expected from formation of Cu_3P stabilized by TOP, which increases the amount of phosphorus detected by EDS. The Cu_3P nanoparticles are generally single-domain crystals (Figure 25c), and their morphology tends to feature hexagonal facets that are derived from the hexagonal crystal structure of Cu_3P (Figure 25d).

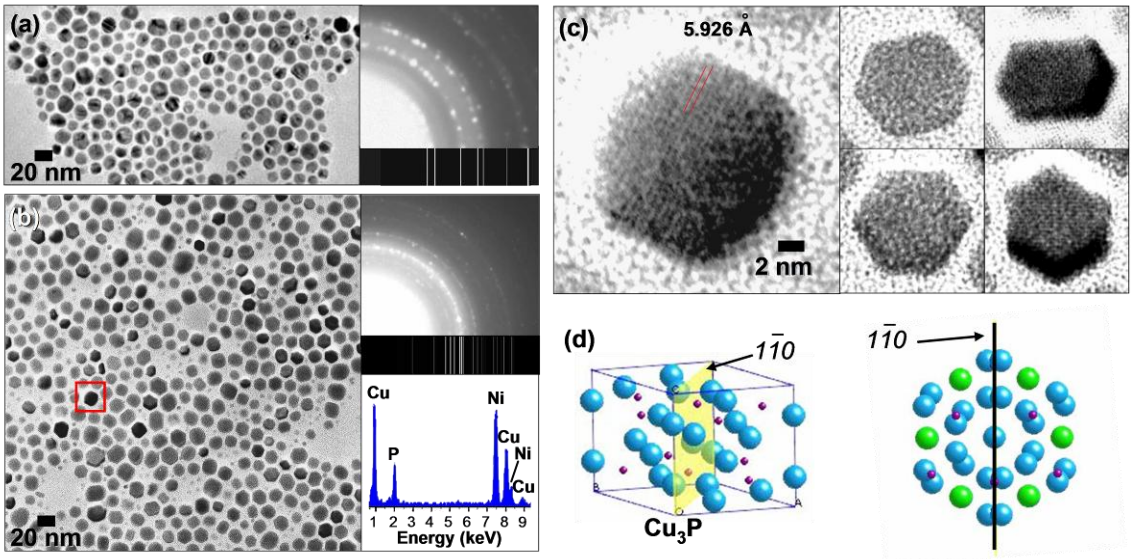

Figure 25. Cu_3P nanocrystals formed by reacting Cu nanoparticles with hot TOP: (a) TEM image and selected area electron diffraction (SAED) for Cu precursor nanoparticles with simulated SAED inset; (b) TEM image and SAED for Cu3P nanocrystals formed from (a) with simulated SAED and energy dispersive x-ray spectrum for Cu_3P nanocrystals (Ni grid) inset; (c) TEM images of Cu_3P nanocrystals depicting the hexagonal morphology and an enlarged image showing d-spacing corresponding to the 1-10 plane. The area enlarged is denoted by red box in (b); (d) Unit cell of Cu_3P with 1-10 plane highlighted, and top view of several unit cells showing how the Cu_3P crystal structure is related to the observed hexagonal morphology of the nanocrystals (corner atoms of hexagon motif are highlighted green).

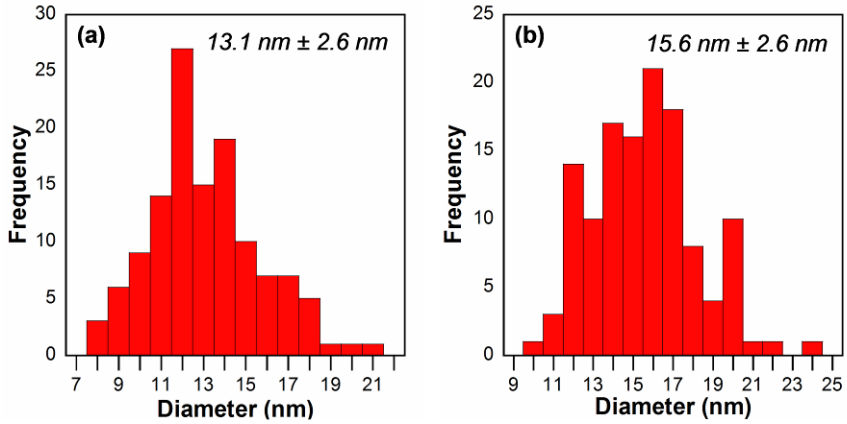

Figure 26. Histograms of nanocrystal diameters for (a) Cu and (b) Cu_3P formed from (a).

In addition to Cu_3P, nanocrystals of Ni_2P, Rh_2P and PtP_2 generated by reacting small spherical nanocrystals of their respective metals with TOP show retention of the size and dispersity of their precursors. Figure 27 shows TEM images and powder XRD patterns of small spherical Ni_2P, Rh_2P and PtP_2 and the metal nanocrystals used as precursors. In the case of Ni_2P, the Ni nanoparticles used as precursors (Figure 27a) are 5.2 ± 0.8 nm, and the Ni_2P nanoparticle products (Figure 27b) are 5.6 ± 0.8 nm (histograms in Figure 28). The small but reproducible increase in average nanocrystal size is roughly consistent with the volume expansion expected for the conversion of fcc Ni to Fe_2P-type Ni_2P via addition of phosphorus. Similar size retention is observed for Rh_2P and PtP_2 nanocrystals (Figure 27 c-f). The retention of relative size and dispersity during the conversion of metals into phosphides could provide a means for designing metal phosphide nanocrystals of precise sizes needed for catalytic or electronic applications.

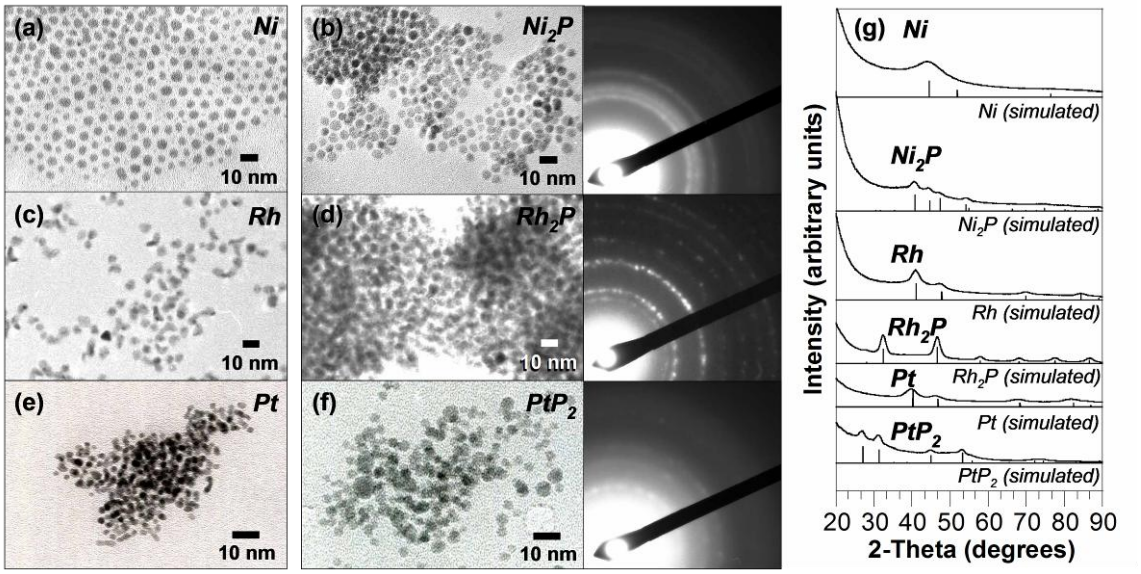

Figure 27. Metal phoshpide nanocrystals with retention of precursor size. TEM images of (a) Ni nanocrystals, (b) Ni_2P formed from (a), (c) Rh nanocrystals, (d) Rh_2P formed from (c), (e) Pt nanocrystals, and (f) PtP_2 formed from (e). SAED patterns for the metal phosphide nanocrystals are shown to the right of the TEM images. (g) Powder XRD patterns of metal and metal phosphide nanocrystals from (a-f) with simulated patterns shown below experimental data.

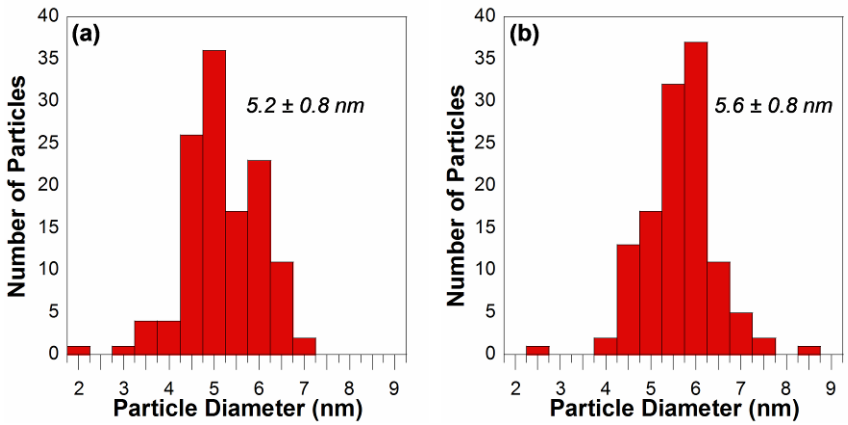

Figure 28. Histograms of nanocrystal diameters for (a) small spherical Ni nanocrystals and (b) Ni_2P formed from (a).

Not all metal phosphide nanocrystals formed from metal nanoparticle precursors retain the size and dispersity of their precursors. As discussed previously, when small Pd nanocrystals are converted to PdP_2, the products can be various derivatives of spherical aggregates formed from smaller particles. Aggregates formed using this conversion strategy could be candidates for applications which require high surface area materials. Figure 29 shows powder XRD patterns and TEM images of large aggregated phosphide products and the metal nanocrystal precursors from which they were formed. In addition to PdP_2, Pd_5P_2 can be formed from a similar reaction of Pd nanocrystals with TOP at 300 °C. The resulting Pd_5P_2 spherical aggregates appear to be composed of smaller spherical particles which are not densely packed (Figure 29a), resembling the PdP_2 nanostructures in Figure 22e. Similarly, CoP formed *in situ* from Co nanocrystals (not shown, see experimental details) is not composed of discrete nanocrystals, but rather aggregates of smaller, sintered particles (Figure 29b). Additionally, AgP_2 and Au_2P_3 (Figure 29d,f) form products significantly larger (~ 500 nm) than their precursors (~ 5-10 nm, Figure 29c,e). Furthermore, AgP_2 (Figure 29d,g) always has significant Ag impurities, indicating that the reaction does not go to completion. Analogously, Au_2P_3 also shows a mixture of metal and metal phosphide (Figure 29f,g). The incomplete reactions may be a consequence of the significantly larger particle sizes, likely due to irreversible coalescence during synthesis, which inhibits complete diffusion of phosphorus into the product.

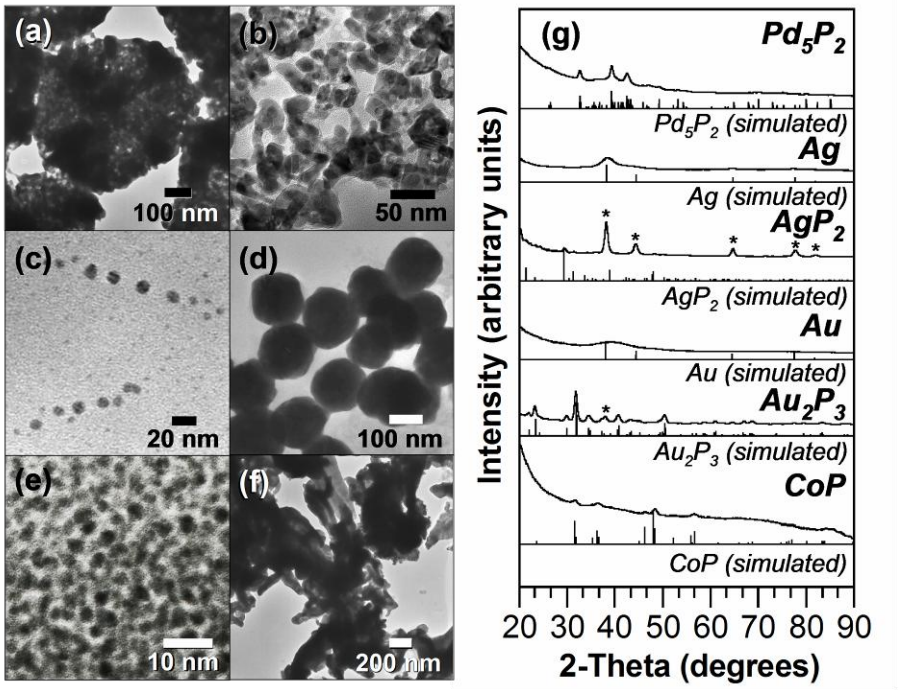

Figure 29. Metal phosphide aggregates formed from metal nanocrystal precursors. TEM images of (a) Pd_5P_2 hollow nanostructures formed from Pd (Figure 21a), (b) CoP formed in situ from Co nanocrystals (not shown), (c) Ag nanocrystals used to form (d) AgP_2, (e) Au nanocrystals used to form (f) Au_2P_3; (g) powder XRD patterns of nanocrystals in (a-f). Metal precursor impurities are indicated by an asterisk (*).

By using metal nanoparticles as precursors, it is also possible to generate metal phosphide nanostructures that cannot easily form using other methods. Alivisatos and co-workers showed that Co nanocrystals react with sulfur to form hollow Co_3S_4 and Co_9S_8 nanospheres via a nanoscale Kirkendall mechanism, which is facilitated by the different diffusion rates of two different chemical species.[12-13] In analogy, when we react 10-25 nm Ni nanocrystals (Figure 30a, inset) with TOP in octyl ether at 300 °C, hollow single-crystal Ni_2P nanospheres form (Figure 30a,b,h). TOP acts as a phosphorus source, which appears to diffuse into the Ni at a slower rate than the Ni

diffuses out, forming hollow voids in the center. For the smaller nanocrystals (10-20 nm), the dominant products are completely hollow nanospheres (Figure 30c). However, for the larger nanospheres, material remains in the center of the hollow spheres (Figure 30b-d), either in the form of dense (Figure 30b,c) or hollow (Figure 30d) nanocrystals. It is difficult to discern at this point whether the encapsulated nanoparticles are Ni or Ni_2P. However, elemental mapping using energy dispersive spectroscopy (EDS) confirms that both Ni and P are present in the shell of the hollow spheres in the expected ratios for particles stabilized by phosphorus-containing molecules (Figure 30e-g). Interestingly, this work hints at a size-dependence to the formation of hollow nanocrystals, since the smaller 5 nm Ni nanocrystals in Figure 27a produced dense Ni_2P nanospheres despite reactions that are carried out under identical conditions. A recent paper by Chiang also describes hollow Ni_2P nanospheres formed by reacting Ni nanoparticles with TOP,[20] although no sphere-in-sphere structures were reported.

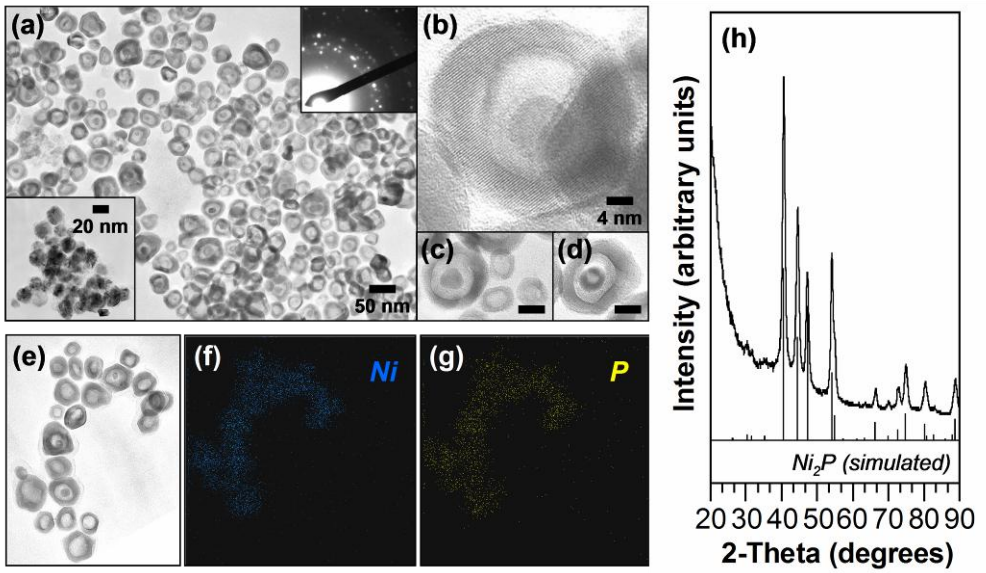

Figure 30. Formation of hollow Ni_2P spheres from 15-25 nm Ni nanoparticles. TEM images and SAED of (a-d) of hollow Ni_2P spheres formed from (a, inset) Ni nanoparticles; (e) TEM image and (f,g) corresponding elemental maps indicating the presence of both (f) Ni and (g) P in the product; (h) powder XRD pattern of hollow Ni_2P spheres. Scale bars are 20 nm for (c) and (d).

In addition to hollow Ni_2P spheres, various morphologies of FeP—including hollow nanorods—can be generated by varying the reaction temperature and injection rate of Fe nanocrystals. Small spherical Fe seed nanocrystals are made by thermally decomposing an $Fe(acac)_3$-oleylamine complex in hot oleylamine (Figure 31a). Isolating and characterizing the Fe nanocrystals results in rapid oxidation to Fe_2O_3, so the Fe seed nanocrystal solution was used as prepared in oleylamine to form FeP. Aliquots of Fe nanocrystals in oleylamine were mixed with TOP and injected into 320 °C HDA, which was rapidly heated to 330 °C or 350 °C during (or immediately after) injection, and aged for 1 h to form FeP nanocrystals of various morphologies. A representative powder XRD pattern is shown in Figure 31f. When the injected rapidly

and heated at 350 °C, the FeP nanocrystals are roughly spherical and show a slight increase in size from the Fe precursor (Figure 31b). However, if the injection of the Fe-oleylamine-TOP solution is done over 5 min, the resulting FeP nanocrystals are a mix of solid and hollow nanorods with low aspect ratios (Figure 31c). Of interest are the small, periodic spherical voids observed in several of the short nanorods in Figure 31c (denoted by a red arrow), as well as fully-hollow nanorods (denoted by a blue arrow). Presumably, several voids can form within the nanocrystal via Kirkendall effects,[20] which may coalesce into one large void (fully hollow nanorods). In contrast, when the aging temperature is lowered to 330 °C and the Fe-TOP solution is added over 5 min, only solid rods are observed with higher aspect ratios (Figure 31d). Furthermore, if the Fe nanocrystals and TOP are added over 30 minutes, very large and long nanorods are formed (Figure 31e), with diameters of approximately 30-50 nm and lengths up to ~ 300 nm. These rods appear to have formed from the coalescence of smaller rods and contain random and irregularly shaped voids. These voids could be due to the voids already present in the smaller hollow rods that coalesced to form them. Formation of Fe rods has been reported to occur in the presence of TOP and strong-binding surfactants,[90] thus the formation of FeP rods could proceed via the formation of Fe rods from the Fe seed nanocrystals in an oriented-attachment process.

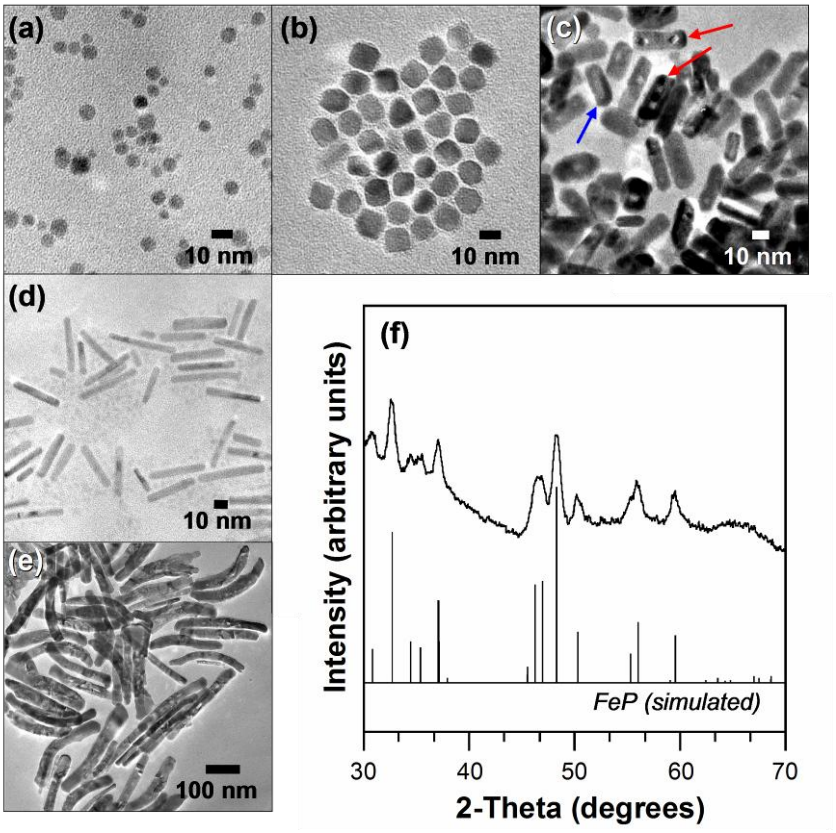

Figure 31. FeP nanocrystals of various morphologies formed from Fe nanocrystals. TEM images of (a) spherical Fe nanocrystals used as precursors and FeP nanocrystals formed from (b) rapid injection of Fe/TOP into HDA at 350 °C, (c) injection at 350 °C over 5 min, (d) injection at 330 °C over 5 min, and (e) injection at 350 °C over 30 min; (f) representative powder XRD pattern of FeP.

Other technologically interesting nanostructures can be generated by varying reaction conditions of previously reported methods. For example, in Hyeon's procedure for making Ni_2P nanorods, the slow injection of a $Ni(acac)_2$-TOP complex into TOPO at 300 °C caused anisotropic growth.[78] By injecting rapidly into 290 °C octyl ether and aging at 300 °C, porous spherical aggregates of small Ni_2P particles are formed instead of rods. A powder XRD study of the reaction over time suggests that the $Ni(acac)_2$-TOP

complex is rapidly decomposed and low-intensity XRD peaks correlating to the formation of Ni_2P are seen within 30 s (Figure 32a, top). It is possible that this reaction could bypass the *in situ* formation of a metal nanocrystal intermediate altogether; on the other hand, its formation and conversion to Ni_2P could happen so rapidly that it has not been observed within a practical timeframe. However, an increase in P:Ni content from 45:55 at 30 s and 1 min to 55:45 at 15 min (typical P:Ni ratio for phase-pure Ni_2P stabilized by TOP in Ni to Ni_2P conversion reactions) is observed by EDS. The increase in phosphorus content between 30 s and 15 min could be evidence supporting a Ni intermediate which forms less than 30 s after injection. Within 15 min, clearly discernable Ni_2P peaks are present by XRD (Figure 32a, middle) and SAED (Figure 32c, inset) and become sharp and intense after 2 h (Figure 32a, bottom and 32e, inset), indicating a highly crystalline product. A TEM image in Figure 32b depicts the initial formation of very small amorphous particles that begin to form spherical aggregates between 15 min and 1 h after injection (Figure 32c-d). By 2 h, the aggregates are highly crystalline, with a clearly discernable SAED pattern correlating to Ni_2P (Figure 32e).

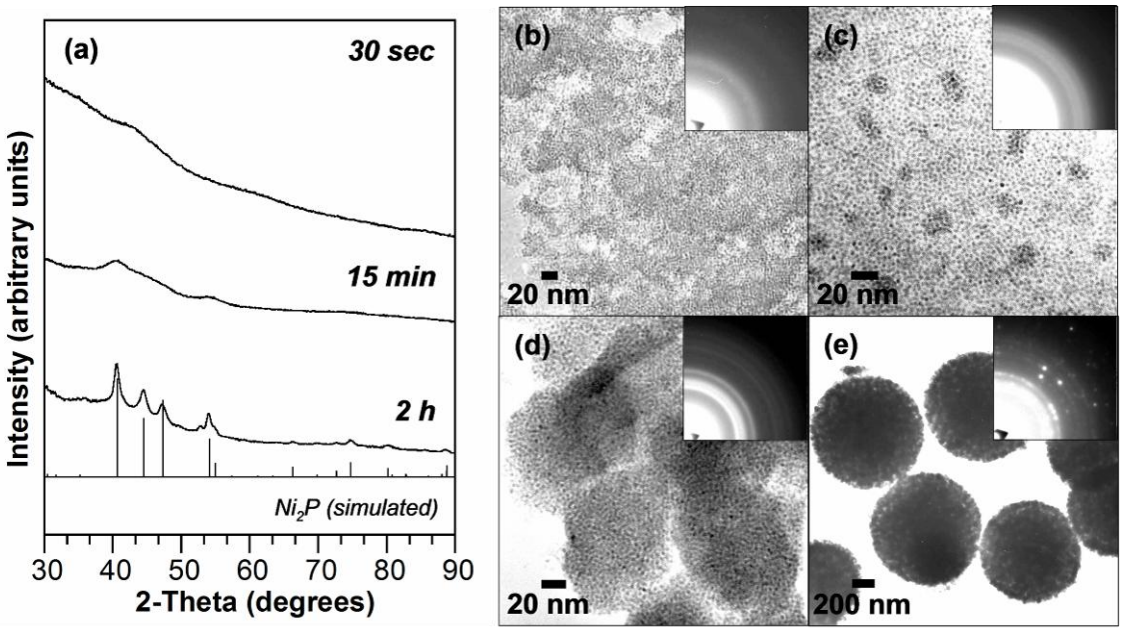

Figure 32. Formation of Ni_2P by reacting $Ni(acac)_2$ with TOP. (a) Powder XRD patterns of intermediates isolated at 30 s and 15 min and the final product after 2 h; TEM images of intermediates isolated at (b) 30 s, (c) 15 min, and (d) 1 h showing the formation and aggregation of small particles into (e) spherical Ni_2P aggregates.

The solvents and reactant ratios can be varied to change the density and size of the Ni_2P aggregates. For example in Figure 32, a 0.1 mmol Ni:1 mL TOP ratio was used, which resulted in spherical aggregates with diameters of ~ 800 nm. However, when the amount of TOP is doubled, spherical Ni_2P aggregates are half as large, but maintain similar density (Figure 33a). Decreasing the relative amount of TOP to 0.1 mmol Ni:0.5 mL TOP results in spherical Ni_2P aggregates of similar size to Figure 32, but with a higher density of constituent particles. Varying the coordinating solvent used in the reaction has the most dramatic effect on the morphology of the Ni_2P aggregates. Figure 33c shows Ni_2P formed when the $Ni(acac)_2$-TOP solution is injected into hot TOPO, which generates densely packed spherical aggregates with very small constituent

particles. Similarly, HDA creates denser aggregates (Figure 33d); however, the constituent particles are sintered causing the Ni_2P aggregate to lose most of the void space within. Furthermore, HDA caused Ni_5P_4 to nucleate as well, resulting in biphasic Ni_2P aggregates. Figure 33e shows an enlargement of the spherical aggregate contained by the red box in 33a. The high porosity likely corresponds to a high surface area, which is a beneficial characteristic in heterogeneous catalysis. Ni_2P is used as an industrial hydrotreating catalyst[91] and high surface area porous aggregates could be used as an alternative to supported Ni_2P nanocrystals.

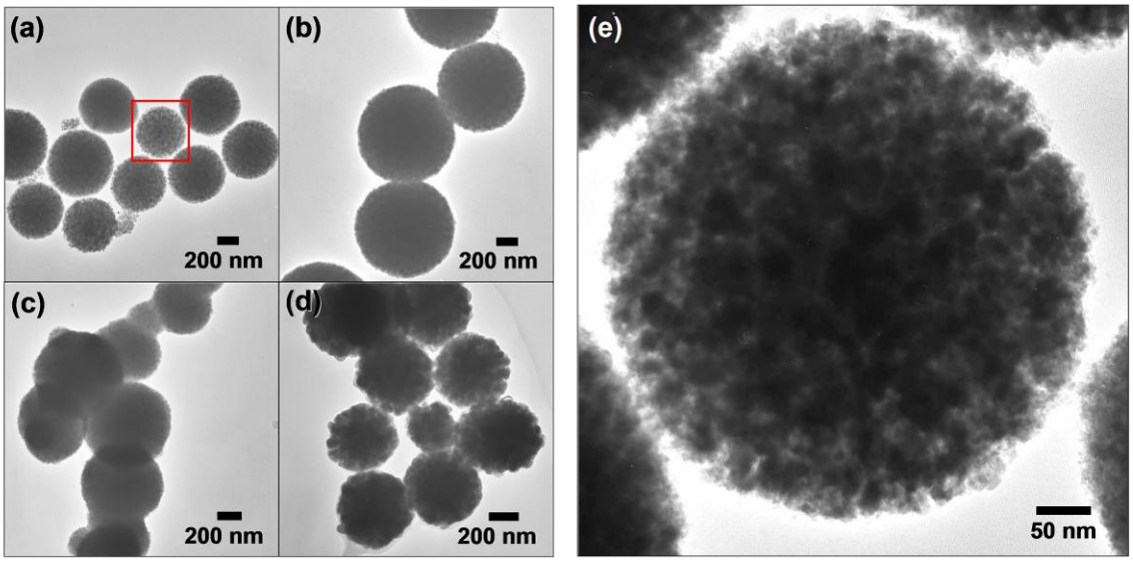

Figure 33. Ni_2P aggregates formed by varying reactant ratios and solvents. TEM images of Ni_2P formed by injecting 0.1 mmol $Ni(acac)_2$ and (a) 2 mL TOP and (b) 0.5 mL TOP into octyl ether; Ni_2P formed by injecting 0.1 mmol $Ni(acac)_2$ and 1 mL TOP into (c) TOPO and (d) HDA; (e) enlarged image of the aggregate contained within the red box in (a).

Conclusions

In this chapter, a generalized strategy for synthesizing metal phosphide nanocrystals has been discussed that capitalizes on the non-innocence of TOP in nanocrystal synthesis at elevated temperatures (> 300 °C). Using this strategy, pre-formed metal nanocrystals are converted into metal phosphides through reaction with hot TOP. We have shown that this conversion strategy can be applied to numerous transition metal phosphide systems, including many that have never been previously reported as unsupported nanocrystals. In addition to its utility for accessing a wide range of transition metal phosphides using a highly robust and unified approach, various aspects of nanostructure (e.g. size, size dispersity, and hollow sphere and rod formation) can be influenced by controlling critical aspects of the metal nanoparticle precursors and reaction conditions. This is particularly important, because robust methods exist for controlling the size and shape of single-metal nanoparticles,[92-93] and these can now serve as reactive templates for the formation of metal phosphides. Future work will focus on further generalizing this synthetic strategy, rigorously establishing the size-dependence of reactivity with TOP, and exploring size- and shape-dependent properties.

CHAPTER V

VERSATILITY AND GENERALITY: CONVERTING BULK AND NANOSTRUCTURED METALS INTO METAL PHOSPHIDES*

Introduction

Transition-metal phosphides are important materials with a wide variety of useful physical properties, including superconductivity,[94-95] magnetocaloric behavior,[96] catalytic activity,[69,91] magnetoresistance,[97] and Li intercalation capacity for battery applications.[98-100] Bulk-scale metal phosphides are typically synthesized by direct combination of the elements at high temperatures, although reactive byproducts are often formed and must be separated from the desired phosphide product.[101] Metal fluxes can also be used to grow high-quality crystals of metal phosphides at lower temperatures than are necessary using direct reactions.[102] In recent years, methods have been developed for the synthesis of metal phosphide nanocrystals. In addition to providing access to high surface area catalysts and nanostructures with interesting morphology-dependent physical properties, these strategies offer a low-temperature solution-based alternative for forming crystalline metal phosphides. For example, solvothermal reactions,[72,87-88,103] thermal decomposition of single-source organometallic precursors,[73,104] and co-reaction of organometallic reagents with phosphines[18,70-71,75-76,78,80] have all been used to generate nanocrystalline phosphides. Most of these

* Reprinted in part with permission from *Chem. Mater., 19*. Henkes, A. E.; Schaak, R. E. "Trioctylphosphine: A General Phosphorus Source for the Low-Temperature Conversion of Metals into Metal Phosphides" 4234, Copyright 2007 by the American Chemical Society.

strategies focus on reactions of trioctylphosphine (TOP) with organometallic complexes of the 3d late transition metals. In some cases, high-quality shape-controlled metal phosphide nanocrystals with interesting physical properties can be generated.

Recently, several studies of metal phosphide formation using TOP as a phosphorus source have targeted the reactivity of metals (both in bulk form and as nanocrystals) with TOP, suggesting that metals can cause cleavage of the P-C bond, resulting in diffusion of phosphorus into the metal. For example, Khanna and co-workers explored the reactivity of bulk-scale In powder with TOP to form nanocrystalline InP.[18] Chen and co-workers hypothesized a catalytic cleavage of the P-C bond caused by reaction of TOP with nanocrystalline Fe (formed in situ) during formation of FeP.[76] Chiang and Chiang reacted Ni nanocrystals with TOP to form hollow Ni_2P nanospheres.[20] In all cases, experiments have shown that TOP is not merely an innocent coordinating ligand but rather a highly reactive compound that can serve as a stabilizer, solvent, and phosphorus source in the synthesis of metal phosphide nanocrystals.

Building on these prior studies, in the previous chapter we reported a potentially general approach for synthesizing high-quality nanocrystals of transition-metal phosphides that was successful for a variety of 3d, 4d, and 5d transition-metal systems.[24-25] This method involves reacting pre-formed metal nanocrystals with TOP at 290-370 °C.[24-25] During this reaction phosphorus is liberated from TOP and diffuses into the metal nanoparticles, converting them to metal phosphides. This strategy was shown to be successful for generating nanocrystals of Ni_2P, PtP_2, Rh_2P, Au_2P_3, Pd_5P_2,

PdP_2, FeP, CoP, Cu_3P and AgP_2.[24-25] The reaction pathway that generates metal phosphide nanocrystals via "conversion chemistry" utilizes a diffusion-based mechanism. The results from our work with nanocrystals[24-25] imply that the shape, size, and size dispersity defined by the metal nanocrystal precursors can be retained in the metal phosphide product, providing a convenient route for generating high-quality nanocrystals of a large number of metal phosphide systems.

In this chapter we describe the results of our follow-up investigations aimed at exploring metal precursor versatility and size limits, and establishing further generality of this "conversion chemistry" approach to the formation of metal phosphides by extending it to new metal phosphide systems. Specifically, we show that in some cases bulk-scale metal powders can be converted into metal phosphides by simple solution-mediated reactions with hot TOP. Furthermore, using similar chemistry metal wires, foils, films, and patterned microstructures can react with TOP to produce metal phosphide coatings and microscale metal phosphide features of variable thicknesses. In all cases, there is a remarkable correlation between the morphology of the metal precursors and the metal phosphide products. Taken together, these diverse synthetic capabilities demonstrate a very general, simple, and rapid solution-mediated strategy for accessing metal phosphides from preformed metals using convenient and commercially available reagents.

Experimental Section

All reactions were carried out under argon using standard air free techniques.

Chemicals

All chemicals were used as purchased. Tri-*n*-octylphosphine (tech. 90 %), tri-*n*-octylphosphine oxide (TOPO), *n*-hexadecylamine (HDA, tech.), oleic acid (tech.), Ni powder (2.2-3.0 μm), Pd powder (0.25-0.55 and 0.5-1.7 μm), Zn powder (7 μm), Cu powder (-100 mesh), In powder (-325 mesh), Rh powder (-325 mesh), Ga pellets (6 mm diameter), Ni foil (0.01 mm thickness), and graphite (-325 mesh, conducting) were purchased from Alfa Aesar. Octyl ether (99 %), oleylamine (70 % tech.), 1,2-hexadecanediol (90 % tech.), Zn wire (0.5 mm diameter), and Zn foil (0.5 mm diameter) were purchased from Sigma-Aldrich. Mossy Zn was from Matheson Coleman and Bell. Dodecenyl succinic anhydride, Araldite 502, and benzyldimethylamine were purchased from Electron Microscopy Sciences. LX 112 was purchased from Ladd Industries. S1827 positive photoresist and MF-319 developer were purchased from Shipley.

Characterization

Powder X-ray diffraction (XRD) was performed on a Bruker-AXS GADDS diffractometer as described previously.[38] Scanning electron microscopy (SEM) was performed using a JEOL JSM-6400 scanning electron microscope operating at 15 kV. Metal powders for SEM imaging were coated with AuPd using a sputter coater. Metal

films and metal-patterned substrates were coated with conducting carbon using a metal evaporator to allow complete resolution of the phosphorus EDS signal. Optical spectroscopy was performed using a Perkin-Elmer Lambda 35 UV/vis spectrometer.

Cross sections of copper and copper phosphide wires were imaged using a Zeiss Axiophot confocal light microscope with color CCD camera. A copper wire and wires with copper phosphide coatings from various reaction times were embedded vertically in an epoxy resin. The epoxy resin was composed of 59.1 % dodecenyl succinic anhydride (hardener), 15.9 % LX 112 (epoxy resin component), 25 % Araldite 502 (epoxy resin component), and 0.2 mL of benzyldimethylamine (accelerator). The resin was dried for 24 h at ~50 °C. After drying, the cross-sectional surface of the wires was ground using a Buehler Ecomet grinder/polisher with 300, 600, and 1200 grit paper. The final stage of polishing was done with a polishing cloth and a 0.03 μm alumina powder slurry.

Bulk Metal Phosphide Powders

Ni_2P Powder. An aqueous solution of $NaBH_4$ (~ 0.05 M) was prepared, and 2 mL was used to treat 12.2 mg of Ni powder (2.2-3.0 μm) to help minimize surface oxidation. The Ni powder was sonicated in the $NaBH_4$ solution, centrifuged and washed with copious amounts of water to remove $NaBH_4$ residue, and then dried under Ar. The treated Ni powder was heated at 300 °C in 2.0 mL of TOP for 2 h and then slowly cooled and saturated with ethanol. Ni_2P powder with a slight Ni impurity was isolated by centrifugation, washed thoroughly with ethanol, and dried under Ar.

Ni_5P_4 Powder. Ni_5P_4 powder was prepared identically to Ni_2P powder, except it was refluxed in TOP (370 °C) for 2 h. $NaBH_4$-treated Ni powder (15.4 mg, 2.2-3.0 μm) was used.

Zn_3P_2 Powder. Zn_3P_2 powder was prepared by refluxing 7.3 mg of Zn powder (7 μm) in 2.0 mL of TOP for 2 h, which was then slowly cooled and saturated with ethanol. Zn_3P_2 powder was isolated by centrifugation, washed thoroughly with ethanol, and dried under Ar.

Cu_3P/CuP_2 Powder. Cu powder (-100 mesh) was treated with dilute aqueous HCl (~ 1.5 M) to remove surface oxidation and then thoroughly rinsed with NANOpure water and dried under Ar. The HCl-treated Cu powder (88.0 mg) was heated in 2.0 g of TOPO to 360 °C. At 360 °C, 2.0 mL of TOP was rapidly injected. The reaction was heated at 370 °C for 2 h and then slowly cooled and saturated with ethanol. A mixture of CuP_2 and Cu_3P powder was isolated by centrifugation, washed thoroughly with ethanol, and dried under Ar.

InP Powder. InP was prepared by first heating 111.0 mg of In powder (-325 mesh) in 2.0 mL of octyl ether to 290 °C. At 290 °C, 2.0 mL of TOP was rapidly injected. The reaction was heated at 325 °C for 2 h and then slowly cooled and saturated with ethanol. InP powder with an In metal impurity was isolated by centrifugation, washed thoroughly with ethanol, and dried under Ar.

Rh_2P Powder. Rh_2P was prepared by refluxing 15.6 mg of Rh powder (-325 mesh) in 3.0 mL of TOP for 1.5 h. At 1.5 h, 3.0 mL of TOP was injected. The reaction was heated a total of 6 h and then slowly cooled and saturated with ethanol. Rh_2P powder with a Rh metal impurity was isolated by centrifugation, washed thoroughly with ethanol, and dried under Ar

GaP Powder. GaP was prepared by refluxing an 18.6 mg Ga pellet in 2.0 mL of TOP for 2 h, which was then slowly cooled and saturated with ethanol. GaP powder with a Ga metal impurity was isolated by centrifugation, washed thoroughly with ethanol, and dried under Ar.

Pd_5P_2/PdP_2 Powders (size study). Investigations of the effect of metal precursor powder size on the phases formed were carried out using two sizes of Pd powder (0.25-0.55 and 0.5-1.7 μm) for reactions at 300 and 360 °C. The reactions at 300 °C were carried out using 15.0 mg of Pd powder (each size) and heating it in 2.0 mL of TOP at 300 °C for 2 h. The 360 °C reactions were carried out by heating 15.0 mg of Pd powder in 2.0 g of TOPO to 360 °C. At 360 °C, 2.0 mL of TOP was rapidly injected, and the reaction was further heated at 360 °C for 2 h. After heating, the reactions were slowly cooled and saturated with ethanol. Mixtures of Pd_5P_2 and PdP_2 powders were isolated by centrifugation, thoroughly washed with ethanol, and dried under Ar.

Metal Phosphide Foils and Wires

Ni_2P Foil. A piece of Ni foil (7.2 mg, 0.1 x 4 x 7 mm) was heated at 450 °C for 1.5 h in 5% H_2/95% Ar. It was then heated in 2.0 mL of TOP at 300 °C for 2 h and then slowly cooled and saturated with ethanol. The foil piece (now black) was washed thoroughly with ethanol and dried under Ar.

Zn_2P_3 Foil. A piece of Zn foil (0.24 g, 0.5 x 5 x 10 mm) was refluxed in 2.0 mL of TOP for 2 h and then slowly cooled and saturated with ethanol. The foil piece (now coated with black Zn_3P_2) was washed thoroughly with ethanol and dried under Ar.

Zn_3P_2 Wire, Mossy Lump. Zn wire (23.9 mg, 0.5 mm diameter, 1 cm length) was refluxed in 2.0 mL of TOP for 2 h and then slowly cooled and saturated with ethanol. The wire had a black Zn_3P_2 coating after reaction and was washed thoroughly with ethanol and dried under Ar. Similarly, 0.1784 g of mossy Zn was refluxed in 2.0 mL of TOP for 3 h and then slowly cooled and saturated with ethanol. Likewise, it had a black Zn_3P_2 coating after reaction and was washed thoroughly with ethanol and dried under Ar.

CuP_2/Cu_3P Wires (time study). Cu wires (75 mg, 1 mm diameter, 1 cm length) were washed with dilute aqueous HCl (~ 1.5 M) to remove any surface oxidation and then thoroughly rinsed with NANOpure water and dried under Ar. The wire pieces were refluxed for 30 min and 1, 2, and 4 h (separately) in 1.0 mL of TOP and then slowly

cooled and saturated with ethanol. The wires (with a black, crystalline phosphide coating) were washed thoroughly and carefully with ethanol and dried under Ar.

Cu_3P/Cu Foil. Cu foil (0.1209 g, 0.2 x 5 x 10 mm) was washed with dilute aqueous HCl (~ 1.5 M) to remove surface oxidation and thoroughly rinsed with NANOpure water and dried under Ar. The foil piece was refluxed in 1.0 g of HDA for 30 min (320 °C), and then 1.0 mL of TOP was rapidly injected. The reaction was refluxed 2 h more (350 °C) and then slowly cooled and saturated with ethanol. The foil piece (with a gray-black powdery coating) was washed thoroughly with ethanol and dried under Ar.

Cu_3P/CuP_2 Foil. Cu foil (0.2676 g, 0.5 x 10 x 15 mm) was washed with dilute aqueous HCl (~ 1.5 M) to remove surface oxidation and thoroughly rinsed with NANOpure water and dried under Ar. The foil piece was refluxed in 2.0 mL of TOP for 2 h and then slowly cooled and saturated with ethanol. The foil piece (with a black, highly crystalline coating) was washed thoroughly with ethanol and dried under Ar.

Metal Phosphide Thin Films

Zn Thin Film. Zn thin films were made by depositing Zn onto precleaned glass microscope slides using a BOC Edwards Auto 306 Metal Evaporation Chamber. Zn wire was used as a Zn source. Zn (100 nm) was deposited onto 10 nm Cr. The resulting

films were highly metallic and optically reflective but were not crystalline enough to obtain powder diffraction patterns.

Zn_3P_2 Thin Film. A Zn film on glass (1 x 3 cm glass slide) was refluxed in 2.0 mL of TOP for 2 h and then slowly cooled and saturated with ethanol. The Zn_3P_2 film (golden color and optically transparent) was washed thoroughly with ethanol and dried under Ar.

Au Thin Film. A Au thin film was prepared by slowly evaporating an aqueous solution of $HAuCl_4 \cdot 3H_2O$ onto a precleaned glass microscope slide. The glass slide was placed vertically in a scintillation vial, which was filled with aqueous $HAuCl_4$ solution and allowed to slowly evaporate while covered with a crystallization dish for 5 weeks. The glass was then heated at 500 °C for 2 h in 5 % H_2/95 % Ar to reduce the Au^{3+} to Au^0.

Au/Au_2P_3 Thin Film. A 1.25 x 1.5 cm piece of Au-coated glass was refluxed in 2.0 mL of TOP for 6 h total (with 1.0 mL of TOP injected at 2 and 3 h) and then slowly cooled and saturated with ethanol. The Au/Au_2P_3 film was washed thoroughly with ethanol and dried under Ar.

Supported Metal Phosphide Nanocrystals

Graphite-Supported Ni Nanocrystals. This synthesis is a modification of that used by Hyeon et al. for making Ni nanocrystals.[82] Supported Ni nanocrystals were prepared by heating 0.1110 g of $Ni(acac)_2$, 0.7604 g of graphite (-325 mesh, conducting), and 1.0 mL of oleylamine in 6.0 g of triphenylphosphine at 220 °C for 30 min, which was then slowly cooled and saturated with ethanol. A black powder was isolated via centrifugation, washed thoroughly with ethanol, and dried under Ar.

Graphite-Supported Ni_2P Nanocrystals. Ni on graphite (29.0 mg) was heated in 2.0 mL of octyl ether to 290 °C. At 290 °C, 1.0 mL of TOP was rapidly injected. The reaction was heated at 300 °C for 2 h and then slowly cooled and saturated with ethanol. The powder was isolated via centrifugation, washed thoroughly with ethanol, and dried under Ar.

Metal Phosphide Patterned Substrates

Cu Patterns on Glass. Glass microscope slides were annealed at 450 °C for 4 h, washed thoroughly with isopropanol and acetone, and dried with a stream of air. S1827 positive photoresist was spin coated onto the microscope slides at 2000 rpm (~ 3.5 μm thickness) using a SCS P6204 (8-in. bowl) nonprogrammable spin coater. The photoresist coated glass slides were exposed to UV light using a Quintel Q4000 MA mask aligner and a mask with 0.2 mm x 10 mm stripes. The exposed slide was developed in MF-319 developer, rinsed with deionized water, and dried with a stream of

air. The photo-patterned glass was then coated with 100 nm of Cu using a BOC Edwards Auto 306 Metal Evaporation Chamber. Photoresist and excess Cu were lifted off by lightly sonicating the coated glass in deionized water, leaving behind Cu stripes on glass.

Cu_3P from Cu Patterns on Glass. Cu-patterned glass slides were cut to ~ 1 x 2 cm pieces. The patterned glass was heated at 320 °C in 4 mL of TOP under Ar for 30 min and then slowly cooled and saturated with ethanol. The pattern on the glass turned a silvery gray color after completion of the reaction. The liquid was decanted, and the patterned glass was rinsed several times with ethanol and then dried under Ar.

Results and Discussion

Converting Bulk Metal Powders to Metal Phosphides

As seen in the previous chapter, metal phosphide systems that tend to form large aggregated/sintered nanocrystalline products (i.e., Au_2P_3 and AgP_2) often contain metallic impurities, leading to the conclusion that the larger particles have decreased reactivity towards the diffusion of phosphorus. Despite the limited reactivity observed for larger particle sizes in these two systems, size-dependent studies in several other systems have revealed that the reactivity of metals with hot TOP to form metal phosphides is not always limited to nanocrystalline metals. Figure 34 shows representative powder XRD data for metal phosphide powders that form from the

reaction of commercially available bulk-scale metal powders with TOP, typically under reflux conditions. (As-purchased microcrystalline powders of Mn, Fe, Nb, Ru, W, Ir, Al, Si, and Sn were found not to convert to metal phosphides under these conditions, although modifications to the procedure may facilitate similar conversions in the future.) For example, Ni_2P forms by heating 2.2- 3.0 μm Ni powder in TOP at 300 °C, while the phase that forms upon heating the same Ni powder in TOP at 370 °C is Ni_5P_4 (Figure 34a, bottom). Intermediate temperatures result in a mixture of Ni_2P and Ni_5P_4. As we observed previously for Pd-P nanocrystals[24] and now for Ni-P bulk powders, varying the reaction temperature can provide access to multiple phases in some metal-phosphorus systems.

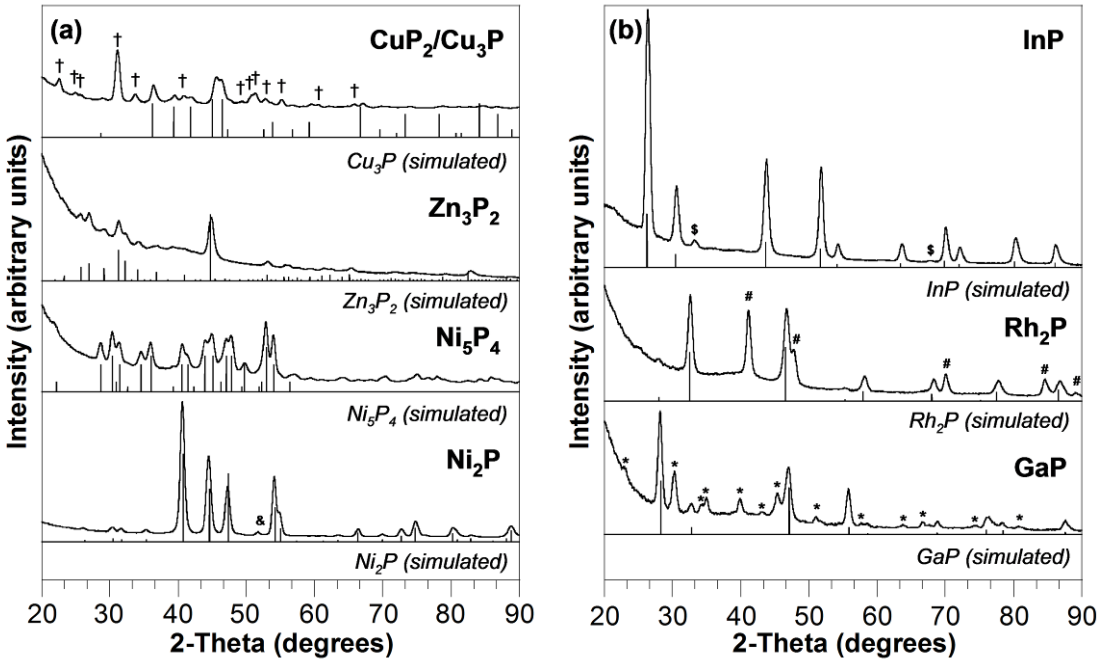

Figure 34. Powder XRD patterns for metal phosphides made from bulk metal powders. (a) Metal phosphides for which minor or no residual metal precursor impurities remain († indicates CuP_2 and $^{\&}$ indicates fcc Ni). (b) Metal phosphides with significant metal precursor impurities ($, # and * indicate In, Rh and Ga, respectively).

When Cu powder is heated to reflux in TOP, a mixture of CuP_2 and Cu_3P is formed (Figure 34a, top); a phase-pure copper phosphide has not been obtained, although no unreacted Cu remains (as determined by XRD). We hypothesize, based on observations of reactivity of TOP with Cu wires, that Cu_3P forms first on the surface of the Cu crystallites with CuP_2 growing in as more phosphorus is available for diffusion. The fact that pure Cu_3P can be obtained as nanocrystals is likely attributable to the size of the Cu source, which is quickly consumed by initial formation of Cu_3P. Consistent with this, there is some evidence that nanocrystalline CuP_2 can form upon further reaction of Cu_3P nanocrystals with TOP at reflux. Bulk Pd reacts similarly, always

forming a mixture of PdP_2 and Pd_5P_2 (Figure 35). This is in contrast to the reactivity of Pd nanoparticles, which can be made to form pure PdP_2 (360 °C) and pure Pd_5P_2 (300 °C).[24] When Pd powder with an average particle size of 0.25-0.55 μm is used, the PdP_2:Pd_5P_2 ratio is approximately 40:60 at 300 °C. Likewise, 0.5-1.7 μm Pd forms PdP_2 and Pd_5P_2 in a ratio of approximately 25:75 at 300 °C. This indicates that larger particle sizes tend to favor formation of Pd_5P_2 relative to PdP_2, perhaps because of diffusion constraints in the larger Pd particles. Formation of Pd_5P_2 is also favored by the larger Pd particles at 360 °C.

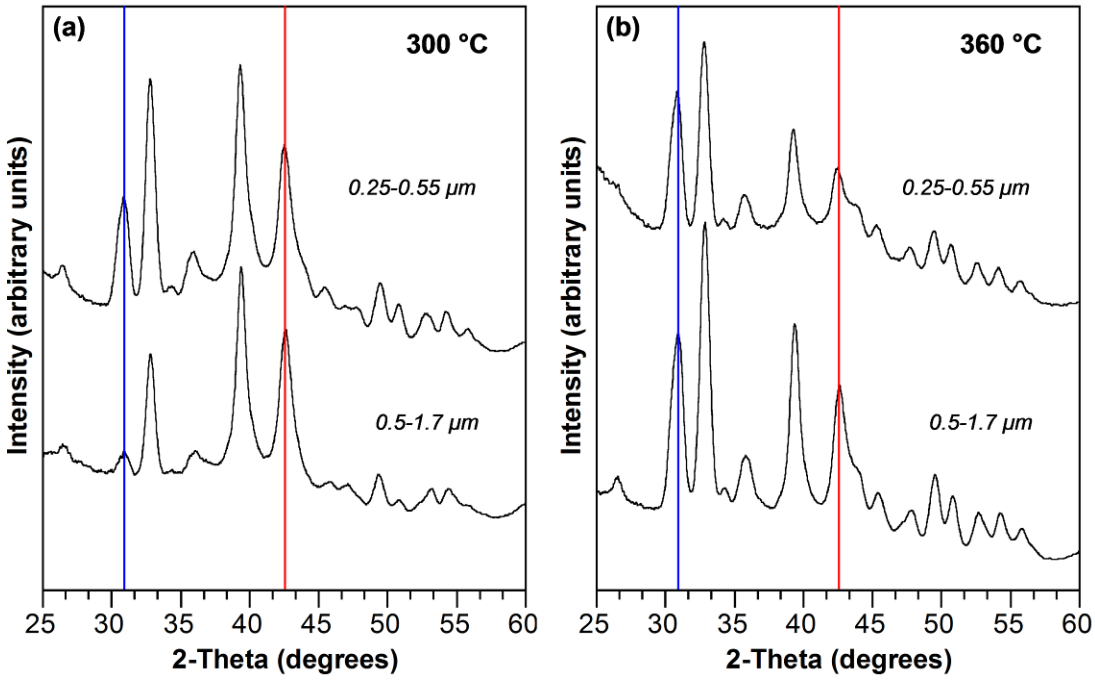

Figure 35. Phase dependence on precursor powder size. Blue and red lines correspond to non-overlapping PdP_2 and Pd_5P_2 powder XRD peaks respectively, and can be used to approximate relative amounts of each phase. (a) Pd powder heated at 300 °C in TOP for 2 h. (b) Pd powder heated in TOP/TOPO at 360 °C for 2 h. The smaller powder has a higher percentage of PdP_2 at both 300 °C and 360 °C.

Zn powder can also be reacted with TOP to form Zn_3P_2, which is an important material for photovoltaic applications,[105] lithium-ion battery anodes,[96] and agricultural pesticides.[106] Figure 1a shows the formation of Zn_3P_2 without any residual Zn. (Zn_3P_2 nanocrystals have not been prepared using this strategy because isolatable Zn nanoparticle precursors could not be prepared by standard methods. Zn_3P_2 nanocrystals and films have been prepared by other methods however.[107-109]) InP can also form from reaction of In metal with TOP, although a small In impurity remains (Figure 34b). This behavior is consistent with, and slightly improved upon, that observed previously for the incomplete reaction of In with TOP.[18] Other bulk metal powders convert incompletely. For example, Rh powder forms a mixture of Rh_2P and Rh (Figure 34b), possibly with Rh_2P passivating the Rh particles and preventing or hindering further reaction. Similarly, GaP has a significant Ga impurity. Table 4 summarizes all of the phases of metal phosphides that are accessible from bulk metal precursors as well as the key reaction conditions that generate each phase.

Table 4. Bulk-scale metal phosphides accessible using a variety of metal precursors.

Bulk metal	Precursor reaction conditions[a]	Product (via powder XRD)
Zn powder	370 °C TOP, 2 h	Zn_3P_2
wire	370 °C TOP, 2 h	Zn_3P_2
foil	370 °C TOP, 2 h	Zn_3P_2
mossy	370 °C TOP, 2 h	Zn_3P_2, Zn
film	370 °C TOP, 2 h	Zn_3P_2
Ni powder	300 °C TOP, 2 h	Ni_2P, Ni
	370 °C TOP, 2 h	Ni_5P_4
foil	300 °C TOP, 2 h	Ni_2P
	370 °C TOP, 2 h	Ni_2P, Ni_5P_4
Cu powder	370 °C TOP/TOPO, 2 h	Cu_3P, CuP_2
foil	350 °C HDA/TOP, 2 h	Cu_3P, Cu
	370 °C TOP, 2 h	Cu_3P, CuP_2
wire	370 °C TOP, 0.5-2 h	CuP_2, Cu_3P (time dependent)
patterned glass	320 °C TOP, 0.5 h	Cu_3P (characterized by EDS)
Rh powder	370 °C TOP, 6 h	Rh_2P, Rh
Ga pellet	370 °C TOP, 2 h	GaP, Ga
In powder	325 °C TOP/Oct_2O, 2 h	InP, In
Pd powder (0.25-0.55 μm)	360 °C TOP/TOPO, 2 h	PdP_2, Pd_5P_2 (~ 30% Pd_5P_2)
	300 °C TOP, 2 h	Pd_5P_2, PdP_2 (~ 60% Pd_5P_2)
Pd powder (0.5-1.7 μm)	360 °C TOP/TOPO, 2 h	PdP_2, Pd_5P_2 (~ 45% Pd_5P_2)
	300 °C TOP, 2 h	Pd_5P_2, PdP_2 (~ 75% Pd_5P_2)
Au film	370 °C TOP, 6 h	Au_2P_3, Au

[a] HDA = *n*-hexadecylamine, TOP = tri-*n*-octylphosphine, TOPO = tri-*n*-octylphosphine oxide, Oct_2O = octyl ether.

SEM micrographs of representative metal powder precursors and their resulting metal phosphide products show that the overall morphology (e.g., general aggregate size and shape) is retained, but the fine microstructure of the metal powders is lost upon reaction with hot TOP. For example, the commercially available 7 μm Zn powder that we used as a precursor consists of spherical aggregates of smaller (~ 800 nm), irregularly shaped Zn particles (Figure 36a). After conversion to Zn_3P_2, the average size of the aggregates remains similar. However, within the aggregates the primary particles are notably larger and fused together, although remnants of the original aggregate structure are still observable (Figure 36b). Similarly, the Ni powder precursor (Figure 36c) retains its overall spherical morphology and size after conversion to Ni_2P and Ni_5P_4 (Figure 36d,e), but reaction with TOP produces nickel phosphides that have lost the sharp facets of the Ni crystallites in the precursor powder. Overall, the conversion of micrometer-sized bulk powders to metal phosphides is a harsh reaction that changes the fine microstructure of the metal but manages to retain the average mesh size and morphology of the metal powder precursor. Analogous reactions with nanocrystals appear to proceed with less aggregation and change of nanostructure because surface stabilizers are present and the particles are more easily dispersible in the solvent (and thus remain better separated from one another).

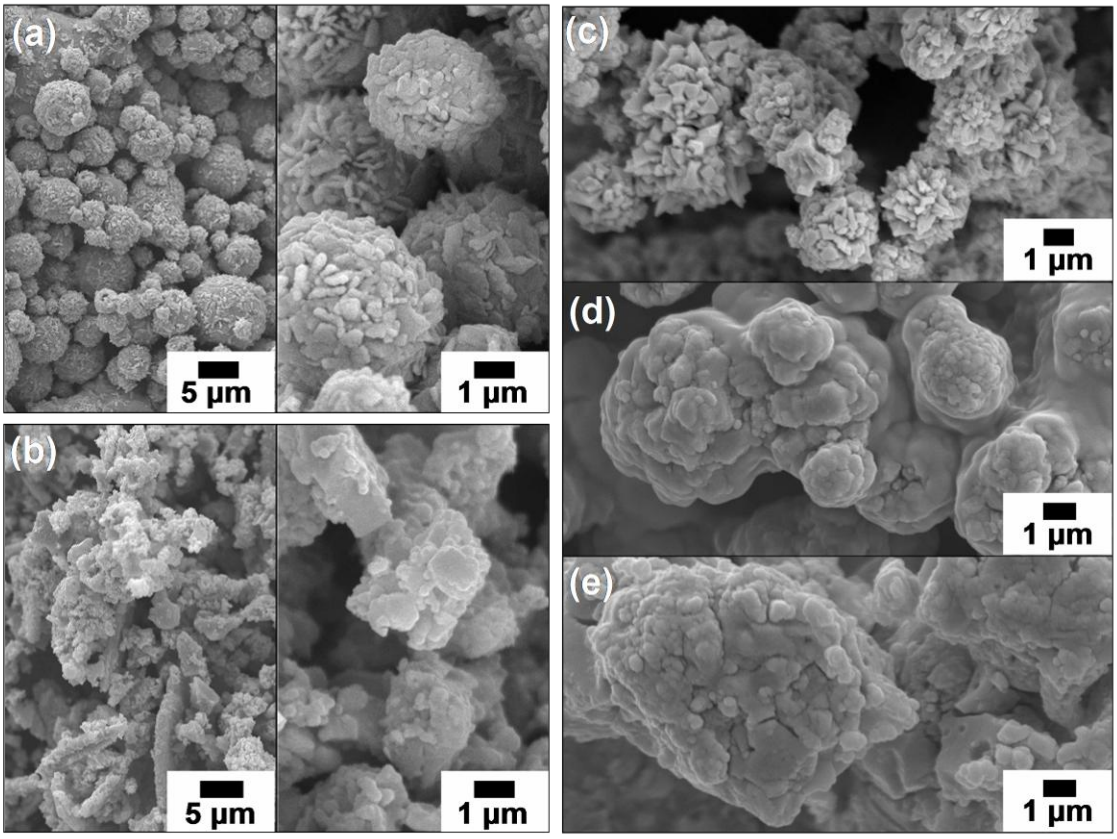

Figure 36. SEM images of metal precursor powders and the metal phosphides formed from them. (a) 7 µm Zn powder (Alfa Aesar); (b) Zn_3P_2 formed from (a); (c) 2.2-3.0 µm Ni powder (Alfa Aesar); (d) Ni_2P and (e) Ni_5P_4 formed from (c).

Coating Metal Wires and Foils with Metal Phosphides

In addition to powders, other bulk-scale metals such as wires and foils also react with hot TOP to form metal phosphides. Unlike the micrometer-sized metal powders, which often convert completely to metal phosphides, the metal wires and foils react with TOP to form coatings with penetration depths typically approaching several hundreds of micrometers. For example, when mossy Zn is reacted under conditions that are analogous to those used for Zn powder, a coating of Zn_3P_2 is readily formed. Similar

reactivity occurs for Zn wire and foil. Powder XRD data for Zn_3P_2-coated mossy Zn, Zn wire, and Zn foil are shown in Figure 37a, and digital photographs of the precursors and products are shown in Figure 37c. Similarly, Ni foil can be coated with Ni_2P (Figure 37b). Cu foil and wire can also be coated with Cu_3P/CuP_2 by refluxing in TOP (Figures 37b,d).

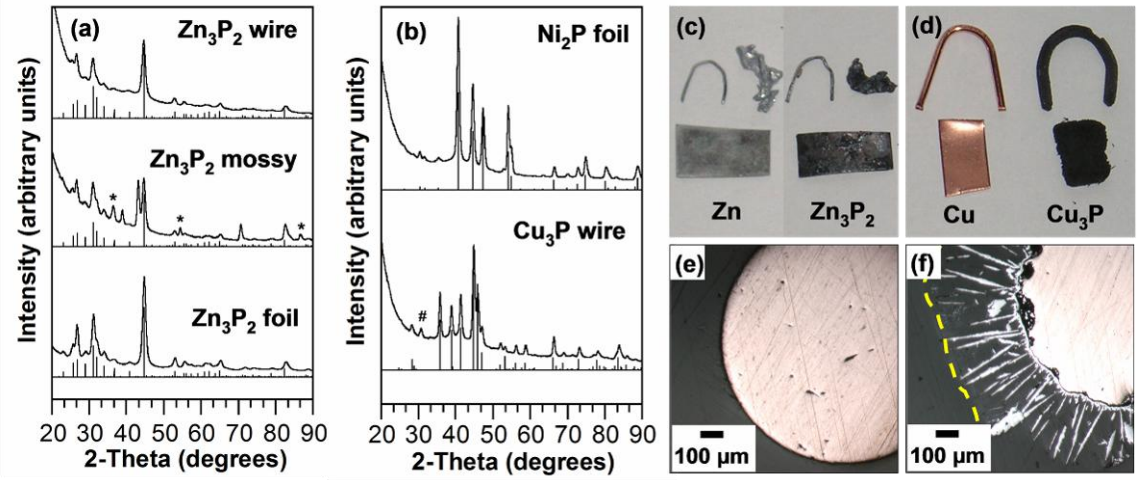

Figure 37. Powder XRD patterns for (a) Zn_3P_2 coatings made from various Zn precursors (Zn impurity is represented by an asterisk); (b) Ni_2P made from Ni foil and Cu_3P wire coating (with CuP_2 impurity represented by $^{\#}$) made from Cu wire; digital photographs of (c) Zn wire, foil and chunk (mossy) and Zn_3P_2 made by refluxing in TOP; (d) Cu metal wire and foil and Cu_3P (with CuP_2 impurity) made by refluxing in TOP; (e) cross-sectional view of 1 mm diameter Cu wire and (f) a resulting Cu_3P (with CuP_2 impurity) coating formed (~ 300 µm thickness) around the Cu wire after refluxing 30 minutes in TOP. The dashed yellow line denotes the thickness of the coating and is intended to guide the eye.

Insight into the penetration depth of the phosphide coatings is shown in Figure 37e,f. In this experiment a Cu wire (Figure 37e) and a Cu wire refluxed in TOP for 30 min (Figure 37f) were embedded vertically in an epoxy resin, and the polished cross-

sectional surface was imaged using an optical microscope. The Cu wire cross section (1 mm diameter) shows no visible surface coating (Figure 37e). However, the Cu wire coated with predominantly Cu_3P (along with a small amount of CuP_2) reveals a Cu metal core (with a diameter that has decreased to 0.95 mm) surrounded by a ~ 300 μm phosphide coating (Figure 37f).

Converting Metal Films, Supported Nanoparticles, and Patterned Substrates to Metal Phosphides

In addition to nanocrystalline and bulk metals, nanostructured and patterned metals can also be converted to metal phosphides with retention of the characteristic features of the nanoscale metal precursors. For example, thin films of Zn (100 nm) made by thermally evaporating Zn metal onto a clean glass slide (with 10 nm Cr adhesion layer between glass and Zn) can be refluxed in TOP to form Zn_3P_2 films (Figure 38a). SEM images shown in Figure 38b,c show how the surface of the film changes during reaction with TOP. The Zn film coarsens after refluxing in TOP for 2 h to form Zn_3P_2. EDS shows a Zn:P ratio of 42:58 for the Zn_3P_2 film (Figure 38f,g). Although powder XRD shows a Zn_3P_2 film with low crystallinity (due to Zn film preparation method), the most intense peak of Zn_3P_2 is present near 44.7 degrees 2θ (Figure 38e, PDF card no. 1-074-1156). The Zn_3P_2 film is optically transparent (photo, Figure 38a) with a peak at ~ 470 nm in the UV-vis spectrum (Figure 38d), corresponding to a blue shift relative to bulk Zn_3P_2.[108] This is consistent with quantum confinement effects previously reported for Zn_3P_2 films and nanocyrstals.[108b,109] Zn_3P_2, a

semiconductor with a band gap in the range of visible light (1.51 eV),[108] has had recent interest as a low-cost semiconductor for use in hybrid solar cells because it absorbs light at the most intense wavelength of sunlight.[105,108-109] Reactions of Zn films, which are easily deposited by thermal evaporation, with TOP, a commercially available reagent, may provide a convenient alternative method for producing Zn_3P_2-based solar cells.

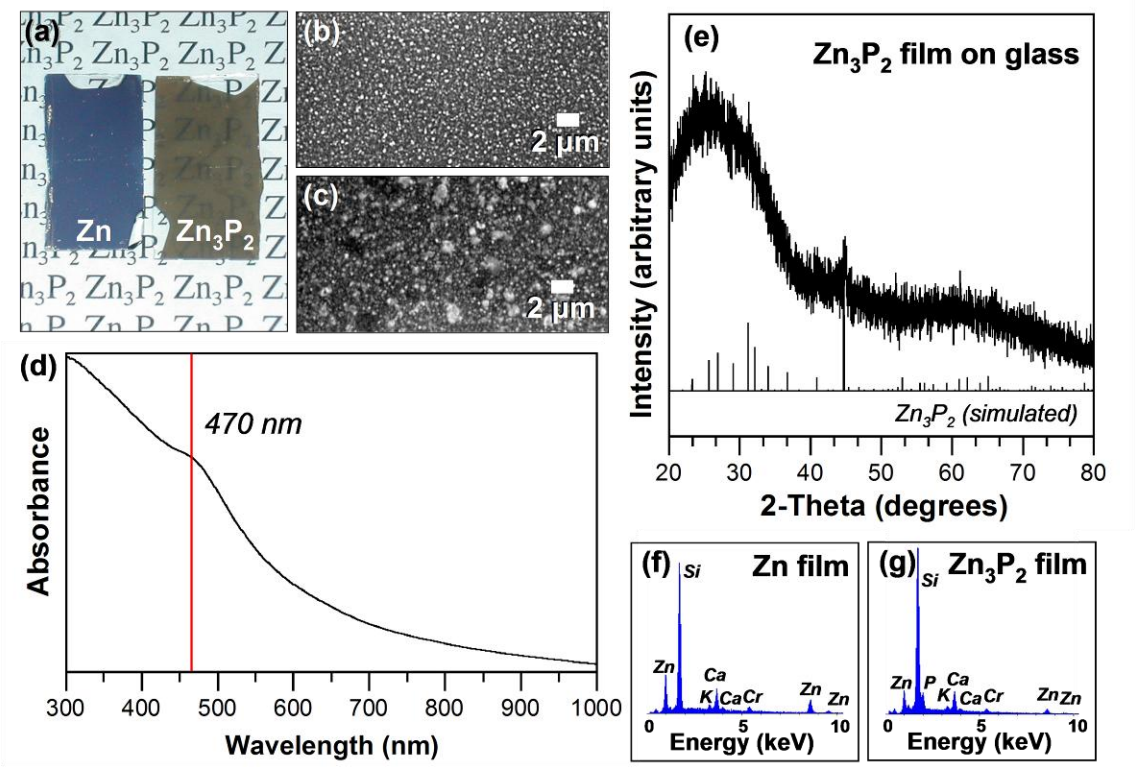

Figure 38. Zn_3P_2 film made by reacting 100 nm Zn film with hot TOP: (a) digital photograph comparing Zn film precursor with transparent Zn_3P_2 product; SEM images of (b) Zn film and (c) Zn_3P_2 film; (d) optical spectrum of Zn_3P_2 film with λ_{max} at ~ 470 nm; (e) powder XRD pattern for Zn_3P_2 film on glass (significant background from glass and small sample size); EDS spectra for (f) 100 nm Zn film on glass (with 10 nm Cr adhesion layer) and (g) Zn_3P_2 film. (Si, Ca and K are present in the glass used as a substrate.)

In addition to metal films, metal nanoparticles immobilized on high surface area supports for applications in catalysis can also be converted to supported metal phosphides by reaction with TOP. Ni_2P is known to be highly active for hydrodesulfurization reactions and is superior to traditional hydrotreating catalysts such as sulfided Ni-Mo, which becomes deactivated over time due to sulfur build-up that changes the surface chemistry of the catalyst.[91] Ni nanocrystals supported on graphite can be made by heating a solution of $Ni(acac)_2$ and graphite in oleylamine and triphenylphosphine at 220 °C for 30 min. The graphite-supported Ni nanoparticles can be isolated easily by centrifugation, washed with ethanol, dried under Ar, and re-dispersed in octyl ether. After injecting TOP into a 290 °C octyl ether suspension of the graphite-supported Ni nanoparticles and aging at 300 °C for 2 h, the supported Ni nanoparticles convert to Ni_2P while remaining on the support. Characterizing graphite-supported Ni nanoparticles by XRD is challenging because of the significant peak broadening and the presence of peaks that overlap with those of graphite. The peak broadening is consistent with XRD data reported for nonsupported Ni nanoparticles made by a similar method.[24,82] Because the most intense fcc Ni peak (*111*) overlaps with the *011* peak of graphite, the relative ratio of this peak to other graphite peaks can be used to infer that Ni is present (Figure 39a, middle). TEM and EDS further confirm the presence of Ni nanoparticles supported on graphite. Figure 39b shows a TEM image with small, spherical particles supported on the graphite, with the *200* peak of fcc Ni indicated on the SAED pattern.

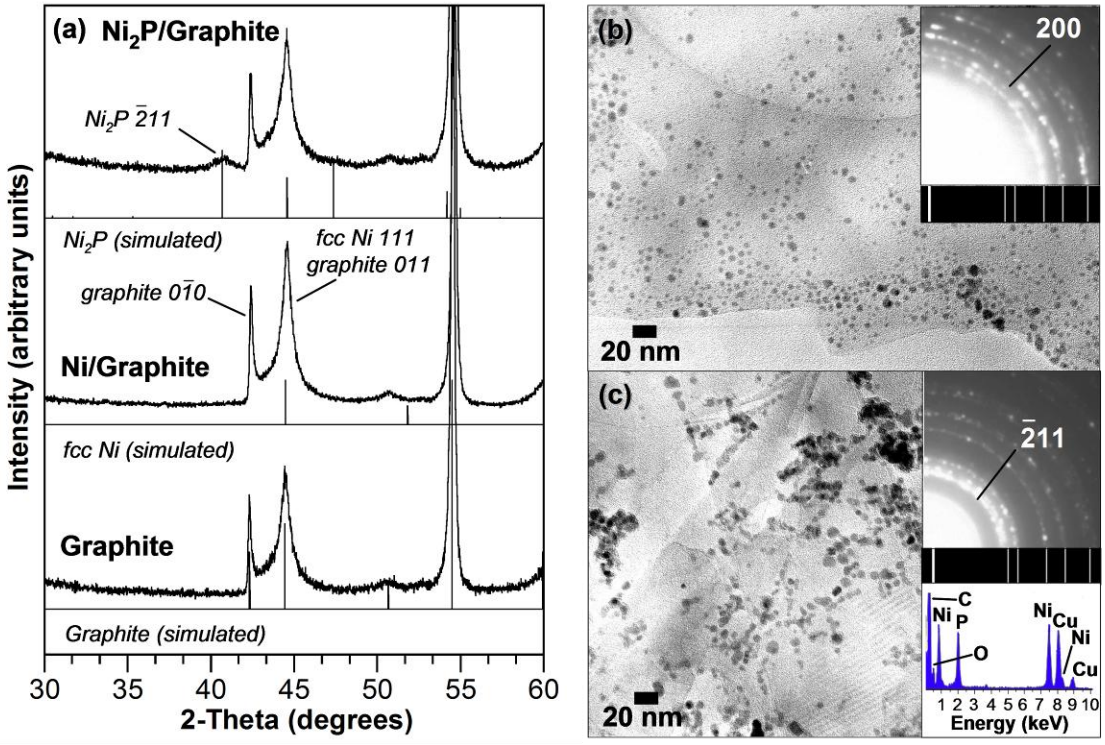

Figure 39. (a) Powder XRD for graphite, fcc Ni nanoparticles supported on graphite (Alfa Aesar, conducting, -325 mesh), and Ni_2P made from Ni nanoparticles supported on graphite. The relative ratios of the intensities of the graphite *0-10* and *011* peaks indicate that fcc Ni is present, because the *111* peak of fcc Ni is superimposed over the graphite *011* peak. TEM images for (b) Ni on graphite and (c) Ni_2P formed from the reaction of (b) with TOP at 300 °C with EDS inset. Key peaks are indicated in SAED.

After reaction with TOP, the graphite-supported Ni nanoparticles convert to Ni_2P. The peak in the XRD pattern at 40.7° 2θ is consistent with the *2-11* reflection of Ni_2P, and the breadth of the peak is as expected based on retaining the small particle size of the Ni precursor in the Ni_2P product (Figure 39a, top). Figure 39c shows a TEM micrograph of supported Ni_2P, which shows that the morphology and size are indeed conserved during the chemical transformation. SAED and EDS also confirm that Ni_2P is present: the *2-11* peak is visible in the SAED pattern and the phosphorus content

increases significantly as compared to the supported Ni particles, which only contain a small amount of phosphorus from the phosphine stabilizer (Figure 39c). Formation of supported Ni_2P nanocrystals by this method is significant because it provides an alternative to the higher temperature methods involving H_2 reduction of nickel phosphates[91,110] or use of phosphine gas as a phosphorus source in a reaction with supported nickel.[111]

Further versatility of this "conversion chemistry" approach of forming metal phosphides is demonstrated by the on-support conversion of microscale lithographically-defined metal patterns into metal phosphide patterns. Copper stripes photolithographically patterned on a glass substrate (Figure 40a) can be converted to Cu_3P stripes (Figure 40b) by heating the Cu-patterned glass in TOP at 320 °C for 30 min. SEM micrographs (Figure 40) show that while the linear features of the Cu pattern and the center-to-center distance between stripes remain unchanged in the Cu_3P product, their width decreases and they begin to curl up at the edges, indicating that the adhesion between the glass and the copper is somewhat compromised during reaction with hot TOP. The EDS spectrum (Figure 40e) and element maps (Figure 40d,f) show that the stripes are composed of both copper and phosphorus. While the conversion reaction is harsh (in this case, resulting in diminished quality of the patterned features for the product), it represents an important proof-of-concept that on-substrate conversions are possible and implies that systems with better adhesion to a substrate can be converted into phosphides using this strategy.

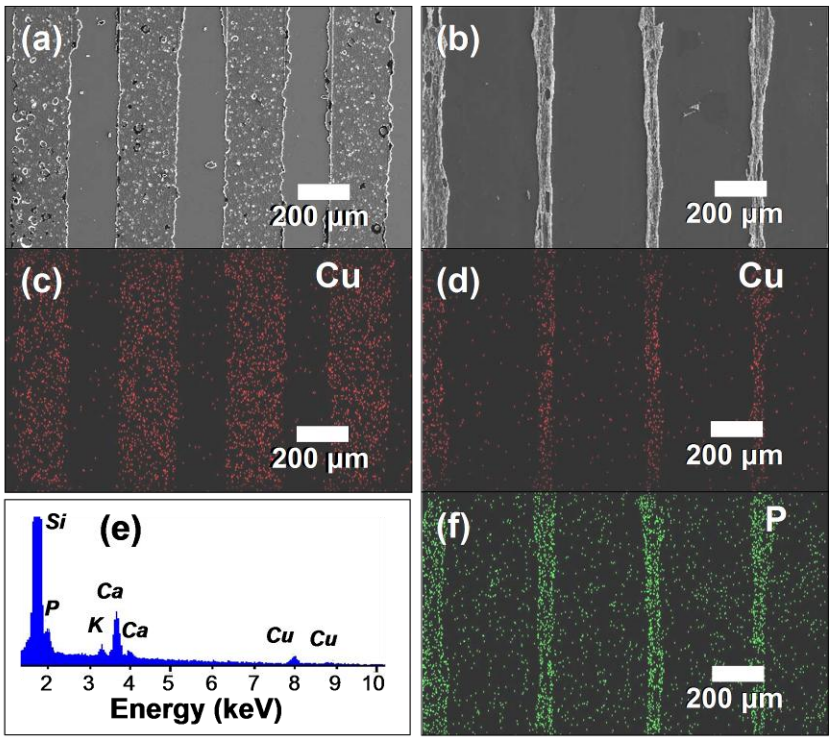

Figure 40. Microstructured Cu_3P patterns on a glass substrate made by reacting lithographically patterned glass-supported Cu patterns with hot TOP: (a) SEM image and (c) EDS map of lithographically patterned Cu stripes; (b) SEM image and (d,f) EDS map of Cu_3P stripes; (e) EDS spectrum for Cu_3P stripes (Ca, K, and Si are present in the glass substrate).

Conclusions

In this chapter we have shown that in addition to metal nanocrystals, the phosphide conversion strategy can accommodate a diverse range of bulk and nanostructured metals as precursors to metal phosphides. TOP can be used as a reactive phosphorus source to convert bulk-scale metal powders, foils, wires, films, supported nanocrystals, and patterned substrates into phosphides. This strategy appears to be general for many transition-metal and post-transition-metal systems. Considering the

number of systems and diversity of morphologies and length scales over which the chemistry can occur, this represents a general, unified, and robust strategy for forming metal phosphides using readily available reagents and metal precursors. Furthermore, since there is some degree of morphology retention between the metal precursors and metal phosphide products, it may be possible to use this chemistry to more rigorously control the size, dispersity, and shape of a wide range of metal phosphide materials with technological applications. Finally, since crystalline metal phosphides can be formed at low temperatures (< 370 °C), this represents an alternative to traditional high-temperature and flux-based strategies for synthesizing metal phosphides and as such may lead to new nonequilibrium phases.

CHAPTER VI

TEMPLATE-ASSISTED SYNTHESIS OF SHAPE-CONTROLLED NANOCRYSTALS: A CASE STUDY OF Rh_2P*

Introduction

Because of quantum effects in nanocrystals[112] and the differences in properties between nanoscale and bulk materials,[113] the development of simple, efficient, and general methods for nanocrystal synthesis is becoming increasingly important. In particular, the interesting changes in the properties of nanoscale materials relative to their bulk analogues are often linked to the shape and morphology of the nanocrystals.[113-114] As a result, understanding and fine-tuning the synthetic variables that induce shape control in nanocrystals can allow one to control the properties of a material, for example in catalysis[115] and optics.[116-117] While there exist a growing number of well-controlled methods for synthesizing metal nanocrystals with precise sizes and shapes (i.e., nanorods, nanocubes, and tetrapods), most are only applicable for single-metal systems[118-119] and some simple binary and alloy phases.[120] Expanding and generalizing these synthetic capabilities to more complex multi-element systems, which is necessary for developing advanced applications and studying size-shape-structure-property interrelationships in exotic nanoscale solids, remains a significant challenge. In particular, generating high-quality multi-element nanocrystals requires that several key

* Reprinted in part with permission from *Inorg. Chem., 47*. Henkes, A. E.; Schaak, R. E. "Template-Assisted Synthesis of Shape-Controlled Rh_2P Nanocrystals" 671, Copyright 2008 by the American Chemical Society.

issues be simultaneously addressed, including availability of appropriate soluble precursors, kinetics of precursor reduction or decomposition, co-nucleation of the elements into the desired phase, and controllable anisotropic growth (for shape control).[37,121-122] These issues, and the interplay among them, often make it difficult to readily apply the concepts developed for the shape-controlled synthesis of single-metal nanocrystals to even the simplest multi-metal systems.

Recognizing these challenges, a straightforward strategy for minimizing these synthetic complexities is to use single-metal nanocrystals as reactive templates that convert to a desired multi-metal phase while retaining the morphology of the single-metal nanoparticle precursor. Because there are many methods for forming metal nanocrystals,[118-119,37,121-123] they can serve as readily available reagents for conversion into more complex materials. This approach has been used quite successfully to generate metal selenide nanowires,[14] silver iodide nanoplatelets,[124] and hollow nanostructures of metal sulfides,[12-13] selenides,[12,125] oxides,[12] and late transition metal alloys.[126] Our group has been expanding this strategy to more complex solids, such as multi-metal intermetallic compounds[7-10] and transition metal phosphides.[24-25] For example, our group[24-25] and the Chiang group[20] have both recently shown that metal nanocrystals react with hot trioctylphosphine (TOP) to form metal phosphides. These investigations suggest that the size and shape of the metal nanoparticle precursor can influence the shape of the metal phosphide product.

While there are several reports describing the synthesis of high-quality, single crystal metal phosphide nanorods and wires,[70,77-78,80,127-128] the anisotropic growth is

influenced by the stabilizers present and the constant supply of an organometallic-phosphine complex feedstock, which is not easily modified to create more complex and varied morphologies using standard one-pot reactions. This is in contrast to many single-metal systems, which can be made to form a variety of elaborate shapes that include rods, cubes, octahedra, tetrahedra, icosahedra, tetrapods, bipyramids, triangular and hexagonal nanoplates, belts, and hollow derivatives.[117b,118-119] Here we report the synthesis of rhodium phosphide (Rh_2P) nanocrystals with a variety of complex morphologies, including cubes, triangles, and multipods. This represents the most morphologically diverse library of metal phosphide nanocrystals reported to date. Importantly, these morphologies have not been reported for *any* metal phosphide nanocrystals, yet are straightforward to access using existing shape-controlled metal nanocrystals as templates. Furthermore, we show that these nanocrystal shapes can be made hollow by exploiting a Kirkendall mechanism.[12,20,24] Finally, we establish the critical role that surface stabilizers have on allowing a metal nanocrystal to be transformed, in a shape-retaining manner, into a metal phosphide nanocrystal.

Our prototype system for these studies, Rh/Rh_2P, was chosen for several reasons. As a metal nanoparticle template for inducing shape control in a derivative system, Rh is ideal since it is possible to synthesize Rh nanocrystals in a variety of elaborate shapes.[93,129-132] While other metal phosphide systems are more technologically relevant and have been studied in more detail (e.g. MnP, FeP, InP, and Ni_2P),[70,75,78,91,133] the corresponding metal nanocrystal precursors tend to not be as readily available in the diversity of shapes reported for Rh. This allows Rh/Rh_2P to serve as the most useful

model system for shape-controlled metal/phosphide conversions. Our prior studies have shown that spherical Rh nanoparticles convert cleanly to Rh_2P upon reaction with hot TOP.[24] Thus, the conversion reaction for this system is robust and therefore is ideal for applying to more complex nanocrystal morphologies such as those achievable for Rh. Finally, Rh_2P is a known superconductor (T_c = 1.3 K).[94] While we have not probed the low-temperature electronic and magnetic properties of the shape-controlled Rh_2P nanocrystals, it is reasonable to anticipate that advances in the shape-controlled synthesis of this and related functional solids as high quality single-domain nanocrystals will provide the materials necessary in the future for advanced physical property studies in the nanometer size regime.

Experimental Section

Chemicals

Rhodium(III) chloride hydrate (99.99 %, $RhCl_3 \cdot xH_2O$), silver(I) nitrate (99.9 %, $AgNO_3$), poly(vinylpyrrolidone) (40,000 M.W., PVP), ethylene glycol (99 %, EG), tri-n-octylphosphine (tech. 90 %, TOP), tri-n-octylphosphine oxide (98 %, TOPO), and oleic acid (tech.) were used as purchased from Alfa Aesar. Sodium hexachlororhodate(III) (Na_3RhCl_6), oleylamine (tech. 70 %), and octyl ether (99 %) were used as purchased from Aldrich.

Characterization

Powder X-ray diffraction was performed on a Bruker-AXS GADDS diffractometer using microdiffraction techniques as previously described.[38] Electron microscopy and electron diffraction were performed on a JEOL JEM-2010 transmission electron microscope (TEM). Energy dispersive spectroscopy (EDS) was performed using an Oxford Instruments INCA Energy TEM system.

Synthesis of Rh Nanocrystals

Rh cubes and octahedra. Rh cubes and octahedra (collectively referred to as "cube-derived nanocrystals") were synthesized using a modification of a method reported by Yang and co-workers for synthesizing Pd and Pt nanocubes in air.[132] (Rh nanocrystals have not previously been reported using this procedure.) A 0.5 mL volume of a 0.002 M solution of $AgNO_3$ in EG was added to 2.50 mL EG and heated to 190 °C. 36.1 mg Na_3RhCl_6 in 1.50 mL EG and 125.2 mg PVP in 3.00 mL EG were slowly and simultaneously injected into the Ag^+/EG solution over 16 min. The reaction was heated for 5 additional min at 190 °C, and then cooled to room temperature. The volume of the reaction solution was quadrupled with acetone and centrifuged at 5000 rpm. The precipitate was discarded. The supernatant was collected, its volume tripled with 3:1 hexanes:ethanol, and centrifuged again at 3000 rpm to isolate cube-shaped particles.

Rh nanocrystal seeds. Rh nanocrystal seeds were synthesized using a modification of a method reported by Tilley, Somorjai and co-workers for synthesizing

5.5 nm seeds.[129] A 10.0 mg amount of $RhCl_3 \cdot xH_2O$ and 50.0 mg PVP in 1.00 mL EG were rapidly injected into 4.0 mL EG at 190 °C in air. The reaction was heated for 1 hour at 190 °C. The solution was cooled to room temperature and an aliquot was used in the synthesis of Rh triangles. TEM micrographs (Figure 41) revealed that the seeds had an oblong morphology.

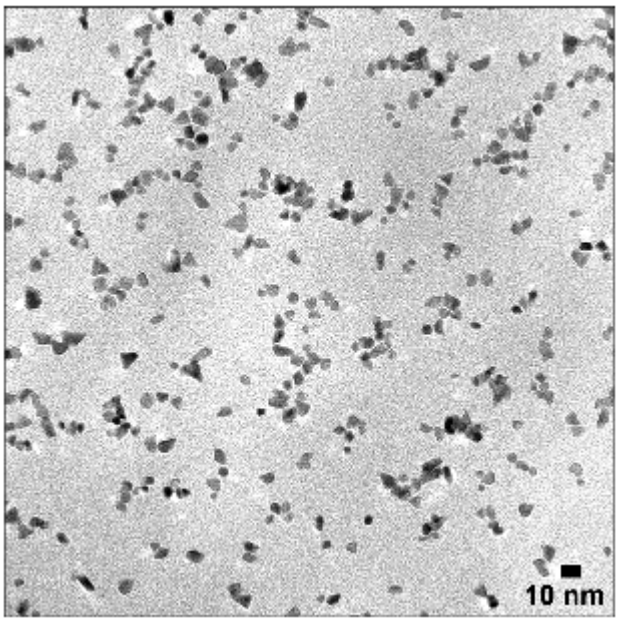

Figure 41. TEM image of Rh nanocrystal seeds used in the synthesis of Rh triangle derived nanocrystals.

Rh triangles. Rh triangle and triangle derivatives (twinned and etched triangles) were prepared based upon methods reported by Tilley, Somorjai and co-workers for synthesizing Rh multipods from Rh seeds in air.[129] A 1.00 mL volume of Rh seed nanocrystals was added to 1.00 mL EG and heated to 140 °C. An 18.9 mg amount of $RhCl_3 \cdot xH_2O$ and 50.0 mg PVP in 1.00 mL EG were slowly injected into the EG/Rh seed

solution at 140 °C over 5 min. The reaction was heated for 5 additional min at 140 °C, and then cooled to room temperature. The particles were precipitated by doubling the volume of the solution with acetone. The particles were isolated by centrifugation, and then washed with acetone and small amounts of ethanol in acetone.

Rh multipods (thin arms). Rh multipods with thin arms were synthesized by modifying a method reported by Tilley, Somorjai and co-workers.[129] An 18.9 mg amount of $RhCl_3 \cdot xH_2O$ in 0.80 mL EG and 52.0 mg PVP in 0.800 mL EG were slowly and simultaneously injected into 2.00 mL EG at 110 °C over 5 min in air. The reaction was heated at 110 °C for 5 additional min, and then cooled to room temperature. The volume was doubled with acetone to precipitate particles. The particles were isolated by centrifugation, and then washed with small amounts of ethanol in acetone.

Rh multipods (thick arms). Rh multipods with thick arms were synthesized according to the procedure reported by Xia and co-workers,[93] except that 40k MW PVP was used instead of 55k.

Conversion of Rh to Rh_2P

Rh_2P cubes. Rh_2P cubes were synthesized by dispersing 1.4 mg Rh cube-derived nanocrystals into 1.0 mL TOP with 0.25 mL ethanol and 0.50 mL oleylamine. This solution was injected into 1.0 g TOPO at 360 °C under Ar and aged for 1 h after injection at 330 °C. After the reaction was cooled, it was saturated with ethanol and

centrifuged at 13k rpm. The isolated particles were washed with ethanol and small amounts of hexanes, and then dried under Ar.

Rh_2P triangles. Rh_2P triangles were synthesized by dispersing 2.0 mg Rh triangle-derived nanocrystals into 1.0 mL TOP with 0.50 mL oleylamine. This solution was injected into 1.0 g TOPO at 360 °C under Ar and aged for 1 h at 360 °C. The reaction was cooled and the particles isolated and washed as described above.

Rh_2P multipods (thin arms). Rh_2P multipods with thin arms were synthesized by dispersing 1.5 mg Rh multipods (thin arms) in 1.0 mL TOP with 0.500 mL ethanol and 0.50 mL octyl ether. This solution was injected into 1.0 g TOPO at 360 °C under Ar, and then aged for 1 h after injection, eventually reaching 360 °C. The solution took approximately 20 min to return to 360 °C, because injecting a substantial amount of ethanol decreased the temperature instantly (~ 320 °C). After 1 h, the reaction was cooled and the particles were isolated and washed as described above.

Rh_2P multipods (thick arms). Rh_2P multipods with thick arms were synthesized using Rh multipods that had been mixed with oleylamine immediately after their synthesis. A 4.7 mg amount of Rh multipods (thick arms) was dispersed in 1.0 mL TOP. This solution was injected into 1.0 g TOPO at 360 °C under Ar, and then aged for 1 h at 340 °C. The reaction was cooled and the particles were isolated and washed as described above.

Results and Discussion

Like other transition metals that crystallize in an fcc structure, rhodium can form nanocrystals with various morphologies.[93,129-132] The formation of regular polyhedral nanocrystals is influenced by the stabilizing polymer PVP, poly(vinylpyrrolidone), as has been seen for other metals such as Au, Pd, Pt and Ag.[118] By varying the Rh^{3+}:PVP ratios, the reaction temperature, and the Rh^{3+} precursor, four separate nanocrystal morphologies can be accessed, as seen in the transmission electron micrographs (TEM) in Figure 42. Cube-derived Rh nanocrystals, which collectively include a variety of single-crystal cubes and octahedra (Figure 42a), can be made by modifying a previously reported method for making Pd and Pt nanocubes.[132] Similarly, Rh triangle derivatives, including single-crystal and multiply twinned triangles and tetrahedra (Figure 42b), can

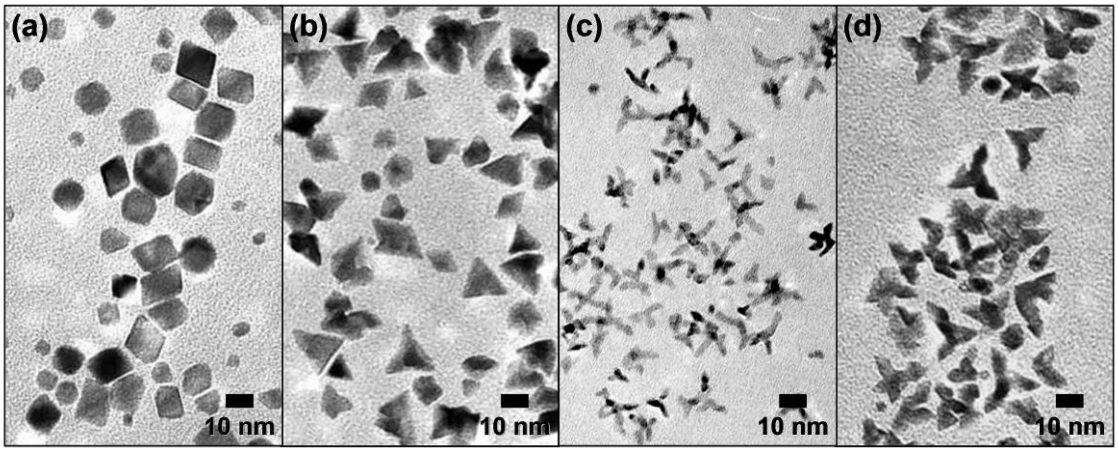

Figure 42. TEM images of Rh nanocrystals used as precursors: (a) cube derivatives (including cubes and octahedra), (b) triangle derivatives (including twinned and etched triangles), (c) thin-armed multipods, and (d) thick-armed multipods.

be formed when Rh seed crystals are used (Figure 41).[129] Rh multipods, which are a mixture of tripods and tetrapods, can be made in two different ways. The first method, based on a modification of work reported by Tilley, Somorjai, and co-workers[129] using $RhCl_3$ as the Rh^{3+} source, results in multipods with long, thin arms that grow around a spherical core (Figure 42c). The second method, developed by Xia and co-workers,[93] utilizes Na_3RhCl_6 as the Rh^{3+} source and results in single crystal tripods and tetrapods (Figure 42d) with arms that have varying thickness as they branch out from the center. For each morphology of Rh nanocrystals, the samples are phase pure (fcc Rh) by powder X-ray diffraction (XRD, Figure 43a) and selected area electron diffraction (SAED, Figure 43 inset). These four distinctive shapes of Rh nanocrystals, which we can synthesize with roughly the same level of shape purity that has been reported in the literature (see Table 5 for statistical analysis), can serve as templates for conversion into Rh_2P. The morphology of the Rh_2P product is defined by the morphology of the Rh nanocrystal templates.

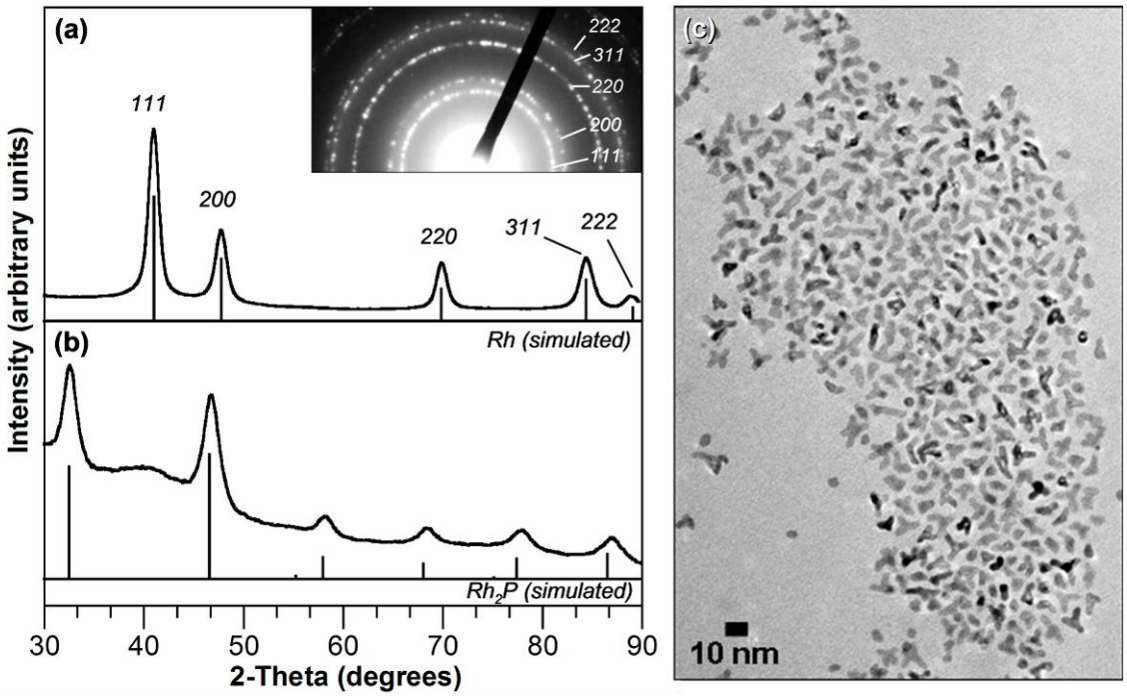

Figure 43. Powder XRD patterns for representative (a) Rh nanocrystal precursors (PDF card no. 5-0685) and (b) Rh_2P products (PDF card no. 77-0300). A representative SAED pattern for the Rh nanocrystal precursors is shown in the inset. A large area TEM image (c) shows a representative sample of Rh_2P multipods with shape-retention (formed from 41c).

Table 5. Shape percentages for Rh nanocrystals.

Sample	Shape	Percentage[a]
Rh Cubes	cubes/octahedra	53 %
	triangles	6 %
	spheres	40 %
	rods	1 %
Rh Triangles	etched triangles	10 %
	triangle derivatives	59 %
	spheres	22 %
	irregular	9 %
Rh Multipods (thin arms)	tetrapods	34 %
	tripods	30 %
	bent	15 %
	rods	5 %
	spheres	16 %
Rh Multipods (thick arms)	tetrapods	29 %
	tripods	24 %
	bent	19 %
	rods	11 %
	spheres	17 %

[a] Percentages are based on 150-400 particles for each sample. Aggregated particles were not included in statistics due to the difficulty of discerning faces and edges.

In a typical reaction to convert a metal nanocrystal to a metal phosphide, the metal nanocrystals are dispersed in TOP and injected into a hot, coordinating solvent, such as trioctylphosphine oxide (TOPO), under argon.[24-25] It is understood that colloidal metals can induce cleavage of the P-C bond in alkylphosphines creating a reactive phosphorus species,[76,85,87] although within the context of these TOP/metal nanoparticle reactions, byproducts have not yet been isolated and characterized. A similar reaction can be used to convert the Rh cubes/octahedra, triangles and multipods into Rh_2P, which is verified by XRD (Figure 43b). A small amount of nanocrystalline Rh is evident in the XRD pattern for Rh_2P, likely from some unreacted Rh (discussed later). Figure 43c shows a large area TEM image representative of Rh_2P multipods with shape-retention. As shown in Figure 44, cube-derived Rh nanocrystals (Figure 44a) form both solid and hollow single-crystal Rh_2P cubes (Figure 44b, ~ 50 % hollow). There is a substantial amount of shape conservation, with ~ 75 % of the cube-derived Rh nanocrystal precursors (cubes and octahedra) maintaining a cube-derived shape upon conversion to Rh_2P. Rh nanocube size seems to be largely responsible for generating hollow vs. dense nanocubes, which is consistent with previous observations of size-dependent hollowing for the conversion of spherical Ni nanocrystals to Ni_2P.[24] However, this is not absolute – a few hollow and dense nanocubes of the same size are sometimes found. In the case of Rh_2P, nanocubes larger than 7-8 nm tend to be hollow, while smaller ones tend to be dense. Similar to the cubes, triangle-shaped Rh nanocrystals (Figure 44c) convert to Rh_2P triangles (Figure 44d) by reaction with hot TOP. Although 40 % of the triangle-

derived Rh_2P nanostructures are hollow, they tend to have slightly rounded corners, and in some cases lose their triangular shape completely.

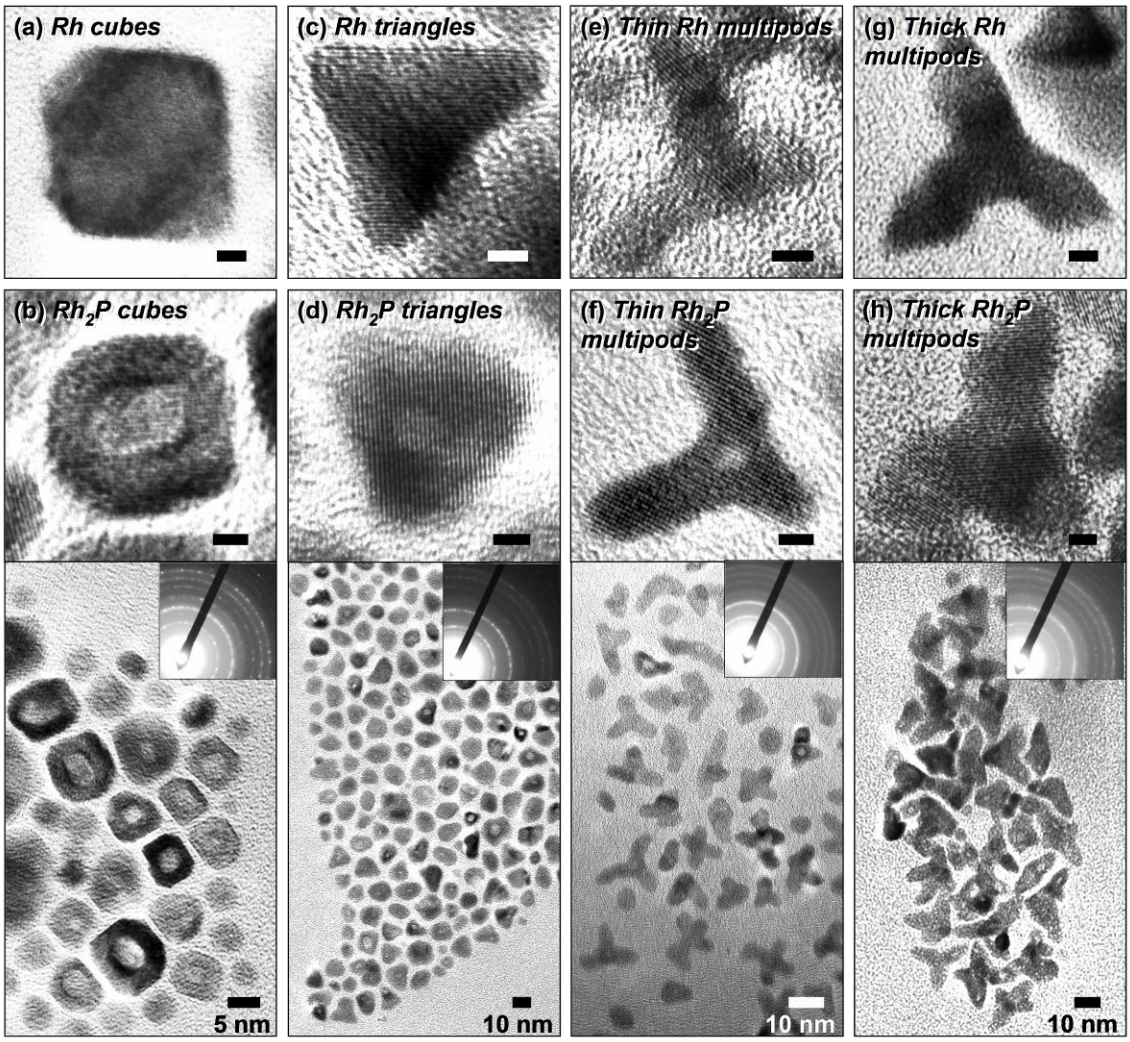

Figure 44. TEM images highlighting the shape-controlled conversion of Rh nanocrystal templates to Rh_2P: (a) Rh cube-derived nanocrystals and (b) Rh_2P formed from (a); (c) Rh triangle-derived nanocrystals and (d) Rh_2P triangles formed from (c); (e) thin-armed Rh multipods and (f) Rh_2P multipods formed from (e); and (g) thick-armed Rh multipods and (h) Rh_2P multipods formed from (g). Scale bars are 2 nm unless otherwise labeled.

Reaction of Rh multipods with TOP results in Rh_2P multipods with distinct morphological characteristics that are templated by the precursor nanocrystals (Figure 44e-h). For the long, thin-armed Rh multipod precursors (Figure 42c and 44e), the Rh_2P products (Figure 44f) maintain the shape of the Rh precursors, including many that show hollow cores, but not hollow arms. This is likely a size effect, since the arms are narrower than the core. Loss of multipod arms was often observed in the Rh_2P products, presumably due to the harsh conditions of the conversion reaction and the fragility of the multipod arms. In contrast to the Rh_2P multipods with long, thin arms, the multipods with thicker arms (Figure 44g) were hollow only in the arms and not the core (Figure 44h). In this case, the arms are more accessible and the cores are hindered by the bulky arms, so diffusion of P into the Rh arms is likely to occur more readily.

Figure 45 shows representative examples of the types of Rh_2P nanocrystals that can be generated via reaction of Rh nanocrystals with TOP, including the range of branched Rh_2P nanocrystals that are observed (monopods, bipods, tripods, and tetrapods). Rh_2P cubes, triangles, and multipods are accessible as both hollow and dense nanocrystals. Generally the ability to access hollow vs. dense nanostructures is related to the size of the precursor nanocrystals, as well as temperature. Both of these factors influence diffusion, which is responsible for the formation of Kirkendall-mediated voids.[43] It is important to note that our Rh nanocrystal precursors are of similar quality (size, uniformity, shape purity) to those reported in the literature (Table 5).[93,129-131] For example, our ability to generate Rh multipod samples containing mixtures of tripods and tetrapods, as well as bent, linear, and spherical nanostructures, mimics literature reports

using similar procedures.[93,129-131] In general, the relative populations of each of the morphologies in the final Rh_2P products are close to those in the Rh precursors as discussed earlier, with some additional degradation caused by the reaction with TOP. If one could synthesize Rh nanocrystal samples with better monodispersity and shape purity than is currently achievable using available literature methods, it is likely that shape-pure samples of Rh_2P nanocrystals could be generated, as well as samples that are entirely hollow or dense.

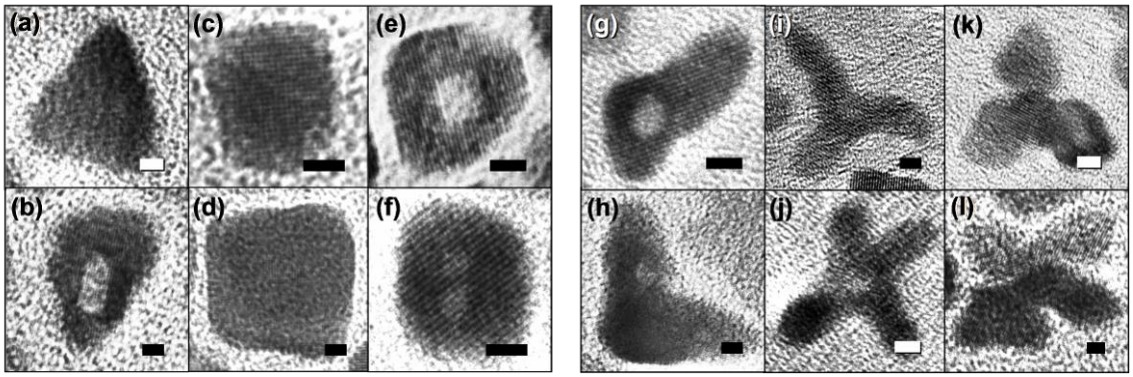

Figure 45. Representative Rh_2P nanostructures obtainable by reaction of Rh nanocrystals with TOP: (a) solid triangle, (b) hollow triangle, (c-d) solid cubes, (e-f) hollow cubes, (g-h) fractured multipods, (i-j) multipods with hollow cores, and (k-l) multipods with hollow arms. All scale bars are 2 nm.

For fcc metals such as Rh, it is known that the (111) planes have the lowest surface energy, followed by (100) and (110).[134] The relationship between surface energy and the shape of Rh nanocrystals has been discussed in depth in the literature.[93,129,134] In general, shapes that deviate from the thermodynamically favored truncated octahedron geometry are kinetically controlled and accessible because of the presence of surface

stabilizers or the use of seeded growth strategies. To our knowledge, the relative surface energies for Rh_2P are not known. However, the formation of Rh_2P nanocrystals with a variety of different nanocrystal morphologies, and therefore different exposed crystal planes, implies that at least some are kinetically controlled. This, in turn, implies that these same surface stabilizers (which remain present throughout the conversion from Rh to Rh_2P) similarly stabilize the Rh_2P surfaces. This is reasonable considering the diffusion-based reaction of P (from TOP) with the Rh nanocrystals and the relationship between the crystal structures of Rh and Rh_2P (Figure 46),[135] which likely minimizes major morphological changes. However, truncated edges and corners are frequently observed in the Rh_2P nanocrystals. For example, the Rh_2P hollow cubes show lattice spacings corresponding to the (200) planes and frequently show truncated corners corresponding to the (111) planes. This suggests competition between the relative stabilities of the Rh_2P planes and those of the precursor Rh nanocrystals.

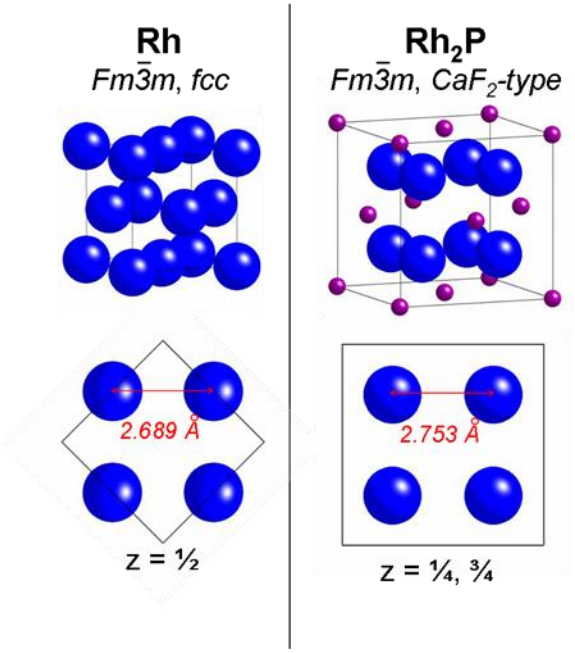

Figure 46. Unit cell models of Rh and Rh_2P. Blue and purple spheres represent Rh and P atoms, respectively.

In order to guarantee the shape-controlled conversion of the Rh nanocrystals to Rh_2P, there are a few crucial issues that need to be addressed. In contrast to previous reports of metal-to-metal phosphide conversion reactions that use hexadecylamine- or oleylamine-stabilized metal nanocrystals[20,24-25] that are soluble in TOP, the PVP-stabilized particles are immiscible with TOP. Since PVP is responsible for controlling the shape of the Rh nanocrystals,[118] stabilizing ligands that show good miscibility with TOP (such as amines or other ligands and surfactants) are not easily substituted for PVP. However, the PVP coating the nanocrystal surface, which defines its solubility, can be coated with co-solvents that help to bridge the miscibility gap between PVP and TOP. This effectively increases the ability to disperse the Rh nanocrystals in TOP, and also

minimizes degradation of the nanocrystal shape during the conversion reaction. Ethanol, oleic acid, oleylamine, and octyl ether are potential co-solvent candidates because they demonstrate sufficient miscibility with TOP, and PVP-coated nanocrystals are somewhat dispersible in them (Table 6 and 7).

Table 6. Degree of miscibility of various stabilizers with TOP.

Solvent/stabilizer	Degree of miscibility with TOP
Ethylene glycol	immiscible; forms two distinct layers
Ethanol	moderately miscible; slightly turbid solution
Oleic acid	miscible; visibly homogeneous
Oleylamine	miscible; visibly homogeneous
Octyl ether	miscible; visibly homogeneous
PVP	negligible after excessive sonication[a]

[a] Extent of dispersability of PVP in TOP with sonication as compared to other solvents (water, ethylene glycol, octyl ether)

Table 7. Dispersability of PVP-stabilized Rh multipods in various solvents.

Solvent/stabilizer	Extent of Rh dispersability (PVP-stabilized multipods)
Ethylene glycol	highly dispersable with lengthy sonication; visibly homogeneous
TOP	not dispersable
Ethanol	highly dispersable with minimal sonication; visibly homogeneous
Oleic acid	highly dispersable with minimal sonication; visibly homogeneous
Oleylamine	moderately dispersable with lengthy sonication
Octyl ether	minimally dispersable with lengthy sonication

Combinations of these co-solvents could also be used to fine-tune the particle/solvent interactions and possibly facilitate enhanced shape conservation via improved dispersion and shape retention. For example, adding oleic acid to the Rh-TOP solution creates a visibly homogeneous solution. However, as shown for the case of thin-arm Rh multipods dispersed with oleic acid in TOP, the resulting Rh_2P particles are largely spherical (Figure 47a). Specifically, 93 % of the Rh_2P products are spherical, compared to only 38 % when using optimal conditions (e.g. those used to generate the products shown in Figure 44f). In this case, the co-solvent aides miscibility, but destroys the anisotropic morphology. In contrast, using oleylamine, octyl ether and ethanol (and combinations of them) as co-solvents results in improved shape conservation in the Rh_2P product (Figure 47b-f), as detailed in Table 8. Despite this, a truly homogeneous solution of the PVP-stabilized particles and TOP can not be obtained, but the conversion reaction can still proceed with reasonably good morphology retention. Table 8 summarizes the ability of various combinations of co-solvents to facilitate the shape-controlled conversion of Rh nanocrystals into Rh_2P via reaction with TOP, as shown in the TEM micrographs in Figure 47. In general, the highest-quality Rh_2P nanocrystals are generated using solvent mixtures that include oleylamine and TOP and temperatures that are on the lower end of those used in nanocrystal/TOP reactions (~ 340 ºC).

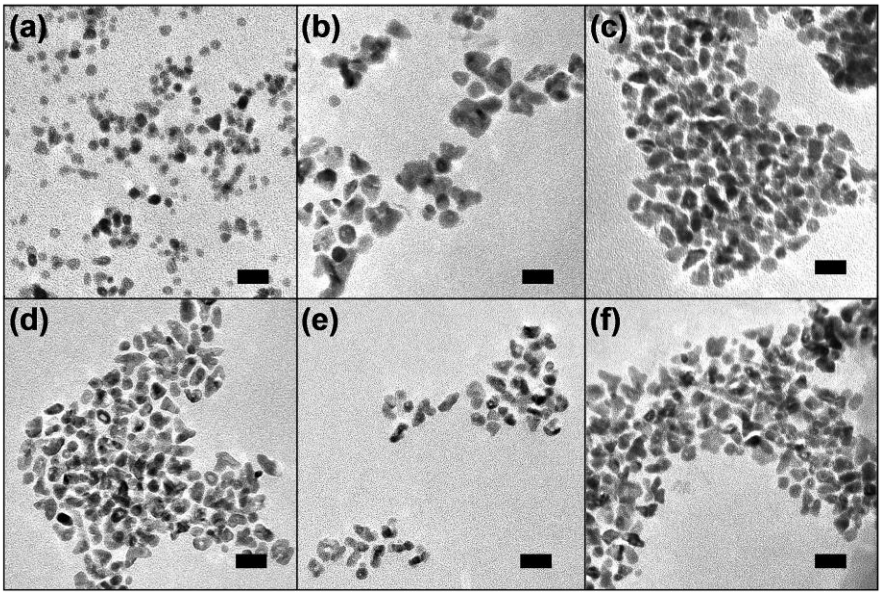

Figure 47. Rh_2P multipods made with various co-solvents, injected and aged for 1 h at 360 °C unless otherwise noted: (a) oleic acid, (b) octyl ether, (c) oleylamine, (d) ethanol + oleylamine (aged 15 min), (e) ethanol, and (f) ethanol (aged at 340 °C). All scale bars are 20 nm.

Table 8. Effects of co-solvents on the quality of Rh_2P multipods.

Co-solvent combination	Extent of Rh dispersability (PVP-stabilized multipods)[a]	Morphological retention of Rh_2P[b]
Ethanol[c] + TOP	heterogeneous solution (emulsion), visible particulates	49 % (360 °C), 60 % (340 °C)
Oleic acid + TOP	homogeneous solution	7 %
Oleylamine + TOP	heterogeneous solution (emulsion), visible particulates	55 % (360 °C), 72 % (340 °C)
Octyl ether + TOP	heterogeneous solution, large aggregated particulates	15 %
Ethanol + octyl ether + TOP	heterogeneous solution, visible particulates	48 %
Ethanol + oleylamine + TOP	slightly turbid, no visible particulates	28 % (360 °C), 62 % (340 °C)

[a] Dispersability of PVP-stabilized Rh multipods is related to the solubility of PVP in the given solvents.

[b] Morphological retention is based on the percentage of Rh_2P particles retaining their original multipod (tetrapod or tripod) shape: % multipods for Rh_2P product / % multipods in Rh precursor. 150-400 particles were categorized for each sample, depending on image quality. No aggregated particles were included since edges and faces could not be clearly discerned. Data is given for conversion reaction aged at 360 °C for 1 h unless otherwise noted.

[c] Ethanol is presumed to vaporize instantly upon injection at the high reaction temperatures.

As is evident from the observations included in Table 8, temperature also plays a key role in optimizing shape retention and product purity, as well as the ability to generate hollow nanostructures. When Rh nanocrystals dispersed in TOP are injected at 360 °C and aged at that temperature for 1 h, phase-pure Rh_2P (by powder XRD, not shown) is always obtained, and the product usually has a high percentage of hollow particles, regardless of morphology. However, the high reaction temperature can result in Rh_2P nanocrystals that have lost their original shape and are highly aggregated. When the injection temperature is 360 °C but the aging temperature is lowered to 330-340 °C, a higher degree of shape conservation is observed, though there are considerably fewer

hollow particles. For example, when oleylamine is used as a co-solvent, there is a significant improvement in Rh_2P shape quality if the reaction is aged at 340 °C (Figure 44h, 62 % shape retention) vs. 360 °C (Figure 47c, 28 % shape retention). However, the improved shape quality is at the cost of product purity. At lower temperatures, the Rh_2P products retain their shape reasonably well, but some unreacted Rh remains, as seen by powder XRD (Figure 43b) and EDS (not shown, ~ 5-10 % increase in Rh content relative to P compared to product aged at 360 °C) . These observations imply that higher aging temperatures facilitate complete conversion of Rh to Rh_2P, show less ability to retain the shape of the Rh precursors (spherical shapes are preferred), and favor hollow nanostructures. Likewise, lower aging temperatures (330-340 °C) tend to result in incomplete conversion (e.g. Rh impurities remain), maintain the shape of the Rh precursors, and generate dense nanostructures. Consistent with this, the optimal reaction conditions for maintaining the regular multipod shape (Figure 44h) while maximizing conversion efficiency are to inject the Rh-TOP solution at 360 °C and age at 340 °C for 1 h. The window of optimal conditions for generating the highest-quality Rh_2P nanocrystals is narrow but achievable, and points to the critical roles that the key synthetic variables have on ensuring shape-controlled conversion of a metal nanocrystal into a metal phosphide.

Conclusions

In this chapter, we described the shape-controlled conversion of a diverse library of Rh nanocrystal shapes into dense and hollow Rh_2P nanocrystals, which represents the most morphologically-diverse set of metal phosphide nanocrystals reported to date. Our studies also provide insights into shape-controlled nanocrystal conversion reactions that are likely to be applicable to other phosphide and multi-element nanocrystal systems. This is important because it is rapidly becoming straightforward to control the quality, shape, and uniformity of single metal nanocrystals,[118-119] but similar achievements (and general synthetic strategies) for multi-metal nanostructures are less common. Employing, understanding, and optimizing template-based strategies provides an alternative mechanism for increasing the complexity of solid-state materials that are accessible as well-controlled nanocrystals.

CHAPTER VII

SUMMARY AND CONCLUSIONS

In chapters II and III, variations of the nanocomposite route were developed for the synthesis of multimetal oxides and metal borates. When using this strategy to form metal oxides, binary metal oxides nanoparticles were mixed in specific ratios in solution to form nano-mixed aggregates[21] in analogy to previous work by the Schaak group.[4-5] Once isolated, dried powdered nanocomposites could be annealed to form target ternary oxides.[21] A noteworthy variation in protocol used for forming oxides was that oftentimes oxide precursors could be used as nanoparticle reactants. For example, in many cases amorphous oxide nanoparticles can be used as reactants to form nanocomposites, as well as many metal hydroxide phases. Even if the particles which form the nanocomposite do not contain the exact stoichiometric ratio of metals to oxygen of the target compound, annealing the composites in air makes it possible to obtain the target ternary oxide phase. However, it is of critical importance that the ratio of metals in the composite be the same as the target compound.

To make metal borates using a strategy related to the nanocomposite approach, sodium borohydride was used as a boron source. When reacted with lanthanides and actinides in solution, BH_4^- has been known to form extended polymeric networks.[63] In the case of the reaction with RE^{3+} with $NaBH_4$ in aqueous solution, a translucent gel rapidly precipitates and appears amorphous via powder XRD when it is dehydrated. It is hypothesized that the nanocomposite in this case is an extended network of RE^{3+} and

boron species (including BH_4^-). The dried composite can be annealed in air at 700 °C to form orthoborate *RE*BO_3, where *RE* can be Y, Nd, Sm, Eu, Gd, or Ho. Orthoborates can have nonlinear optical properties, making them useful as phosphors in plasma displays and as laser up-converters.[22] For example, we prepared $Y_{0.9}BO_3$:$Eu_{0.1}$ using this strategy, which emits in the red-orange region under incident UV light. While there are inherently many grain boundaries within the borate materials produced using this method (which can inhibit its performance in technological applications), the simplicity of the reaction could make it attractive for the on-support synthesis of metal borates.

Furthermore, the oxide and borate variations of the nanocomposite strategy can be coupled to form nanocomposite precursors to more complex materials. For example, Al_2O_3 nanoparticle precursors can be formed *in situ* with *RE*-B nanoparticles to form a multimetal precursor which can be annealed to form huntite-type borates *RE*$Al_3(BO_3)_4$. Huntite-type borates can have frequency self-doubling properties.[23] Coupling borates with oxides via the nanocomposite transformation approach is an example of one of many ways this simple strategy could be used to form complex materials.

In chapters IV, V and VI, a generalized strategy was developed for transforming metals into metal phosphides using metal nanocrystals as well as bulk and nanostructured metals as precursors. It has been known in catalysis that colloidal metals can catalyze cleavage of the P-C bond in alkylphosphines.[85] Taken in context with the speculations of other groups[127] and the isolation and observation of a metal nanocrystal intermediate in the direct reaction of $Pd(acac)_2$ with TOP in chapter IV, we hypothesize that many zero-valent late transition metals zero can cleave the P-C bond in TOP at

temperatures above 300 °C, forming a reactive phosphorus species which can diffuse into the parent nanocrystal to form metal phosphides. This reaction is significant for two key reasons. Most importantly, work by our group and others[20,70,77-78,80] serves to reiterate that at elevated temperatures TOP can be highly reactive, and its ability to readily react with metals should be considered when used in nanocrystal synthesis. Secondly, the evidence that TOP can be a mild phosphorus source and used in simple, bench-top reactions to form phosphides opens a door to a new synthetic strategy which can be broadly applied to many late and post-transition metal phosphides and potentially to phosphide derivative materials.

Chapter IV highlights the generality of this conversion strategy, which we have expanded to many late transition metal phosphide systems, including 4d and 5d transition metal phosphides—many of which have never been made as unsupported nanocrystals using other methods.[24-25] Additionally, we have seen in some systems that more than one metal phosphide phase can be accessed simply by varying the reaction temperature. As a general trend, higher reaction temperatures promote higher phosphorus content in the product. We believe this occurs because the higher reaction temperatures cause faster decomposition of TOP and thus there is a greater concentration of free phosphorus available to diffuse into the parent metal nanocrystal.

Another key observation in chapter IV, which was rigorously studied in chapter VI, was the notion of templating the size and shape of metal phosphide nanocrystals based on the size and shape of their metal precursors. For example, a size effect was observed in the Ni_2P system in which small spherical Ni nanocrystals formed Ni_2P

nanocrystals that retained the size of their precursors when reacted with TOP at 300 °C.[14] In contrast, when larger Ni nanocrystals were used as precursors under identical reaction conditions, hollow Ni_2P spheres formed via Kirkendall effects that were roughly twice the diameter of the precursor Ni nanocrystals.[24] The observation of hollow particles hints at a size effect on reaction rate in this type of conversion reaction. Furthermore, in chapter VI the correlation between the size and shape of metal precursors and the size, shape and presence of hollowing in metal phosphide products was rigorously investigated in a case study of Rh_2P.[26] Rh nanocrystals with distinct cube-like, triangle-like or multipod morphologies were converted to Rh_2P nanocrystals that could retain the original shape of their precursors under the appropriate reaction conditions. Variables such as reaction temperature, the use of stabilizing ligands with appropriate solubility in reaction solvents, and the presence of specific co-solvents to promote homogeneous mixing of the reactants play important roles in the ability to retain precursor shape, to promote hollowing of the products, and to obtain optimal phase purity of Rh_2P.[26] The shape-retention insights gained from the case study of the conversion of Rh to Rh_2P could be broadly applied to other metal phosphide systems and potentially to other classes of materials.

In addition to the conversion of metal nanocrystals to phosphides, chapter V highlights the diversity of metal reactants which can be used as precursors. In analogy to discrete nanocrystals, bulk- and micron-scale metal powders can be converted to metal phosphides under nearly identical conditions as their nanocrystal counterparts.[25] In many cases, a diminished reactivity is observed in which mixed-phase products or

metallic impurities are present that could be attributed to a larger particle size hindering complete diffusion of phosphorus into the parent metal structure. Additionally, metal phosphide coatings can be formed on bulk-scale wires, foils and metal chunks when reacted with TOP in solution.[25] Furthermore, nanostructured metals such as supported metal nanocrystals, thin films, and patterned substrates can be transformed to metal phosphides using the same solution-based conversion strategy.[25] The ability to adapt the phosphide conversion strategy to diverse metal precursors hints at its potential applicability for materials processing.

Taken together, chapters IV, V, and VI form an important body of work that has served to drastically increase the variety of metal phosphide nanocrystals that can be made using bench-top, solution based techniques. Equally important, the correlation between size, shape and micro-/nano-structure of the metal precursors used and the metal phosphide products formed hints at the potential for using this strategy to rationally design complex metal phosphide architectures with controllable stoichiometry, size and shape. Furthermore, the rigorous establishment of reactivity of various metals to form phosphides can be used as part of a growing set of fundamental reactions that could serve as a "tool box" of transformation reactions used to broadly integrate the synthesis of various classes of materials.

REFERENCES

(1) West, A. R. *Basic Solid State Chemistry*, 2nd Edition; Wiley: West Sussex, 1999.

(2) Haber, J.; Gunda, N. V.; Balbach, J. J.; Conrado, M. S.; Bhuro, W. E. *Chem. Mater*. **2000**, *12*, 973-982.

(3) Schlecht, S.; Erk, C.; Yosef, M. *Inorg. Chem*. **2006**, *45*, 1693-1697.

(4) Sra, A. K.; Schaak, R. E. *J. Am. Chem. Soc*. **2004**, *126*, 6667-6672.

(5) Schaak, R. E.; Sra, A. K.; Leonard, B. M.; Cable, R. E.; Bauer, J. C.; Han, Y.-F.; Means, J.; Teizer, W.; Vasquez, Y.; Funck, E. S. *J. Am. Chem. Soc.* **2005**, *127*, 3506-3515.

(6) Bauer, J. C.; Chen, X.; Liu, Q.; Phan, T.-H.; Schaak, R. E. *J. Mater. Chem.* **2008**, *18*, 275-282.

(7) Chou, N. H.; Schaak, R. E. *J. Am. Chem. Soc*. **2007**, *129*, 7339-7345.

(8) Cable, R. E.; Schaak, R. E. *J. Am. Chem. Soc.* **2006**, *128*, 9588-9589.

(9) (a) Leonard, B. M.; Bhuvanesh, N. S. P.; Schaak, R. E. *J. Am. Chem. Soc*. **2005**, *127*, 7326-7327. (b) Leonard, B. M.; Schaak, R. E. *J. Am. Chem. Soc*. **2006**, *128*, 11475-11482.

(10) Cable, R. E.; Schaak, R. E. *Chem. Mater*, **2007**, *19*, 4098-4104.

(11) Viau, G.; Fiévet-Vincent, F.; Fiévet, F. *J. Mater. Chem.* **1996**, *6*, 1047–1053

(12) Yin, Y.; Rioux, R. M.; Erdonmez, C. K.; Hughes, S.; Somorajai, G. A.; Alivisatos, A. P. *Science* **2004**, *304*, 711-714.

(13) Yin, Y.; Erdonmez, C. K.; Cabot, A.; Hughes, S.; Alivisatos, A. P. *Adv. Funct. Mater.* **2006**, *16*, 1389-1399.

(14) Gates, B.; Mayers, B.; Wu. Y.; Sun, Y.; Cattle, B.; Yang, P.; Xia, Y. *Adv. Funct. Mater*. **2002**, *12*, 679-686.

(15) Woo, K.; Hong, J.; Choi, S.; Lee, H.-W.; Ahn, J.-P.; Kim, C. S.; Lee, S. W. *Chem. Mater*. **2004**, *16*, 2814-2818.

(16) Son, S. U.; Park, I. K.; Park, J.; Hyeon, T. *Chem. Commun*. **2004**, 778-779.

(17) Yin, M.; Wu, C.-K.; Lou, Y.; Burda, C.; Koberstein, J. T.; Zhu, Y.; O'Brien, S. *J. Am. Chem. Soc*. **2005**, *127*, 9506-9511.

(18) Khanna, P. K.; Jun, K.-W.; Hong, K. B.; Baeg, J.-O.; Mehrotra, G. K. *Mater. Chem. Phys.* **2005**, *92*, 54-58.

(19) Singh, N.; Khanna, P. K. *Synth. React. Inorg. Me.* **2007**, *37*, 367-371.

(20) Chiang, R.-K.; Chiang, R.-T. *Inorg. Chem*. **2007**, *46*, 369-371.

(21) Henkes, A. E.; Bauer, J. C.; Sra, A. K.; Johnson, R. D.; Cable, R. E.; Schaak, R. E. *Chem. Mater*. **2006**, *18*, 567-571.

(22) Jiang, X.-C.; Yan, C.-H.; Sun, L.-D.; Wei, Z.-G.; Liao, C.-S. *J. Solid State Chem.* **2003**, *175*, 245-251.

(23) Jaque, D.; Enguita, O.; Luo, Z. D.; Garcia Sole, J.; Caldino G., U. *Opt. Mater.* **2004**, *25*, 9-15.

(24) Henkes, A. E.; Vasquez, Y.; Schaak, R. E. *J. Am. Chem. Soc.* **2007**, *129*, 1896-1897.

(25) Henkes, A. E.; Schaak, R. E. *Chem. Mater*. **2007**, *19*, 4234-4242.

(26) Henkes, A. E.; Schaak, R. E. *Inorg. Chem.* **2008**, *47*, 671-677.

(27) Salamon, M. B.; Jaime, M. *Rev. Mod. Phys.* **2001**, *73*, 583-628.

(28) Cava, R. J. *J. Am. Ceram. Soc.* **2000**, *83*, 5-28.

(29) Nanamatsum S.; Kimura, M.; Doi, K.; Matsushita, S.; Yamada, N. *Ferroelectrics* **1974**, *8*, 511-513.

(30) Halasyamani, P. S.; Poeppelmeier, K. R. *Chem. Mater.* **1998**, *10*, 2753-2769.

(31) Boivin, J. C.; Mairesse, G. *Chem. Mater.* **1998**, *10*, 2870-2888.

(32) Pena, M. A.; Fierro, J. L. G. *Chem. Rev.* **2001**, *101*, 1981-2017.

(33) Rao, C. N. R.; Gopalakrishnan, J. *New Directions in Solid State Chemistry*; Cambridge University Press: Cambridge, 1989.

(34) Feng, S.; Xu, R. *Acc. Chem. Res.* **2001**, *34*, 239.

(35) (a) Schaak, R. E.; Mallouk, T. E. *J. Am. Chem. Soc.* **2000**, *122*, 2798-2803. (b) Schaak, R. E.; Mallouk, T. E. *Chem. Mater.* **2002**, *14*, 1455-1471.

(36) Wright, J. D.; Sommerdijk, A. J. M. *Sol-gel Materials: Chemistry and Applications*; Gordon and Breach: Amsterdam, 2001.

(37) Cushing, B. L.; Kolesnichenko, V. L.; O'Connor, C. J. *Chem. Rev.* **2004**, *104*, 3893-3946.

(38) (a) Bhuvanesh, N. S. P.; Reibenspies, J. H. *J. Appl. Crystallogr.* **2003**, *36*, 1480-1481. (b) Bhuvanesh, N. S. P.; Reibenspies, J. H.; Zhang, Y.; Lee, P. L. *J. Appl. Crystallogr.* **2005**, *38*, 632-638.

(39) (a) Feldmann, C.; Jungk, H.-O. *Angew. Chem., Int. Ed.* **2001**, *40*, 359-362. (b) Li, X.; Gao, H.; Murphy, C. J.; Gou, L. *Nano Lett.* **2004**, *4*, 1903-1907. (c) Stewart, S. J.; Multigner, M.; Marco, J. F.; Berry, F. J.; Hernando, A.; Gonzalez, J. M. *Solid State Commun.* **2004**, *130*, 247-251. (d) Wang, Z.; Chen, X.; Liu, J.; Mo, M.; Yang, L.; Qian, Y. *Solid State Commun.* **2004**, *130*, 585-589. (e) Yin, M.; Wu, C.-K.; Lou, Y.; Burda, C.; Koberstein, J. T.; Zhu, Y.; O'Brien, S. *J. Am. Chem. Soc.* **2005**, *127*, 9506-9511.

(40) Yin, M.; Wu, C.-K.; Lou, Y.; Burda, C.; Koberstein, J. T.; Zhu, Y.; O'Brien, S. *J. Am.Chem. Soc*. **2005**, *127*, 9506-9511.

(41) Papoutsi, D.; Lianos, P.; Yianoulis, P.; Koutsoukos, P. *Langmuir* **1994**, *10*, 1684-1689.

(42) Snyder, J.; Slusky, J. S.; Cava, R. J.; Schiffer, P. *Nature* **2001**, *413*, 48-51.

(43) Heremans, C.; Wuensch, B. J.; Stalick, J. K.; Prince, E. *J. Solid State Chem.* **1995**, *117*, 108-121.

(44) (a) Wang, S. X.; Wang, L. M.; Ewing, R. C.; Govindan Kutty, K. V. *Nucl. Instrum. Methods B* **2000**, *169*, 135-140. (b) Hayward, M. A. *Chem. Mater.* **2005**, *17*, 670-675.

(45) Fuentes, A. F.; Boulahya, K.; Maczka, M.; Hanuza, J.; Amador, U. *Solid State Sci*. **2005**, *7*, 343-353.

(46) Kakihana, M.; Milanova, M. M.; Arima, M.; Okubo, T.; Yashima, M.; Yoshimura, M. *J. Am. Ceram. Soc*. **1996**, *79*, 1673-1676.

(47) (a) Langlet, M.; Jenouvrier, P.; Rimet, R.; Fick, J. *Opt. Mater.* **2004**, *25*, 141-147. (b) Jenouvrier, P.; Boccardi, G.; Fick, J.; Jurdyc, A.-M.; Langlet, M. *J. Lumin.* **2005**, *113*, 291-300.

(48) Lerch, M.; Boysen, H.; Neder, R.; Frey, F.; Laqua, W. *J. Phys. Chem. Solids* **1992**, *53*, 1153-1156.

(49) Taylor, D. J.; Fleig, P. F.; Page, R. A. *Thin Solid Films* **2002**, *408*, 104-110.

(50) (a) Singh, R. S.; Bhimasankaram, T.; Kumar, G. S.; Suryanarayana, S. V. *Solid State Commun.* **1994**, *91*, 567-569. (b) Srinivas, A.; Suryanarayana, S. V.; Kumar, G. S.; Kumar, M. M. *J. Phys. Condens. Matter* **1999**, *11*, 3335-3340. (c) Srinivas, A.; Kim, D.-W.; Hong, K. S.; Suryanarayana, S. V. *Mater. Res. Bull.* **2004**, *39*, 55-61.

(51) (a) Shimode, M,; Sasaki, M.; Mukaida, K. *J. Solid State Chem.* **2000**, *151*, 16-20. (b) Park, S.; Keszler, D. A. *J. Solid State Chem.* **2003**, *173*, 355-358.

(52) Becker, P. *Adv. Mater*. **1998**, *10*, 979-992.

(53) Baudrier-Raybaut, M.; Haïdar, R.; Kupecek, P.; Lemasson, P.; Rosencher, E. *Nature* **2004**, *432*, 374-376.

(54) Wei, Z.; Sun, L.; Liao, C.; Yan, C.; Huang, S. *Appl. Phys. Lett*. **2002**, *80*, 1447-1449.

(55) Chadeyron, G.; Mahiou, R.; El-Ghozzi, M.; Arbus, A.; Zambon, D.; Cousseins, J. C. *J. Lumin*. **1997**, *72*, 564-566.

(56) Kim, T.; Kang, S. *Mater. Res. Bull*. **2005**, *40*, 1945-1954.

(57) Jiang, X.-C.; Sun, L.-D.; Yan, C.-H. *J. Phys. Chem. B* **2004**, *108*, 3387-3390.

(58) Wang, F.; Fan, X.; Pi, D.; Wang, M. *J. Solid State Chem*. **2004**, *177*, 3346-3350.

(59) Li, Z.; Zeng, J.; Li, Y. *Small* **2007**, *3*, 438-443.

(60) (a) Kim, D. S.; Lee, R. Y. *J. Mater. Sci*. **2000**, *35*, 4777-4782. (b) Kim, K. N.; Jung, H. K.; Park, H. D.; Kim, D. *J. Mater. Res*. **2002**, *17*, 907-910.

(61) Wei, Z. G.; Sun, L. D.; Liao, C. H.; Jiang, X. C.; Yan, C. H. *J. Mater. Chem.*. **2002**, *12*, 3665-3670.

(62) Boyer, D.; Bertrand, G.; Mahiou, R. *J. Lumin*. **2003**, *104*, 229-237.

(63) Marks, T. J.; Kolb, J. R. *Chem. Rev*. **1977**, *77*, 263-293.

(64) Cotton, F. A.; Wilkinson, G., *Advanced Inorganic Chemistry*; John Wiley and Sons: New York, 1988.

(65) Brown, N. M. D.; Bladon, P. *J. Chem. Soc. (A)* **1969**, 526-532.

(66) Lemanceau, S.; Bertrand-Chadeyron, G.; Mahiou, R.; El-Ghozzi, M.; Cousseins, J. C.; Conflant, P.; Vannier, R. N. *J. Solid State Chem*. **1999**, *148*, 229-235.

(67) Wei, Z.-G.; Sun, L.-D.; Jiang, X.-C.; Liao, C.-S.; Yan, C.-H.; Tao, Y.; Zhang, J.; Hu, T.-D.; Xie, Y.-N. *Chem. Mater*. **2003**, *15*, 3011-3017.

(68) Brenier, A.; Tu, C.; Zhu, Z.; Li, J.; Wu, B. *J. Appl. Phys.* **2005**, *97*, 013503.

(69) Brock, S. L.; Perera, S. C.; Stamm, K. L. *Chem. Eur. J*. **2004**, *10*, 3364-3371.

(70) Gregg, K. A.; Perera, S. C.; Lawes, G.; Shinozaki, S.; Brock, S. L. *Chem. Mater*. **2006**, *18*, 879-886.

(71) Perera, S. C.; Tsoi, G.; Weneger, L. E.; Brock, S. L. *J. Am. Chem. Soc.* **2003**, *125*, 13960-13961.

(72) Xie, Y.; Su, H. L.; Qian, X. F.; Liu, X. M.; Qian, Y. T. *J. Solid State Chem*. **2000**, *149*, 88-91.

(73) Lukehart, C. M.; Milne, S. B.; Stock, S. R. *Chem. Mater*. **1998**, *10*, 903-908.

(74) Stamm, K. L.; Garno, J. C.; Liu, G.; Brock, S. L. *J. Am. Chem. Soc.* **2003**, *125*, 4038-4039.

(75) Perera, S. C.; Fodor, P. S.; Tsoi, G. M.; Wenger, L. E.; Brock, S. L. *Chem. Mater*. **2003**, *15*, 4034-4038.

(76) Chen J.-H.; Taie, M.-F.; Chi, K.-M. *J. Mater. Chem*. **2004**, *14*, 296-298.

(77) Li, Y.; Malik, M. A.; O'Brien, P. *J. Am. Chem. Soc*. **2005**, *127*, 16020-16021.

(78) Park, J.; Koo, B.; Yoon, K. Y.; Hwang, Y.; Kang, M.; Park, J.-G.; Hyeon, T. *J. Am. Chem. Soc*. **2005**, *127*, 8433-8440.

(79) Park, J.; Koo, B.; Hwang, Y.; Bae, C.; An, K.; Park, J.-G.; Park, H. M.; Hyeon, T. *Angew. Chem., Int. Ed*. **2004**, *43*, 2282-2285.

(80) Qian, C.; Kim, F.; Ma, L.; Tsui, F.; Yang, P.; Liu, J. *J. Am. Chem. Soc*. **2004**, *126*, 1195-1198.

(81) (a) Son, S. U.; Jang, Y.; Yoon, K. Y.; Kang, E.; Hyeon, T. *Nano Lett*. **2004**, *4*, 1147-1151. (b) Kim, S.-W.; Park, J.; Jank, Y.; Chung, Y.; Hwang, S.; Hyeon, T.; Kim, Y. W. *Nano. Lett*. **2003**, *3*, 1289-1291.

(82) Park, J.; Kang, E.; Son, S. U.; Park, H. M.; Lee, M. K.; Kim, J.; Kim, K. W.; Noh, H.-J.; Park, J.-H.; Bae, C. J.; Park, J.-G.; Hyeon, T. *Adv. Mater.* **2005**, *17*, 429-434.

(83) Sra, A. K.; Ewers, T. D.; Xu, Q.; Zandbergen, H.; Schaak, R. E. *Chem. Commun*. **2006**, 750-752.

(84) Grebinski, J. W.; Richter, K. L.; Zhang, J.; Kosel, T. H.; Kuno, M. *J. Phys. Chem. B* **2004**, *108*, 9745-9751.

(85) Schmidt, F. K.; Belykh, L. B.; Cherenkova, T. V. *Kinet. Catal.* **2001**, *42*, 163-173.

(86) (a) von Schnering, H.-G.; Hönle, W. *Chem. Rev*. **1988**, *88*, 243-273. (b) Kanatzidis, M. G.; Pöttgen, R.; Jeitschko, W. *Angew. Chem. Int. Ed*. **2005**, *44*, 6996-7023.

(87) Su, H. L.; Xie, Y.; Li, B.; Liu, X. M.; Qian, Y. T. *Solid State Ionics* **1999**, *122*, 157-160.

(88) Aitken, J. A.; Ganzha-Hazen, B.; Brock, S. L. *J. Solid State Chem*. **2005**, *178*, 970-975.

(89) (a) Smigelskas, A. D.; Kirkendall, E. O. *Trans. AIME* **1947**, *171*, 130-142. (b) Fan, H.J.; Knez, M.; Scholz, R.; Hesse, D.; Nielsch, K.; Zacharias, M.; Gösele, U. *Nano Letters* **2007**, *7*, 993-997.

(90) Park, S.-J.; Kim, S.; Lee, S.; Khim, Z. G.; Char, K.; Hyeon, T. *J. Am. Chem. Soc.* **2000**, *122*, 8581-8582.

(91) Oyama, S. T. *J. Catal.* **2003**, *216*, 343-352.

(92) Murphy, C. J.; Gole, A. M.; Hunyadi, S. E.; Orendorff, C. J. *Inorg. Chem.* **2006**, *45*, 7544-7554.

(93) Zettsu, N.; McLellan, J. M.; Wiley, B.; Yin, Y.; Li, Z.-Y.; Xia, Y. *Angew. Chem. Int. Ed.* **2006**, *45*, 1288-1292.

(94) Raub, C. J.; Zachariasen, W. H.; Geballe, T. H.; Matthias, B. T. *J. Phys. Chem. Solids* **1963**, *24*, 1093-1100.

(95) DeLong, L. E.; Meisner, G. P. *Solid State Commun.* **1985**, *53*, 119-123.

(96) Tegus, O.; Brück, E.; Buschow, K. H. J.; de Boer, F. R. *Nature* **2002**, *415*, 150-152.

(97) Jiang, J.; Kauzlarich, S. M. *Chem. Mater.* **2006**, *18*, 435-441.

(98) Souza, D. C. S.; Pralong, V.; Jacobson, A. J.; Nazar, L. F. *Science* **2002**, *296*, 2012-2015.

(99) Bichat, M.-P.; Pascal, J.-L.; Gillot, F.; Favier, F. *Chem. Mater.* **2005**, *17*, 6761-6771.

(100) Mauvernay, B.; Doublet, M.-L.; Monconduit, L. *J. Phys. Chem. Solids* **2006**, *67*, 1252-1257.

(101) (a) Rundqvist, S. *Acta Chem. Scand.* **1961**, *15*, 451-453. (b) Zachariasen, W. H. *Acta Crystallogr.* **1963**, *16*, 1253-1255. (c) Gullman, L.-O. *J. Less-Common Met.* **1966**, *11*, 157-167.

(102) Kanatzidis, M. G.; Pöttgen, R.; Jeitschko, W. *Angew. Chem., Int. Ed.* **2005**, *44*, 6996-7023.

(103) Gu, Y.; Guo, F.; Qian, Y.; Zheng, H.; Yang, Z. *Mater. Res. Bull.* **2002**, *37*, 1101-1105.

(104) Kim, Y.-H.; Jun, Y.-W.; Jun, B.-H.; Lee, S.-M.; Cheon, J. *J. Am. Chem. Soc.* **2002**, *124*, 13656-13657.

(105) (a) Hermann, A. M.; Madan, A.; Wanlass, M. W.; Badri, V.; Ahrenkiel, R.; Morrison, S.; Gonzales, C. *Sol. Energy Mater. Sol. Cells* **2004**, *82*, 241-252. (b) Soliman, M.; Kashyout, A. B.; Osman, M.; El-Gamal, M. *Ren. Energy* **2005**, *30*, 1819-1829.

(106) Hygnstrom, S. E.; McDonald, P. M.; Virchow, P. M. *Int. Biodet. Biodeg.* **1998**, *42*, 147-152.

(107) Buhro, W. E. *Polyhedron* **1994**, *13*, 1131-1148.

(108) (a) Pawlinkowski, J. M. *Phys. Rev. B* **1982**, *26*, 4711-4713. (b) Bryja, L.; Jezierski, K.; Misiewicz, J. *Thin Solid Films* **1993**, *229*, 11-13.

(109) (a) Green, M.; O'Brien, B. *Chem. Mater.* **2001**, *13*, 4500-4505. (b) Weber, A.; Sutter, P.; von Känel, H. *J. Appl. Phys.* **1994**, *75*, 7448-7455.

(110) Yang, S.; Liang, C.; Prins, R. *J. Catal*. **2006**, *241*, 465-469.

(111) Yang, S.; Prins, R. *Chem. Commun*. **2005**, 4178-1480.

(112) Alivisatos, A. P. *Science* **1996**, *271*, 933-937.

(113) El-Sayed, M. A. *Acc. Chem. Res*. **2004**, *37*, 326-333.

(114) (a) Scher, E. K.; Manna, L.; Alivisatos, A. P. *Phil. Trans. R. Soc. Lond. A* **2003**, *361*, 241-257. (b) Burda, C.; Chen, X.; Narayanan, R.; El-Sayed, M. A. *Chem. Rev*. **2005**, *105*, 1025-1102.

(115) (a) Narayana, R.; El-Sayed, M. A. *Nano Letters* **2004**, *4*, 1343-1348. (b) Daniel, M.-C.; Astruc, D. *Chem. Rev*. **2004**, *104*, 293-346. (c) Tian, N.; Zhou, Z.-Y.; Sun, S.-G.; Ding, Y.; Wang, Z. L. *Science* **2007**, *316*, 732-735.

(116) (a) Chen, J.; Wiley, B.; Li, Z.-Y.; Campbell, D.; Saeki, F.; Cang, H.; Au, L.; Lee, J.; Li, X.; Xia, Y. *Adv. Mater*. **2005**, *17*, 2255-2261. (b) Eustis, S.; El-Sayed, M. A. *Chem. Soc. Rev*. **2006**, *35*, 209-217.

(117) (a) Li, L.-S.; Hu, J.; Yang, W.; Alivisatos, A. P. *Nano Letters* **2001**, *1*, 349-351. (b) Murphy, C. J.; Sau, T. K.; Gole, A. M.; Orendorff, C. J.; Gau, J.; Gou, L.; Hunyadi, S. E.; Li, T. *J. Phys. Chem. B* **2005**, *109*, 13857-13870. (c) Orendorff, C. J.; Gole, A.; Sau, T. K.; Murphy, C. *J. Anal. Chem*. **2005**, *77*, 3261-3266.

(118) (a) Wiley, B.; Sun, Y.; Mayers, B.; Xia, Y. *Chem. Eur. J.* **2005**, *11*, 454-463. (b) Kim, F.; Connor, S.; Song, H.; Kuykendall, T.; Yang, P. *Angew. Chem. Int. Ed.* **2004**, *43*, 3673-3677. (c) Sun, Y.; Xia, Y. *Science* **2002**, *298*, 2176-2179. (d) Xiong, Y.; McLellan, J. M.; Yin, Y.; Xia, Y. *Angew. Chem. Int. Ed*. **2007**, *46*, 790-794. (e) Washio, I.; Xiong, Y.; Yin, Y.; Xia, Y. *Adv. Mater*. **2006**, *18*, 1745-1749. (f) Wiley, B. J.; Xiong, Y.; Li, Z.-Y.; Yin, Y.; Xia, Y. *Nano Letters*, **2006**, *6*, 765-768. (g) Xiong, Y.; Washio, I.; Chen, J.; Cai, H.; Li, Z.-Y.; Xia, Y. *Langmuir* **2006**, *22*, 8563-8570. (h) Seo, D.; Park, J. C.; Song, H. *J. Am. Chem. Soc.* **2006**, *128*, 14863-14870.

(119) (a) Berhault, G.; Bausach, M.; Bisson, L.; Becerra, L.; Thomazeau, C.; Uzio, D. *J. Phys. Chem. C* **2007**, *111*, 5915-5925. (b) Sau, T. K.; Murphy, C. J. *J. Am. Chem. Soc*. **2004**, *126*, 8648-8649. (c) Chen, S.; Wang, Z. L.; Ballato, J.; Foulger, S. H.; Carroll, D. L. *J. Am. Chem. Soc*. **2003**, *125*, 16186-16187.

(120) (a) Lee, S.-M.; Cho, S.-N.; Cheon, *J. Adv. Mater.* **2003**, *15*, 441-444. (b) Peng, X. *Adv. Mater.* **2003**, *15*, 459-463. (c) Mana, L.; Scher, E. C.; Alivisatos, A. P. *J. Am. Chem. Soc*. **2000**, *122*, 12700-12706. (d) Chen, J.; McLellen, J. M.; Siekkinen, A.; Xiong, Y.; Li, Z.-Y.; Xia, Y. *J. Am. Chem. Soc*. **2006**, *128*, 14776-14777. (e) Maksimuk, S.; Yang, S.; Peng, Z; Yang, H. *J. Am. Chem. Soc*. **2007**, *129*, 8684-8685.

(121) (a) Jun, Y.-W.; Choi, J.-S.; Cheon, J. *Angew*. *Chem*. *Int*. *Ed*. **2006**, *45*, 3414-3439. (b) Park, J.; Joo, J.; Kwon, S.G.; Jang, Y.; Hyeon, T. *Angew*. *Chem*. *Int*. *Ed*. **2007**, *46*, 4630-4660. (c) Hyeon, T. *Chem*. *Commun*. **2003**, 927-934.

(122) Jun, Y,-W.; Lee, J.-H.; Choi, J.-S.; Cheon, J. *J. Phys. Chem. B* **2005**, *109*, 14795-14806.

(123) (a) Kurihara, L. K.; Chow, G. M.; Shoen, P. E. *Nanostruct. Mater.* **1995**, *5*, 607-613. (b) Green, M. *Chem. Commun*. **2005**, 3002-3011. (c) Wang, X.; Zhuang, J.; Peng, Q.; Li, Y. *Nature* **2005**, *437*, 121-124.

(124) Ng, C. H. B.; Fan, W. Y. *J. Phys. Chem. C* **2007**, *111*, 2953-2958.

(125) Tan, H.; Li, S.; Fan, W. Y. *J. Phys. Chem. B* **2006**, *110*, 15812-15816.

(126) (a) Sun, Y.; Wiley, B.; Li, Z.-H.; Xia, Y. *J. Am. Chem. Soc*. **2004**, *126*, 9399-9406. (b) Vasquez, Y.; Sra, A. K.; Schaak, R. E. *J. Am. Chem. Soc*. **2005**, *127*, 12504-12505.

(127) Chen, J.-H.; Tai, M.-F.; Chi, K.-M. *J. Mater. Chem*. **2004**, *3*, 296-298.

(128) Kelly, A. T.; Rusakova, I.; Ould-Ely, T.; Hofmann, C.; Lüttge, A.; Whitmire, K. H. *Nano Letters*, **2007**, *7*, 2920-2925.

(129) Hoefelmeyer, J. D.; Niesz, K.; Somorjai, G. A.; Tilley, T. D. *Nano Letters*, **2005**, *5*, 435-438.

(130) Humphrey, S. M.; Gras, M. E.; Habas, S. E.; Niesz, K.; Somorjai, G. A.; Tilley, T. D. *Nano Letters*, **2007**, *7*, 785-790.

(131) Park, K. H.; Jang, K.; Kim, H. J.; Son, S. U. *Angew. Chem. Int. Ed*. **2007**, *46*, 1152-1155.

(132) Song, H.; Kim, F.; Connor, S.; Somorjai, G. A.; Yang, P. *J. Phys. Chem. B* **2005**, *109*, 188-193.

(133) Boyanov, S.; Bernardi, J.; Gillot, F.; Dupont, L.; Womes, M.; Trascon, J.-M.; Monconduit, L.; Doublet, M.-L. *Chem*. *Mater*. **2006**, *18*, 3531-3538.

(134) (a) Wen, Y.-N.; Zhang, J.-M. *Solid State Commun*. **2007**, *144*, 163-167. (b) Zhang, J.-M.; Ma, F.; Xu, K.-W. *Appl. Surf. Sci*. **2004**, *229*, 34-42. (c) Vitos, L.; Ruban, A. V.; Skriver, H. L.; Kollár, J. *Surf. Sci*. **1998**, *411*, 186-202.

(135) (a) Ross, R. G.; Hume-Rothery, W. *J. Less-Common Met.* **1963**, *5*, 258-270. (b) Zumbusch, M. *Z. Anorg. Chem*. **1940**, *243*, 322-329. (c) Rundqvist, S. *Nature*, **1960**, *185*, 31-32. (d) Secoue, M.; Auvray, P.; Toudic, Y.; Ballini, Y. *J. Crystal Growth* **1986**, *76*, 135-141.

VITA

Amanda Erin Henkes received a B.S. in Chemistry and B.A. in Spanish from Southern Methodist University in Dallas, Texas in 2004. She entered the Department of Chemistry at Texas A&M University in the fall of 2004, where she began graduate research under the direction of Prof. Raymond E. Schaak. She received a National Science Foundation Graduate Research Fellowship in 2006, and has been a member of Phi Lambda Upsilon since 2002. Her research interests include multi-element nanocrystal synthesis, low-temperature solution routes to synthesizing solid state materials, and the shape-controlled synthesis of metal and metal phosphide nanocrystals.

Ms. Henkes can be reached at the Department of Chemistry, Texas A&M University, P.O. Box 30012 College Station, TX 77842-3012. Her email addresses are ahenkes@mail.chem.tamu.edu and amandahenkes@yahoo.com.